Université de Toulouse

THÈSE

En vue de l'obtention du

DOCTORAT DE L'UNIVERSITÉ DE TOULOUSE

Délivré par *l'Université Toulouse III - Paul Sabatier*
Discipline ou spécialité : *Astrophysique*

Présentée et soutenue par *Paolo Pilleri*
Le *18-11-2010*

Titre : *Impact de l'évolution des hydrocarbures aromatiques polycyliques sur la physique et la chimie des régions des photodissciation : une étude dans l'infrarouge et le millimétrique*

JURY
Pierre Jean (Président)
Alain Abergel (Rapporteur)
Carsten Kramer (Rapporteur)
Asunción Fuente (Examinatrice)
Giacomo Mulas (Examinateur)
Jerôme Pety (Examinateur)
Christine Joblin (Directrice)
Maryvonne Gerin (co-Directrice)

Ecole doctorale : *SDU2E*
Unité de recherche : *CESR*
Directeur(s) de Thèse : *C. Joblin (CESR) ; M. Gerin (LERMA)*

Université Toulouse III - Paul Sabatier
U.F.R Physique, Chimie, Automatique

THESE

pour obtenir le grade de

DOCTEUR DE L'UNIVERSITÉ DE TOULOUSE
DÉLIVRÉ PAR L'UNIVERSITÉ TOULOUSE III - PAUL SABATIER

Spécialité

ASTROPHYSIQUE

présentée au Centre d'Etude Spatiale des Rayonnements

par

Paolo PILLERI

Impact de l'évolution des hydrocarbures aromatiques polycycliques sur la physique et la chimie des régions de photodissociation : une étude dans l'infrarouge et le millimétrique

---

P. Jean	President
A. Abergel	Rapporteur
C. Kramer	Rapporteur
A. Fuente	Examinatrice
G. Mulas	Examinateur
J. Pety	Examinateur
C. Joblin	Directrice de thèse
M. Gerin	co-Directrice de thèse

Ringraziamenti

Je profite des premières lignes de ce manuscrit pour remercier tous ceux qui ont contribué, d'une façon ou l'autre, à la rédaction de cette thèse et à rendre aussi merveilleux ces trois ans à Toulouse.

En premier, je voudrais remercier mes deux directrices de thèse. Un grand merci à Christine Joblin, pour avoir été une directrice compétente, disponible et attentive lors de ces trois ans. Merci pour la confiance et la liberté dont j'ai pu profiter, et merci surtout pour son humanité et sa sensibilité. Merci à ma co-directrice Maryvonne Gerin, pour son aide constante, ses conseils toujours pertinents et pour sa gentillesse. Merci à toutes les deux pour le temps et la patience que vous m'avez accordés ainsi que pour la passion que vous m'avez transmise.

Je voudrais remercier les membres de mon jury de thèse. Merci à Pierre Jean pour sa disponibilité à présider ce jury. Merci à Alain Abergel et Carsten Kramer, pour avoir accepté de référer cette thèse, et pour leurs conseils et remarques pertinents, qui ont contribué à améliorer le contenu final de ce travail. Je voudrais aussi remercier Jerôme Pety et Asunciòn Fuente, pour l'intérêt qu'ils ont montré dans mes travaux, et pour leur aide précieuse dans les projets que nous avons en commun. E un profondo grazie a Giacomo Mulas, per tanti motivi: per aver creduto in me, per avermi spinto a intraprendere questa sfida, e per tutti i consigli, scientifici e non, durante questi anni.

Je voudrais remercier particulièrement Olivier Berné, pour son amitié et son aide constante tout au long de ma thèse.

Je voudrais aussi remercier tous les chercheurs avec lesquels j'ai eu le plaisir de collaborer pendant la thèse. Je tiens à mentionner Volker Ossenkopf, Javier R. Goicoechea et François Boulanger pour avoir fortement contribué à l'obtention et l'analyse des données presentées dans ce manuscrit.

Merci à tous les chercheurs du département Univers Froid: ça a été un vrai plaisir de partager ces trois ans avec vous. Merci en particulier à Emmanuel Caux pour le soutien lors de la fin de la thèse. Merci à Sandrine, Karine, Charlotte, Claude, Jean-Philippe et Isabelle pour leur bonne humeur constante et leur disponibilité à tout moment.

Merci aux directeurs du CESR, Jean-André Sauvaud, et de l'IRAP, Martin Giard, ainsi qu'à tout le personnel des deux laboratoires. Je tiens à remercier en particulier Emilie Besançon, Stephanie Bruel et Jean-François Botte pour leur aide et disponibilité. Merci aussi à tous les doctorants du CESR.

Et pour finir le tour du CESR, merci au Bureau 307 et ses citoyens: Julien, son velo et sa génialité. Baptiste, sa raquette de tennis et ses leçons de Français. Francesca, ses lasagnes et sa pêche. Giuliano, sa bonne humeur et ses conseils. Et bien sûr, tous les infiltrés: Anne et sa tendresse, Jonathan et sa poesie, Valerio et sa Juve, Yann et ses crêpes, Ana et sa salsa, Natacha et ses coups de pied, et enfin Matteo, qui continue la tradition sarde au CESR/IRAP. Merci à Anthony et David pour toutes les discussions à la cantine. Enfin, merci à Ludo et Mauro, tout simplement pour tout.

Une grand merci au 'rassemblement omnisports d'un club des copains optimistes' pour les nombreuses heures passées a taper sur un ballon de futsal et les encore plus nombreux apéros après (et parfois avant) les matchs.

Merci à Manu. Lors de notre première rencontre, on était amis après deux minutes. Si ce n'est pas un record, on en n'est pas loin.

Merci à tous mes amis, en France, en Italie ou ailleurs. C'est aussi grâce à vous que j'ai réussi à arriver au bout de cette aventure. Grazie en particulier à Giacomo, Letizia, Riccardo, perché é bello tornare a casa e ritrovarvi. Grazie infinite a Andrea e Katia, "el campeon" Felice, Jenny, Nico (7), Ele e Lele, per essere dei veri amici.

Merci à *mi hermanito* Loic, Karine, Alain et Simone. Je ne vais jamais oublier Nistos Cap Nestes, la beauté des Pyrénées et de ses gens, et la véritable manière de manger la purée de patates.

Merci à Agnes, pour ses couleurs et son sourire.

Enfin, grazie alla mia famiglia. Ai miei fratelli Nicola e Lucia con le loro dolci metà; a mamma e babbo, senza bisogno di perché.

Contents

Introduction [*en*]

Polycyclic Aromatic Hydrocarbon (PAH) molecules have been proposed in the eighties as an abundant and widespread constituent of the interstellar medium. Since then, PAHs have been identified as key species in the chemistry and physics of photodissociation regions (PDRs) associated to interstellar and circumstellar environments. In particular, due to their size and chemical properties, PAHs trace the transition between small, gas-phase hydrocarbons and very small carbonaceous dust particles. Furthermore, they have a major impact in the thermal balance of UV-irradiated regions, significantly contributing to the heating of the gas by photo-electric effect.

Astronomical observations of PAHs have been historically performed in the infrared (IR) domain: the IRAS and ISO space missions have unveiled information on the nature and properties of interstellar PAHs. These studies are also possible from the ground but they are restricted to a few atmospheric windows. Recently, the AKARI and *Spitzer* space telescopes provided near- and mid-infrared observations with an unprecedented sensitivity. This enabled to extend the study of PAHs to fainter and more distant objects. Now, the *Herschel* space mission has opened a new wavelength domain in the study of PAHs and their related species by providing sensitive observations at high spectral resolution in the far-IR and sub-millimeter domains.

Whereas PAHs and related very small dust particles are better observed in the IR, many small gas-phase species are usually observed at (sub-)millimeter wavelengths. The original approach presented in this thesis is to take benefit of both types of observations to study the evolution of the PAH population and its influence on the physics and chemistry of interstellar and circumstellar environments.

This thesis is divided into four parts, organised as follows. The first part introduces the astrophysical scenario (Chaps. 1 and 2) and describes in more details the open questions that will be addressed in this work (Chap. 3). The second part contains a brief description of the astronomical instruments that have been used (Chap. 4), and describes the mid-IR analysis procedure that we have developed to characterise the evolution of the PAH population (Chap. 5). The third part analyses the evolution of PAHs and their influence on the chemistry of the ISM. In particular, Chap. 6 describes the destruction of very small dust particles by the local ultraviolet radiation field as a source of free PAHs. Chapter 7 presents the search for a peculiar PAH, corannulene, at mm wavelengths and discuss the results in terms of the destruction and formation processes of the smallest PAH species in the envelopes of evolved carbon stars. Chapter 8 presents the combination of IR and millimeter observations to study the evolutionary link between very small grains, PAHs and small hydrocarbons. The fourth part shows how the combination of

the analysis of PAH emission with that of small gas-phase species in the millimeter domain can unveil the structure (Chap. 9), energetics and dynamics (Chap. 10) of PDRs, with a special emphasis on the reflection nebula NGC 7023 NW. Finally, I summarise the results and present the main perspectives of this work.

Introduction [*fr*]

Il a été proposé au cours des années 1980 que les molécules Polycycliques Aromatiques Hydrogénées (PAH) sont une composante importante de la matière interstellaire. Depuis lors, il a été établi que les PAH jouent un rôle majeur dans la physique et la chimie des régions de photodissociation (PDR) associées aux environnements interstellaires et circumstellaires. En particulier, de par leur taille et leurs propriétés chimiques, les PAH se placent à la transition entre les petits hydrocarbures en phase gazeuse et les très petits grains carbonés. De plus, ils prennent largement part au chauffage du gaz via l'effet photoélectrique, contribuant ainsi significativement à l'équilibre thermique des régions exposées au rayonnement ultraviolet.

L'observation astronomique des PAH a été essentiellement menée dans le domaine infrarouge (IR) : les missions spatiales IRAS et ISO ont révélé des informations sur la nature et les propriétés de ces PAH interstellaires. Depuis le sol, ces études se restreignent à quelques fenêtres atmosphériques. Récemment, les satellites AKARI et *Spitzer* ont réalisé des observations dans les domaines de l'IR proche et moyen avec des sensibilités inédites, permettant l'étude d'objets moins lumineux et plus lointains. Grâce à la mission spatiale *Herschel*, l'étude des PAH et des espèces qui leur sont liées est désormais possible dans les domaines de l'IR lointain et du sub-millimétrique en bénéficiant à la fois de sensibilité et de très haute résolution spatiale.

Alors que les PAH et les très petits grains de poussière qui leur sont liés sont plus facilement observés dans le domaine IR, de nombreuses espèces du gaz peuvent être observées dans le domaine (sub-)millimétrique. L'originalité de la démarche présentée dans ce travail de thèse provient de l'utilisation conjointe de ces deux domaines d'observation pour étudier l'évolution de la population de PAH et son influence sur la physique et la chimie des milieux interstellaires et circumstellaires.

Les quatre parties de cette thèse s'articulent comme suit. La première partie introduit le scénario astrophysique (Chaps. 1 et 2) et détaille les questions encore ouvertes auxquelles ce travail apporte des éléments de réponse. La seconde partie présente brièvement les instruments d'observation astronomique qui ont été utilisés (Chap. 4) et décrit la procédure d'analyse des données du domaine IR moyen que nous avons développée pour l'étude de l'évolution de la population de PAH. La troisième partie analyse l'évolution des PAH et leur influence sur la chimie du milieu interstellaire. En particulier, le Chap. 6 décrit la destruction des très petits grains de poussière par le champ de rayonnement ultraviolet local, considérée comme source de PAH libres. Le Chap. 7 présente la recherche dans le domaine millimétrique d'un PAH particulier, le corannulène, et discute le résultat en termes de processus de formation et de destruction des

plus petits PAH dans les enveloppes des étoiles carbonées évoluées. Le Chap. 8 présente la combinaison des observations IR et millimétriques pour étudier les liens entre très petits grains, PAH et petits hydrocarbures au sein d'un scénario d'évolution. La quatrième partie montre comment la combinaison de l'analyse de l'émission des PAH et de celle des espèces du gaz dans le domaine (sub-)millimétrique peut dévoiler la structure (Chap. 9), le bilan énergétique, et la dynamique (Chap. 10) des PDR. Ces chapitres s'intéressent plus particulièrment à l'étude de la nébuleuse par réflexion NGC 7023 NW. Pour finir, je résume les résultats obtenus et présente les perspectives principales de ce travail.

Part I

The astrophysical context

Chapter

1

The interstellar medium

1.1 The phases of the interstellar medium

When observed at large scales, the interstellar medium (ISM) of our Galaxy appears very rarefied, with typical densities of 1 atom/cm^3. However, variations in density of several orders of magnitudes can be found, especially in the Galactic disk where most of the mass of the ISM lies. When dealing with the different environments of the ISM, it is evident that a precise taxonomy based on any single physical parameter is impossible, since gradients can be very smooth, and that some environments may fall in more than a single class. However, a general classification can be made, on the basis of density, temperature and ionisation state of the different phases of the ISM (McKee and Ostriker, 1977). Table 1.1 summarises a recent update of such classification, reporting typical values for hydrogen density (n_H) and gas temperature (T) for each medium. Hereafter, n_H represents the local density of hydrogen in all its forms.

Hot ionized medium

The Hot Ionised Medium (HIM), or coronal gas, accounts for a large fraction of the volume of our Galaxy but only for a small part of its mass. Most of the coronal gas is located in the halo of the Galaxy, where the local density is so low that UV radiation

Table 1.1: Typical physical conditions for the different phases of the ISM in the Milky Way. *Adapted from Tielens (2005).*

Phase	n_H [cm^{-3}]	T [K]	Principal tracer
Hot Ionised Medium	$10^{-4} - 10^{-2}$	$\sim 10^6$	X-rays, UV
Warm Ionised Medium	$10^{-1} - 10^3$	~ 8000	H_α
Warm Neutral Medium	~ 0.5	~ 8000	H I emission
Cold Neutral Medium	~ 50	~ 80	H I absorption & C^+ emission
Molecular medium	> 200	~ 10	Optical, IR, radio

and shocks from supernovae can easily propagate through, heating the gas to the highest temperature found in the ISM ($T \sim 10^6$ K) and ionising most of it.

Warm ionized medium

Photons carrying energy greater than 13.6 eV ($\lambda < 912$ Å) ionise neutral hydrogen (H I). Eventually, with time scales that depend on the physical conditions of the region (the electron density n_e and T), the ionised hydrogen (H II) recombines with free electrons. In the Warm Ionised Medium (WIM), recombination is a slower process than ionisation, and most of the gas is found in a ionised state. Photoionisation is also responsible for the gas heating, since a fraction of the energy of the ionising photons is transferred to the ejected electrons that heat the gas through collisions. The outcome is a typical gas temperature of about 8000 K. These regions are traced by optical recombination transitions (principally the Balmer series of hydrogen), although they present also *free-bound* continuum associated to electron recombination and *free-free* radio continuum, due mainly to the acceleration of electrons that interacts with protons without recombination.

Neutral atomic medium

In our Galaxy, hydrogen is found mainly in its neutral form. In fact, H I is the major constituent of the mass of the interstellar medium. It can be found in a warm phase (WNM, Warm Neutral Medium) at temperatures similar to those of the WIM, or at much colder temperatures (~80 K) in the so-called Cold Neutral Medium (CNM). The heating of these regions is mainly due to photo-electrons ejected from dust particles. The principal tracer of these atomic regions is the 21 cm hyperfine transition of H I, which is observed in emission at warm temperatures, whereas colder regions are mainly studied with absorption measurements.

Cold molecular medium

The Cold Molecular Medium (CMM) accounts for a large fraction (~ 30 %) of the mass of the ISM, but a very small part of its volume. Most of the mass of the CMM is found

in gravitationally-bound molecular clouds in the Galactic plane, with local densities that range from few 10^2 cm^{-3} to over 10^7 cm^{-3}. Typical gas temperatures for this phase range from few K to some tens of K. The densest molecular clouds are not in pressure equilibrium with the neutral gas surrounding them but are rather collapsing cores that will eventually give birth to stars.

1.2 The lifecycle of matter in the Galaxy

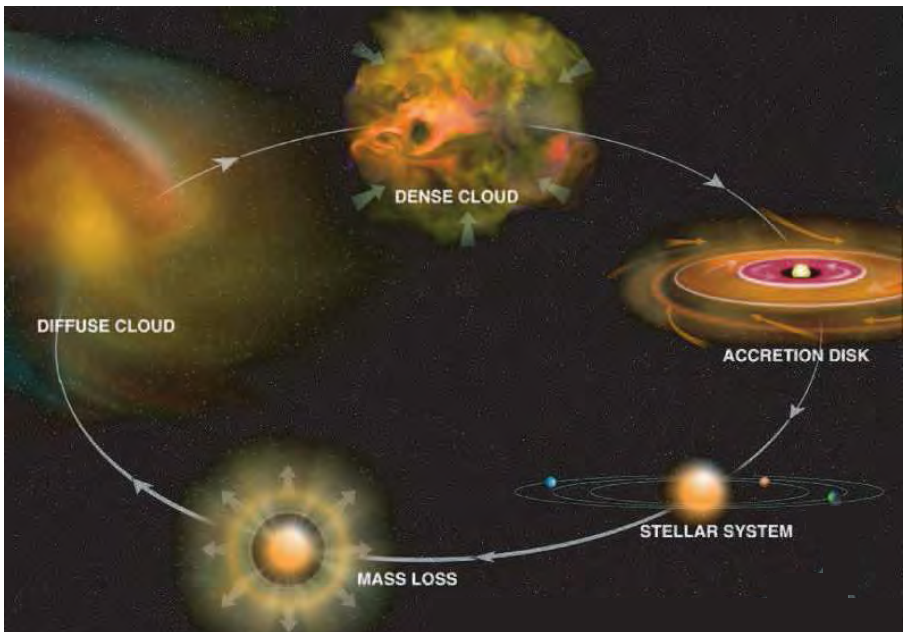

Figure 1.1: Scheme of the lifecycle of matter in our Galaxy. *Source: Bill Saxton - NRAO/AUI/NSF*

Stars are formed when a dense part of a molecular cloud collapses due to self-gravity. Such clumps are the densest and coldest environments of the interstellar medium: UV radiation cannot penetrate the central cores of these regions, where molecules can form (in grain mantles or by gas-phase chemistry) without being submitted to destruction by the UV field. When a clump reaches the Jeans mass it forms a **protostar**. At this stage, the contraction of the protostar produces heat that may evaporate the grain mantles, injecting molecules into the surrounding gas, but the core is not yet hot enough to ignite the fusion of hydrogen and start its career as a star. During the collapse, the conservation of angular momentum may lead to the formation of a rotating circumstellar disk, or **proto-planetary disk**.

The initial mass of the collapsing core determines the following stages of stellar evolution and its ultimate fate. Massive stars ($M > 8M_\odot$) evolve so quickly that the steps of their formation and evolution up to the main sequence phase are still unclear.

These stars will burst in supernovae at their later stage of evolution. The evolution of lower mass **T-Tauri** stars ($M < 2M_\odot$), and intermediate mass **Herbig Ae-Be** stars ($2 < M/M_\odot < 8$) is somewhat better understood: they will evolve in main sequence stars when the core contraction yields temperature sufficient to ignite the fusion of hydrogen.

During their main sequence, the intermediate mass stars may form a so called **H II regions**. The bulk of the radiation of young O/B stars is emitted in the UV portion of the spectrum, and the photons with energy higher than 13.6 eV ionise the hydrogen gas that surrounds the star.

At the end of their main sequence, when the hydrogen reservoir has been exhausted, these low- to intermediate-mass stars enter in the Asymptotic Giant Branch (AGB) phase, in which the central core contracts until it reaches the temperature needed to start the fusion of helium and, successively, carbon. While the core collapses, the outer layers of the stars are blown away and cool down, giving birth to a **circumstellar envelope** (CSE). In this phase, the photons from the central star may ionise and process the material in the envelope. **Planetary nebulae** (PNe) are the final step in the evolution of low- to intermediate-mass stars. This stage is reached when the reservoir of helium has been exhausted and the central star becomes a white dwarf. These stars have completely ejected their outer envelopes, which are ionised by the central source.

The remnants of the circumstellar envelopes that are ejected from the evolved stars in the ISM merge continuously with the surrounding materials and form **diffuse clouds**. Being the product of dust and gas processing in evolved stars, the newly formed nebulae are generally enriched in heavy elements and processed dust. Diffuse regions can be observed (either in emission or in absorption) because the material that constitute them is illuminated by other near-by stars. Eventually, these diffuse regions may evolve in gravitationally bound dark clouds, starting the cycle of matter from where it began.

1.3 PHOTO-DISSOCIATION REGIONS

In the ISM, as well as in many circumstellar environments, the far-UV photons ($6 < h\nu < 13.6$ eV) drive the thermal balance, the physical processes and the chemical evolution. Such UV photons are energetic enough to break typical molecular bonds, and therefore UV-illuminated environments are generally called Photo-Dissociation Regions (PDRs). Regions such as the inner edges of the envelopes in PNe, the illuminated edges of the dark nebulae and reflection nebulae can be considered as PDRs.

Figure 1.2 shows the schematic view of a typical edge-on PDR which is formed by the UV radiation from a nearby star impinging over the border of a molecular cloud. The depth along a PDR is often measured in magnitudes of visual extinction (A_V) at 5500 Å caused by dust particles immersed in the gas. Typically, one magnitude of A_V corresponds to a total hydrogen column density from the PDR surface of 1.8×10^{21} H cm^{-2}, although depending on the environment. The different layers of a typical PDR can be schematised as follows:

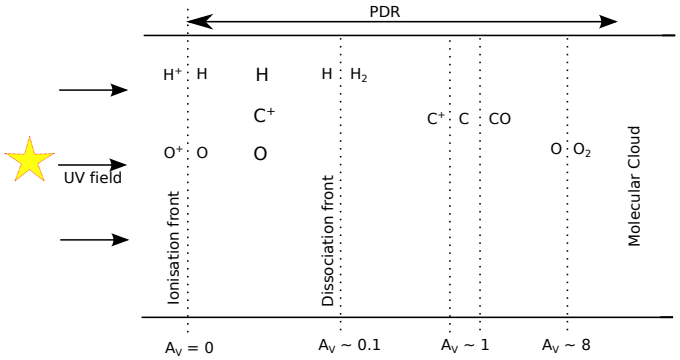

Figure 1.2: Schematic representation of an edge-on PDR, illuminated on the left by the UV field from nearby hot star. The A_V values reported for the chemical transitions refer to a mild UV-irradiated PDR, and depend on the irradiation conditions. *Figure adapted from Draine and Bertoldi (2000).*

- A region where atomic hydrogen is mostly neutral, and the far-UV photons yield the ionisation of atomic carbon. This region is usually characterised by the emission of [C II] and [O I] fine structure lines and by the IR emission from very small dust particles, in particular PAHs (Polycyclic Aromatic Hydrocarbons, see Chap. 2).

- At $A_V \sim 0.1 - 0.2$ the formation of H_2 on grains starts to be an efficient process compared to the photo-destruction of gas-phase H_2. This produces a transition between atomic and molecular hydrogen. This region is characterised by the emission in the IR ro-vibrational emission of H_2: the gas kinetic temperature can reach hundreds of K due to photoelectric heating, enough to excite H_2 to produce rotational IR emission. At these depths, carbon is still observed mainly in its ionised atomic form, and the IR emission of very small dust particles and the [C II] and [O I] lines is still observed.

- A transition between ionised and neutral carbon is observed at $A_V \sim 1 - 2$. Most of the atomic oxygen combines with carbon to form CO. H_2 is still by far the most abundant molecule, but being hard to observe at these depths due to the low gas temperature, the main tracer of molecular gas at these depths is CO.

- Molecular oxygen is efficiently formed deeper in the PDR, at $A_V \sim 8$.

In stationary regime, the transition between each layer can be very smooth or extremely harsh, depending on the physical conditions of the PDR, in particular on the illuminating radiation field and the local density. Typical densities of PDRs can vary from $\sim 10^2\,\mathrm{cm}^{-3}$ to some $10^6\,\mathrm{cm}^{-3}$, whereas values for the illuminating radiation field are usually in the range of $1 < G_0 < 10^6$ in units of the Habing (1968) field. G_0 is defined as the average interstellar flux in the solar proximity between 6 and 13.6 eV, and corresponds to $1.6 \times 10^{-3}\,\mathrm{erg\,cm}^{-2}\,\mathrm{s}^{-1}$.

In the scheme of Fig. 1.2 are reported only the most abundant gas species and their transitions along the PDR front. Of course, the UV field does not control the evolution of these species only, but drives all the chemical networks in the PDR. It is also strongly absorbed by the various dust populations leading to emission in the IR. Some of these processes and the associated open issues will be developed in Chap. 3.

Chapter

2

Gas, dust, and in between: Polycyclic Aromatic Hydrocarbons

Amongst the elements, hydrogen constitutes about 70.4% of the mass of the ISM, followed by helium (~ 28.1%) and heavier elements (in particular C, O, N, S, Fe, Si, Mg, Al, ...) which account for only about 1.5% of the mass. About 99% of the mass of the ISM is locked in gas phase species. The rest is found in dust particles.

2.1 Gas

Atomic gas. Atomic lines are observed in many interstellar and circumstellar environments. The 21 cm line of atomic hydrogen is the main observational tool to study the physical conditions in neutral atomic regions. Many atomic absorption lines are also detected in the visible and UV part of the spectrum. In warm regions, atoms are mainly detected by their forbidden fine structure transitions: the [C I], [C II], [O I], emission lines in the far-IR are usually very intense in PDRs. Other fine structure lines may arise from more ionised regions, either highly irradiated PDRs or H II regions, such as the [Ar II], [Ar III], [Ne II], [S IV], [O IV] that are observed in the mid-IR (see, for instance, Fig. 2.5).

Molecular gas. Molecular bonds can easily be broken by harsh UV photons. Therefore molecules are found mainly in the outer layers of CSEs, the internal layers of PDRs and disks, where the radiation is attenuated by dust and the molecules can survive to photo-dissociation. Yet molecules are also present in the diffuse ISM.

The two most abundant molecules detected in the ISM are H_2 and CO. Today, more than 150 molecules (plus their isotopomers) have been identified in the ISM and CSEs, from the simplest H_2 to long chains as $HC_{11}N$. The molecular richness of the ISM environments depends on their conditions, some molecules being very specific to particular ISM conditions. A list of the molecular species detected in space to date can be found in the Appendices. There is also strong evidence for other large molecules such as Polycyclic Aromatic Hydrocarbons (PAHs), although no single molecule has been unambiguously identified in the ISM yet (cf. Sect. 2.3). Still, very recently, the presence of C_{60} and possibly C_{70} has been evidenced both in PDRs (Sellgren *et al.*, 2007, 2010) and in one planetary nebula (Cami *et al.*, 2010).

In molecular clouds the gas temperature can be very low (down to a few K), and molecules are detected in the radio through their low-lying rotational transitions. In some cases (mainly UV-pumped or collisional excitation in hot and dense environments and shocks, and PDRs) the higher rotational or vibrational modes of the molecule can be populated, and the corresponding ro-vibrational transitions are emitted in the (far-)IR and sub-millimeter domain. H_2 constitutes a very particular case, since it is a homonuclear molecule and does not have a permanent dipole moment. Therefore, the low-lying energy levels are linked through quadrupole transitions with small transition probabilities and relatively high excitation energies. H_2 emission can therefore arise only if the molecule is either UV-pumped or collisionally excited in hot environments like PDR edges.

The pathways for the production of molecules are gas-phase reactions in complex chemical networks and reactions on grain surfaces. However, the precise formation networks for many interstellar molecules, from the simplest H_2 to large PAHs, are not yet completely understood.

2.2 Dust

Dust particles are spread through the whole ISM. Even though their abundance is scarce ($\sim$ 1% of the total mass of the ISM) they play a fundamental role in many processes of the ISM. First, dust is responsible for the **extinction** and polarisation of the stellar radiation. Most of the energy carried by the absorbed photons is re-emitted at longer wavelengths by **thermal emission**. Also, small dust particles significantly contribute to the thermal balance of the gas through photo-electric heating. Dust grains are important in the formation of molecules, not only because they shield them from the UV radiation field, but they can also act as catalysers for reactions on their surfaces. Finally, dust has a major contribution in the depletion of heavy elements (Field, 1974).

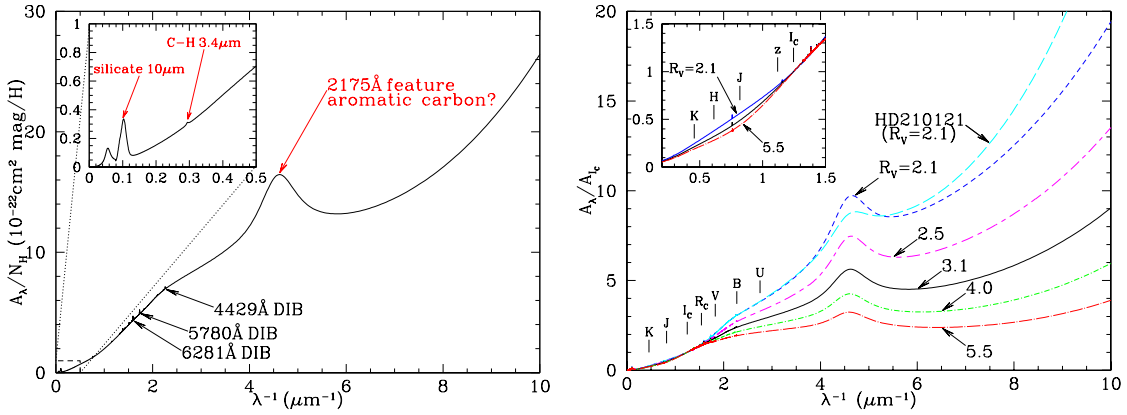

Figure 2.1: *Left:* Average dust extinction in the diffuse interstellar medium. Some of the strongest DIBs are superimposed and labelled. *Source: (Draine, 2009).* *Right:* Calculated extinction curves for R_V values ranging from 2.1 to 5.5. *Source: (Draine, 2003)*

2.2.1 Extinction

Dust absorbs and scatters visible and UV radiation very efficiently and the combination of these two effects is called extinction. The first panel in Fig. 2.1 shows the wavelength dependence of the average extinction curve in the Galaxy (Draine, 2009). The most evident feature is the UV bump at 2175 Å, superimposed to a quite smooth rise from the IR to the UV. The overall shape of the extinction curve, including the slope of the UV-rise varies in different lines of sight (Fitzpatrick and Massa, 1986, 1988) but the whole family of extinction curves can be represented with a single parameter, R_V (see Fig. 2.1, right). This is defined as $R_V = A_V/E(B-V)$, where A_V is the measured extinction in the visible, and $E(B-V)$ is the color excess in the line of sight. Values of R_V have been found to vary between 2.1 in the diffuse medium to 5.5 in denser molecular clouds and icy environments, with an average value in the Galaxy of $R_V = 3.1$ (Cardelli *et al.*, 1989).

The wavelength dependence and spatial variation of the extinction curve are often used as tracers of dust properties along the line of sight. The UV extinction bump was first detected by Stecher (1969). Bless and Savage (1972) attributed it to a multicomponent interstellar dust. Now the majority of the authors agree that this strong feature is due to $\pi \rightarrow \pi^*$ excitation in aromatic carbons, including PAHs. In the IR, the extinction curve has a quite smooth rise, with some superimposed features. The 9.7 and 18 μm absorption features are attributed to the Si-O stretching and bending modes in amorphous silicates (Kemper *et al.*, 2005), whereas the 3.4 μm absorption feature is associated to C-H stretching mode of grains containing aliphatic hydrocarbons. The nature of the latter is still controversial (Pendleton and Allamandola, 2002; Dartois *et al.*, 2004). Superimposed to the smooth profile of the extinction curve there are more than 200 weak unidentified absorption features observed from 4000 to 13200 Å, the so-called **Diffuse Interstellar Bands** (DIBs, for a review see Herbig, 1995). Since their first detection by

Merrill (1934), not a single carrier of the DIBs has been firmly identified.

2.2.2 Thermal emission

Dust re-emits the energy it has absorbed from the UV photons as thermal emission in the IR-mm domain. The characteristics of the thermal emission depends on the nature and the size of the grains. Current models are able to fit reasonably well the spectral energy distribution (SED) of many lines of sights (see, for instance, Draine and Li, 2007; Compiègne *et al.*, 2010). Generally speaking, large grains have a high heating capacity and the absorption of a single UV photon does not significantly change their temperature (cf. Fig. 2.3). Therefore, they radiate in the IR-mm as grey-bodies at an equilibrium temperature, which is a few tens of K for a typical molecular cloud. This thermal emission accounts for most of the emission at $\lambda > 60\,\mu$m. Smaller dust particles (such as PAHs) also emit infrared photons after absorption of a single UV photon, but being much smaller, they can be heated to very high temperatures upon absorption of a single UV photon. The PAH molecule then cools down by slow IR emission into its IR-active modes. In general, the molecule has the time to re-emit this excess energy through various de-excitation pathways before absorbing another photon, except in regions with quite high photon flux ($G_0 \gtrsim 10^5$). Figure 2.2 shows a modelled SED including different different grain populations (see below). The emission process for PAHs will be further described in Sect. 2.3.

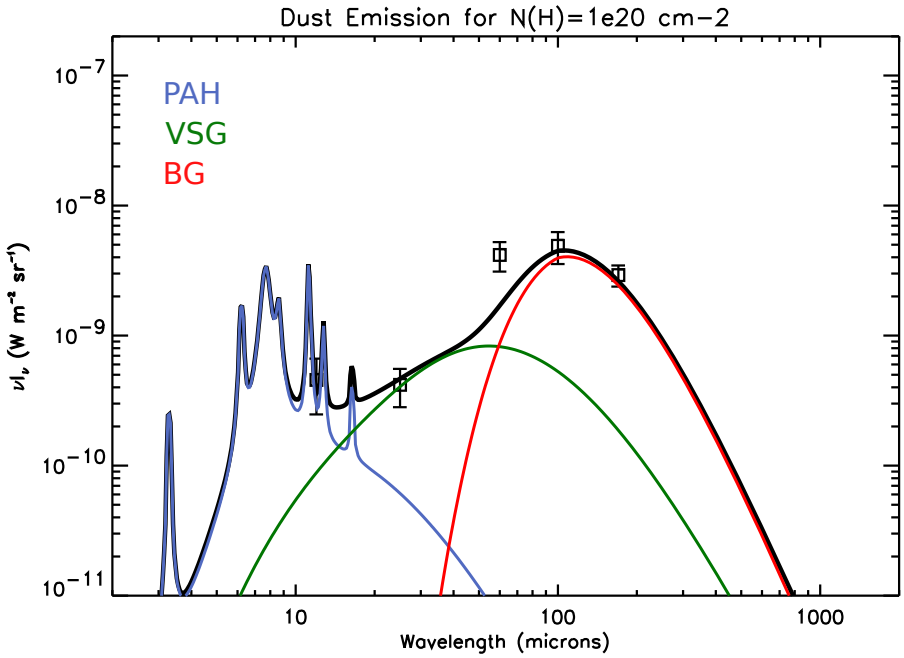

Figure 2.2: The mean emission spectrum of the Small Magellanic Cloud fitted with the model of Désert *et al.* (1990). *Figure adapted from Bot* et al. *(2004)*

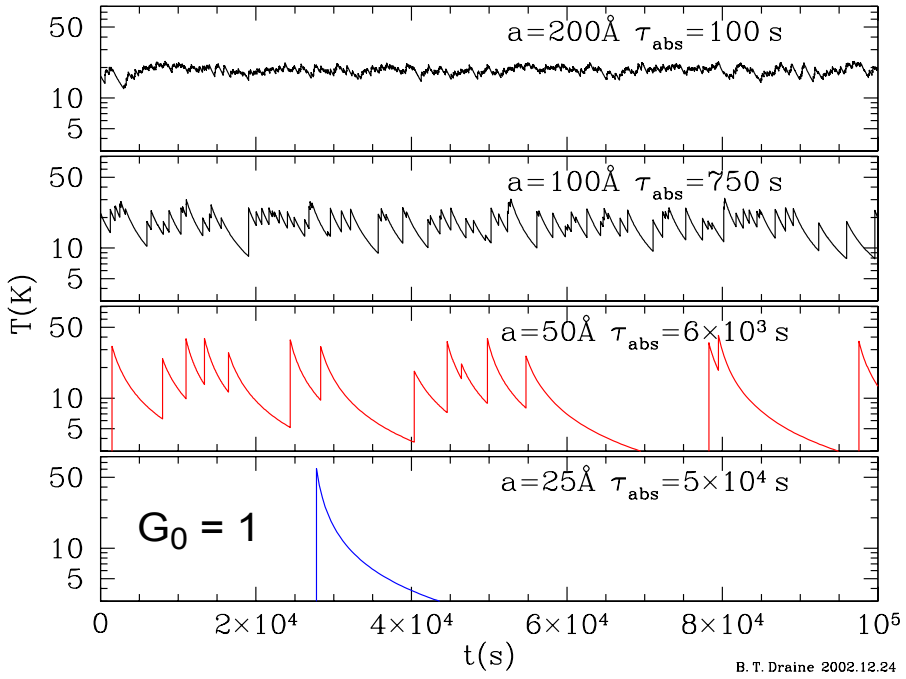

Figure 2.3: The temperature fluctuations of interstellar grains of different sizes heated by the average interstellar radiation field of our galaxy ($G_0 = 1$). Big grains, with a high heating capacity, maintain an equilibrium low temperature upon absorption of a UV photon, while the smallest grains (such as PAHs) heat up to a high temperature and cool down before absorbing another photon. τ_{abs} is the absorption rate of a UV photon for that particular size and in the mean interstellar radiation field. *Source: Draine (2003)* .

2.2.3 Extended Red Emission

The Extended Red Emission (ERE) is a broad band ($\sim$ 350 nm) emission in the visible-UV part of the spectrum of several reflection nebulae and other interstellar objects. It was first observed by Cohen *et al.* (1975) in the Red Rectangle nebula, and the first attribution of ERE to luminescence of PAH-like molecules was proposed by D'Hendecourt *et al.* (1986). Recently, Witt *et al.* (2006) proposed PAH di-cations (PAH^{++}) as possible ERE carriers. This assignment was then revisited by Berné *et al.* (2008), who instead proposed ionised PAH dimers ($[PAH_2]^+$) as possible carriers of ERE. Other candidates for ERE were proposed as well (for a review, see Witt *et al.*, 2006) but none provides a satisfactory explanation.

2.2.4 Grain size distributions

The wavelength dependence of the extinction curve provides a first important constraint on the grain size distribution. The first model of the grain size distribution was proposed by Mathis *et al.* (1977), in which the dust population was composed of spherical grains of both graphite and silicates. This model (hereafter, the MRN model) was able to fit

reasonably well the extinction curve in several lines of sight from the IR to the UV by assuming a size distribution $n(a) = K \times a^{-3.5}$, where a is the radius of a spherical grain (comprised between 250 and 2500 Å) and K is a constant. Successively, the range of the size distribution of the MRN model was extended (from 30 to 10000 Å) by Draine and Lee (1984), where specific optical properties for the graphitic and silicate dust particles were included, in contrast with the simple spherical grains of MRN. However, the smallest sizes are difficult to infer from the fit of the extinction curve, and such estimate is better constrained using the emission features in the near- and mid-IR. PAHs were first introduced in grain models by Désert *et al.* (1990). Very Small Grains (VSGs) are a second class of mid-IR emitters that can contribute to the mid-IR emission if they are small enough to be stochastically heated (Désert *et al.*, 1990). The VSGs are generally considered to be carbonaceous (Désert *et al.*, 1986) but Li and Draine (2001b) concluded that the presence of very small silicate grains is not excluded and can involve up to 10% of interstellar Si.

2.3 Interstellar PAHs

Polycyclic Aromatic Hydrocarbons (PAHs) are a class of large molecules composed of a skeleton of two or more aromatic carbon rings and hydrogen atoms at the periphery. They have properties typical of both gas-phase and solid grains. They can be also considered as an intermediary stage between the small hydrocarbons and very small carbonaceous grains. According to Joblin *et al.* (1992), PAHs contain up to 20% of the total interstellar carbon, making them the more abundant interstellar molecules after CO and H_2. Assuming 3×10^{-4} for the abundance of carbon yields to the abundance of carbon locked in PAHs of 6×10^{-5} for the diffuse medium ($R_V = 3.1$, Joblin *et al.*, 1992). This abundance value is consistent with that determined by (Draine, 2003). The author also showed that this varies in different environments reaching 4.2×10^{-5} for $R_V = 5.5$. Figure 2.4 shows a number of examples of the PAH family.

2.3.1 The Aromatic Infrared Bands

The Aromatic Infrared Bands (AIBs) are a set of emission bands observed in the infrared spectrum of a large number of interstellar objects. The most intense bands are located at $\sim 3.3, 6.2, 7.7, 8.6, 11.3$ and $12.7\,\mu$m. They are associated to C-C and C-H stretching and bending transitions of PAHs (Léger and Puget, 1984; Allamandola *et al.*, 1985) that are emitted during the IR cooling cascade that follows the absorption of a UV photon. Figure 2.5 shows these bands measured by the SWS spectrometer of ISO in the Orion Bar and NGC 7027, and summarises the association of each of the observed features with the corresponding PAH vibrational mode.

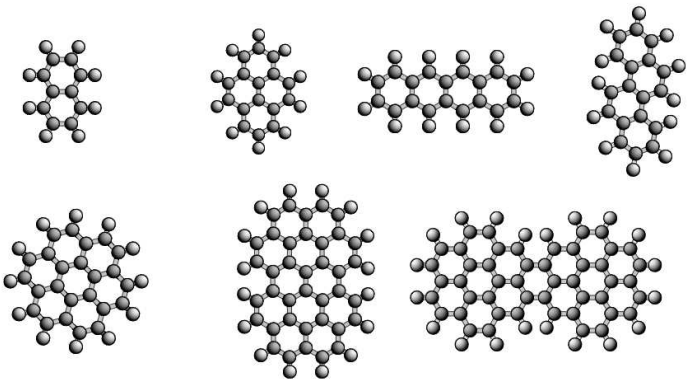

Figure 2.4: Few examples of the PAH family. Upper row: naphtalene ($C_{10}H_8$), pyrene ($C_{16}H_{10}$), tetracene ($C_{18}H_{12}$), chrysene ($C_{18}H_{12}$). Lower row: coronene ($C_{24}H_{12}$), circumbiphenyl ($C_{38}H_{16}$), dicoronylene ($C_{48}H_{20}$). *Figure adapted from Malloci* et al. *(2004).*

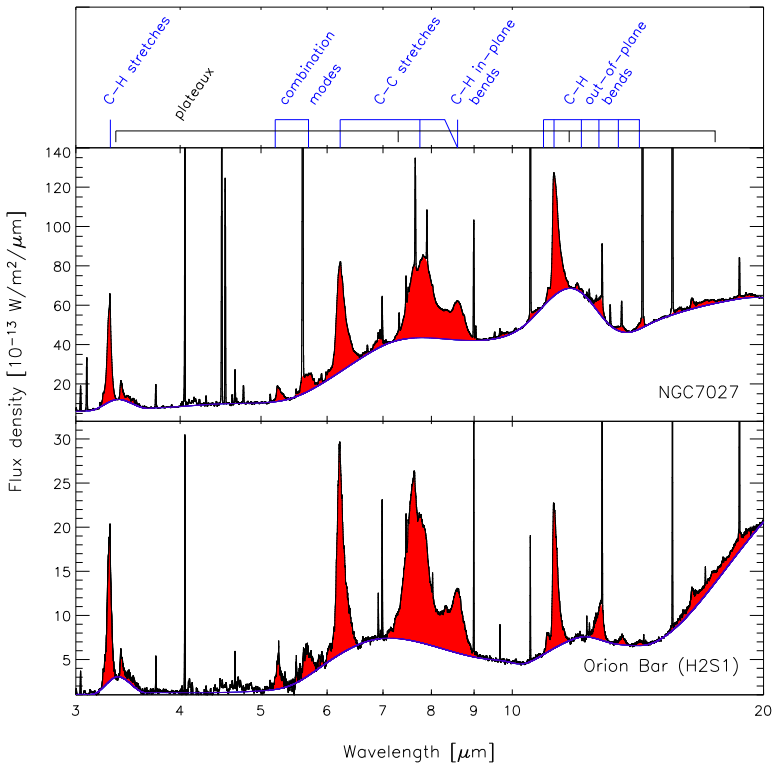

Figure 2.5: Observed mid-IR spectrum of the Orion Bar and NGC 7027, and the association of the AIB features with the corresponding vibrational transition of PAHs. The sharp lines are due to the ionised gas. *Source: Peeters* et al. *(2004)*

Spectral variations of the AIBs

The relative intensities, positions and shapes of the mid-IR bands can show large variations in different environments of the ISM and CSM. In particular, the ISO and *Spitzer* telescopes have unshed a wealth of details on such variations in different sources, or even within the same source (see, for example, Peeters *et al.*, 2002; Werner *et al.*, 2004b). These variations reflect differences in the chemical composition of the AIB carriers and in the physical conditions to which they are exposed. Several authors have studied the evolution of the AIB properties in different environments to solve the evolutionary scheme of the carriers (see, for instance, Hony *et al.*, 2001; Peeters *et al.*, 2002; Rapacioli *et al.*, 2005; Berné *et al.*, 2007; Joblin *et al.*, 2008).

The absolute intensities of the AIBs in different PDRs have been found to approximately scale with the impinging UV radiation field (Boulanger *et al.*, 1998). Such correlation appears natural, since PAHs are very efficient at converting the UV photons from stars into IR photons. The ionisation state of PAHs is also reflected in the relative intensities of the bands. For instance, the ratio of the intensities of the 7.7 and 11.3 μm bands ($I_{7.7}/I_{11.3}$) is higher for ionised species, as showed by both quantum-chemical calculations (DeFrees *et al.*, 1993) and laboratory measurements (Szczepanski and Vala, 1993b,a).

2.3.2 Photo-physics of an interstellar PAH

In typical interstellar conditions, a PAH will spend most of the time in its fundamental ground state. The probability of the absorption of a single photon of energy E is proportional to the number of photons carrying energy E and to the absorption cross-section $\sigma(E)$ (for experimental and theoretical estimates of $\sigma(E)$, see Joblin *et al.*, 1992; Malloci *et al.*, 2004). It has been shown (Joblin *et al.*, 1992) that $\sigma(E)$ actually scales linearly with the number of carbon atoms in the PAH. When a UV or visible non-dissociating photon is absorbed, the molecule is brought into an excited electronic state.

In a molecule containing a large number of atoms, several vibrational levels associated to different electronic states lie at the same energy, in the limit of Heisenberg uncertainty. Iso-energetic non-radiative transitions between these initial excited states and the ground electronic excited state (or in some cases the first excited state, cf. Fig. 2.6) occur very fast. This process is called **internal conversion** (IC).

Even if the probability of a single non-radiative transition is very low, the density of the vibrational states corresponding to a given energy can be so high (10^{50} eV^{-1} at 10 eV for coronene, $C_{24}H_{12}$) that IC can occur at time scales of 10^{-12} – 10^{-8} s, faster than any electronic radiative transition, which has time scales of about 10^{-7} s. The same process can occur between electronic states of different multiplicity, with time scales slightly slower: this process is known as **intersystem crossing** (ISC).

The number of vibrational states that are iso-energetic at a given energy is higher in the low-lying electronic states: after IC, the molecule has a high probability to be found in a vibrationally excited level of the electronic ground state. It can eventually

be also found in the first excited states (S_1 or T_1 for neutral species). Processes like fluorescence for the S_1 state(with time scales of about 10^{-7} s), or phosphorescence for the T_1 state (with time scales of a few seconds) can happen resulting in the emission of a visible photon.

IC, phosphorescence and fluorescence will bring the molecule to the electronic ground state with a lot of vibrational energy, This vibrational energy will be redistributed amongst the modes by a process called internal vibrational redistribution (IVR). From here, the molecule de-excites by emitting IR photons, with a time scale of the order of 0.1 s, although it can take more than several seconds to relax most of the energy. Figure 2.6 gives an overview of these processes for a neutral PAH.

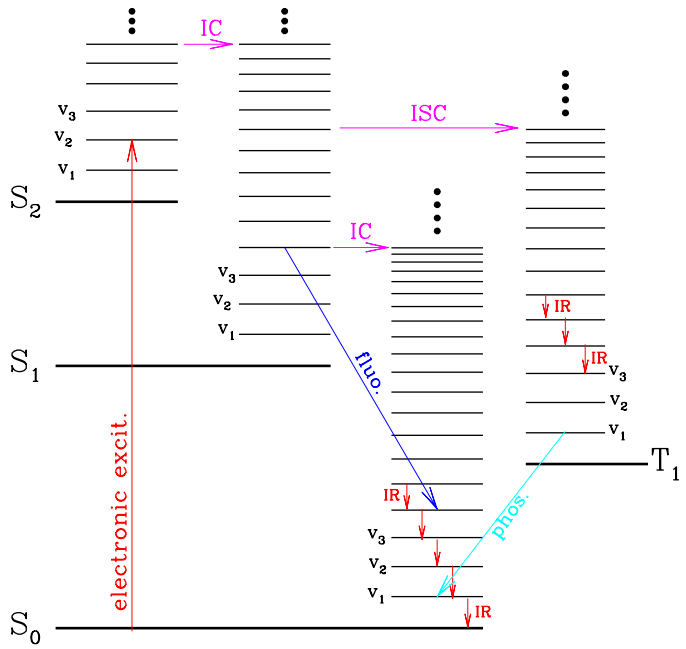

Figure 2.6: Scheme of the excitation and de-excitation mechanisms for a large isolated neutral PAH absorbing a single UV photon. *Adapted from Li (2004)*

2.3.3 Identification of PAHs

Today, the presence of PAHs in the ISM is well agreed upon. However, a firm identification of a single species that belongs to the PAH family is still missing.

The AIBs are generally attributed to the PAH class, but unfortunately, they cannot be used for the identification of any specific molecule because they are associated to transitions common to many species. In order to provide a specific identification, one needs to explore a different spectral domain, where the transitions are characteristic of specific molecules.

Visible and UV

The correspondence of DIBs with electronic transitions of PAHs constitutes a way to proceed for the identification of interstellar PAHs (see, for instance, Salama *et al.*, 1999). This task requires high quality observations and very demanding experiments for each molecule (see, for example, Useli-Bacchitta *et al.*, 2010). Recently, Iglesias-Groth *et al.* (2008, 2010) proposed the identifications of two particular small PAHs, respectively the naphthalene cation ($C_{10}H_8^+$) and the anthracene cation ($C_{14}H_{10}^+$), on the basis of the correspondence of two observed DIBs along a single line of sight, with a laboratory spectrum, but these assignements are still uncertain.

Far-IR modes

Another possibility to identify PAHs is to search for the far-IR modes of PAHs that are characteristic of the deformation of the whole carbon skeleton of the molecule. Far-IR bands tend to be emitted when the excitation energy of the molecule is relatively low, therefore lifetime broadening should not hinder the detection of the fine structure of these bands (Joblin *et al.*, 2002; Mulas *et al.*, 2006).

Unfortunately, most of the vibrational energy of a PAH is emitted in the mid-IR, and therefore the far-IR bands are expected to be very weak. Joblin *et al.* (2002) showed that only 0.2% of the total UV energy absorbed by a coronene, will be emitted in FIR band emission. Therefore, the far-IR emission of specific PAHs is expected to be challenging but could be possible with the high sensitivity of the *Herschel* Space Observatory in bright sources (Mulas *et al.*, 2006). This is a subject in which results are expected in a near future.

Radio

Most neutral, unsubstituted PAHs have a planar structure, and do not have a permanent dipole moment. Therefore, they do not present a pure rotational spectrum, or a very weak one. Some exceptions exist (Lovas *et al.*, 2005; Thorwirth *et al.*, 2007), one of them being the molecule corannulene ($C_{20}H_{10}$), which has a bowl-shaped structure due to the pentagonal ring in the center. This molecule has therefore a high permanent dipole moment (2.07 Debye) and should show a rotational spectrum. The search for this molecule in the millimeter domain will be presented in Chap. 7.

Chapter

3

PAHs in the physics and chemistry of the ISM

3.1 Carbon chemistry

Carbon is an important component of both gas-phase species and dust components in the ISM and CSM. The study of the processes that drive the carbon cycle in the ISM is a key aspect to understand the physics and chemistry in the ISM. In this section we will present our current knowledge on the formation and evolution of PAH-related molecules in the ISM.

3.1.1 Formation and evolution of PAHs

Formation in AGB envelopes

It is generally agreed that the principal sites of formation of interstellar PAHs are the envelopes of evolved carbon stars (for a review, see Kwok, 2004). The precise pathways that bring to the formation of PAHs are still uncertain, but the most likely scenario involves the pyrolysis of smaller hydrocarbons (Frenklach and Feigelson, 1989; Cherchneff *et al.*, 1992), especially acetylene (C_2H_2). Cernicharo *et al.* (2001) detected small

hydrocarbon species that are thought to be the precursors of PAHs (C_4H_2, C_6H_2 and benzene, C_6H_6) in AFGL 618, an evolved carbon star with a large circumstellar envelope. These detections gave further support to the hypothesis that PAHs (or their precursors) should be present in the envelopes of evolved carbon stars. Bright AIB emission is observed in proto-planetary Nebula (PPNe) and PNe. Even if PAHs are present in AGB stars, the direct observation of AIBs could be hindered by the fact that either these stars are too cool to trigger AIB emission, or/and that the opaque interior of the circumstellar envelope may shield the AIB carriers present in the outer layers. Recently, Boersma *et al.* (2006) detected PAH emission in one late AGB star, TU-Tau, in which the dust is heated by a hot companion that provides the UV radiation. Successively, Sloan *et al.* (2007) detected AIB emission in a carbon-rich AGB star, that presents also a circumstellar disk. The PDR in the disk is most likely the region where the AIBs originate. Smolders *et al.* (2010) reported the detection of PAH emission in earlier AGB stars, in which the circumstellar envelope is not yet opaque to radiation and the central star can induce AIB emission from the surrounding envelope. These stars, however, are too cold to produce a strong UV radiation field, so the AIB carriers must be excited through visible pumping (Li and Draine, 2002) which implies that they must be either cationic or very large aromatic compounds, or aliphatic. Cherchneff (2006) showed that the production of C_2H_2 by non-equilibrium chemistry is possible in the outer regions of such stellar outflows, coherently with the global pyrolysis picture.

Formation by fragmentation of grains

A second production pathway of interstellar PAHs, complementary to the previous, is the fragmentation of amorphous grains or Very Small Grains by shocks or UV irradiation (Scott and Duley, 1996; Cesarsky *et al.*, 2000). Very Small Grains (VSGs) are a second class of mid-IR emitters that are stochastically heated as PAHs, and can contribute to the mid-IR emission if they are small enough (Désert *et al.*, 1990). The VSGs are generally considered to be carbonaceous (Désert *et al.*, 1986) but Li and Draine (2001b) concluded that the presence of very small silicate grains is not excluded involving up to 10% of interstellar Si. Using blind source separation methods, Rapacioli *et al.* (2005) and Berné *et al.* (2007) extracted three independent spectra from the mid-IR emission (cf. 3.1: two molecular PAH-type spectra attributed respectively to neutral (PAH^0) and ionised (PAH^+) populations and one that consists in both continuum and broad band emissions. The latter was attributed to the VSG population although they cannot be strictly identified as the VSG population of Désert *et al.* (1990). Their properties are similar to the PAH grains modelled by Li and Draine (2001a) whose optical properties are constructed by mixing PAH bands with graphite continuum. Interestingly, Rapacioli *et al.* (2005) and Berné *et al.* (2007) showed that molecular PAHs are produced from the photo-processing of the so-called VSG population. We therefore refer to the latter as **evaporating VSG (eVSGs)**.

Rapacioli *et al.* (2005) proposed PAH clusters as possible candidates for eVSGs, and Rapacioli *et al.* (2006) studied the lifetime of these species in the NGC 7023 PDR.

The clusters they studied consisted of rather small stacks of neutral coronene molecules ($C_{24}H_{12}$) and the authors found that these clusters are very efficiently evaporated by UV radiation in PDRs. Larger clusters (e.g. made of larger units than $C_{24}H_{12}$ or containing more than the maximum size of 13 units, see Rapacioli *et al.*, 2006) may be more stable to UV radiation, and theoretical studies on their stability in ISM conditions is an on-going work at CESR (Montillaud *et al.*, 2011).

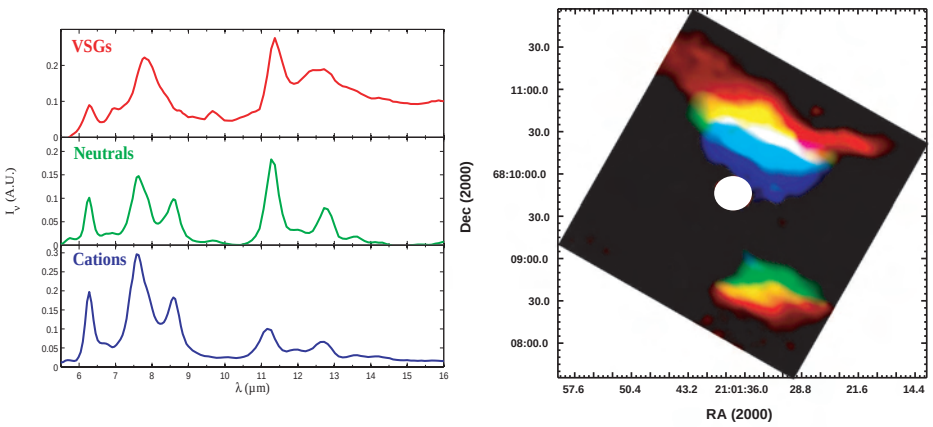

Figure 3.1: The three principal components extracted in Rapacioli *et al.* (2005), assigned to Very Small Grains (VSGs), PAH cations (PAH^+) and neutrals (PAH^0). Their relative weights in the reflection nebula NGC 7023 is shown in the right panel (VSG=red, PAH^0 = green, PAH^+ = red). In the following, we will refer to the VSGs as evaporating VSGS (eVSGs). The evaporation process is evidenced by the frontier between the VSGs and the PAHs on the right panel. *Image courtesy of O. Berné.*

An evolutionary scheme between aliphatic and aromatic carbonaceous materials is also suggested by observational evidence. Two broad features at 8 and 12 μm are detected in post-AGB stars and PPNe but not in late type PNe (Peeters *et al.*, 2002). On the other hand, AIB emission is detected in both PPNe and PNe, but not in the earlier phases. The two broad features are generally attributed to materials containing both aliphatic and aromatic hydrocarbons (Kwok, 2004). A systematic study of several PPNe and PNe by Joblin *et al.* (2008) supports the scenario in which the carriers of the broad features are destroyed in PNe, producing the AIB carriers. Furthermore, PPNe and PNe show intense band emission at 3.4 μm, which is attributed to aliphatic side groups in PAHs (Joblin *et al.*, 1996a) or super-hydrogenated PAHs (Bernstein *et al.*, 1996). Indeed, several observations of spatially resolved PDRs (Geballe *et al.*, 1989; Joblin *et al.*, 1996a; Sloan *et al.*, 1997) show that the intensity ratio of the 3.4 and 3.3 μm bands increases in the more shielded regions. This has been interpreted as the photo-destruction of the more fragile aliphatic bonds.

Ionisation of PAHs

There is compelling evidence for the presence of PAH cations in the ISM (Joblin *et al.*, 1996b; Sloan *et al.*, 1999). The spectrum of ionised PAHs differs from that of neutrals in particular by its band intensity ratio. It shows higher values of the 3.3, 11.3 and 12.7 μm over 7.7 μm intensity ratio, whereas in ionised PAHs the opposite tendency is seen.

The studies of Rapacioli *et al.* (2005) and Berné *et al.* (2007) presented further evidence for the presence of PAH cations in PDRs and opened the way to study the evolution of PAH-related populations in different environments using a simple set of template spectra. This was applied to PNe (Joblin *et al.*, 2008), proto-planetary disks (Berné *et al.*, 2009b) and H II regions (Berné *et al.*, 2009a). Joblin *et al.* (2008) and Berné *et al.* (2009a) showed that a fourth PAH population was needed to accurately fit the spectra of PNe and PPNe, and Proto-Planetary disks. The spectral features of this fourth population, together with the fact that its emission is important in highly irradiated sources, led the authors to associate it to large ionised (cationic or anionic) PAHs. In these works, the authors showed a correlation between the emission associated to the different populations and the physical characteristics of the source, evidencing the chemical evolution of the carriers, in particular photo-ionisation and photo-dissociation of PAHs and eVSGs.

Dehydrogenation and photo-dissociation

Loss of hydrogen atoms by PAHs can also be very efficient in interstellar conditions. This process has been modelled for diffuse ISM conditions by Le Page *et al.* (2003), who showed that larger PAHs are much more hydrogenated than smaller species. However, large uncertainties remain in the description of the reactivity of PAH-related species with H and H_2 and their dissociation rates. The minimum size of PAHs that can be found in their normal hydrogenated state was evaluated to be in the 25-50 C atom range, depending on the G_0/n_H ratio.

PAHs can be dissociated by UV photons in the ISM. The loss of hydrogen atoms at the periphery of the carbon skeleton can be in competition with the ejection of small hydrocarbons (mainly C_2H_2 and C_4H_2, Useli Bacchitta and Joblin, 2007; Useli Bacchitta, 2009) in the gas. This process can contribute to the production of small hydrocarbons in PDRs. Fuente *et al.* (2003), Teyssier *et al.* (2004) and Pety *et al.* (2005) indeed showed that models fail to reproduce the high abundance of hydrocarbons (C_2H, C_4H, c-C_3H_2, ...) that is observed in the outer layers of several PDRs. Pety *et al.* (2005) showed a good spatial correlation of the emission in these hydrocarbon lines with that of the AIBs for the Horsehead Nebula PDR (see Fig. 3.2), supporting a scenario in which these hydrocarbons are produced by destruction of the AIB carriers.

3.2 Energetics of PDRs

The thermal balance of the gas in PDRs results from the competition between heating and cooling:

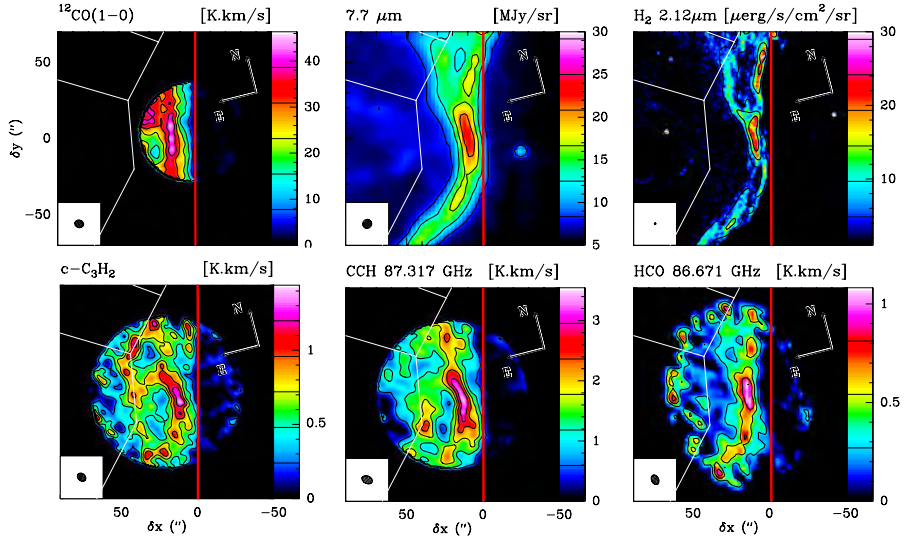

Figure 3.2: The Horsehead Nebula observed with different tracers. The 7.7 μm image tracing PAH emission (ISOCAM data, Abergel *et al.*, 2003) and the hydrocarbon emission (Plateau de Bure Interferometer data, Pety *et al.*, 2005) are spatially coincident. For reference, the H_2 2.1 μm (Habart *et al.*, 2005) and ^{12}CO emissions are displayed. *Image adapted from Gerin* et al. *(2009).*

Photo-electric heating. The most important heating mechanism at the border of PDRs is known to be photo-electric heating by (small) dust grains (Bakes and Tielens, 1994; Weingartner and Draine, 2001). If the energy of the photon is higher than the ionisation potential, the excess energy is released as kinetic energy of the ejected electron. The **photoelectric heating efficiency** (ϵ_{ph}) is a fundamental parameter that is defined as the fraction of far-UV energy which is converted to gas heating. The photo-electric efficiency depends on the physical properties of the grain, such as its size and ionisation state. In positively charged grains, the electron must have enough energy to overcome the ionisation potential and to pass the Coulomb barrier. Therefore, positively charged grains contribute less to photoelectric heating. Furthermore, the efficiency of larger grains is limited by the escape length of photo-electrons: half of the photo-electric heating is most likely due to grains of a few tens of Å. PAHs, in particular, are expected to be a very important source of photo-electrons.

In PDRs, ϵ_{ph} is often measured observationally as the ratio of the cooling energy emitted in the [C II] and [O I] lines and the energy emitted in the far-IR continuum that depends on the far-UV flux. An accurate measurement of ϵ_{ph} requires also to take into account other important cooling lines such as CO and H_2. The value of ϵ_{ph} has been found to vary by about 2 orders of magnitude in different sources of the ISM. For instance, Vastel *et al.* (2001) measured a very low heating efficiency $\epsilon_{ph} = 1.4 \times 10^{-4}$ cm^{-3} in the PDR of W59N, which is a highly-irradiated source that possibly contains a large fraction of ionised dust particles. In a low-UV irradiated PDR, L1721, Habart *et al.* (2001) found $\epsilon_{ph} \sim 0.03$. This confirms that dust composition and charge play indeed a

major role in the heating process. Understanding dust evolution in PDRs is a fundamental step in the description of the thermal balance of PDRs.

Cooling. The gas in PDRs can be cooled by several processes. The most efficient process in the outer edges of the PDR is the emission of collisionally excited far-IR fine structure lines of the most abundant species: C I, C II, O I, S I with ratios that depend on the physical properties of the region. Emission of [O I] at 63 and 146 μm is expected to dominate the radiative cooling in highly-irradiated ($G_0 > 10^3$) and high density ($n_H > 10^4$ cm^{-3}) regions, while [C II] emission at 158 μm dominates in regions with lower density and radiation field. The ratio between the [C II] and [O I] cooling rates can be used as a tool for determining the physical conditions (G_0 and n_H) of a PDR (Kaufman *et al.*, 1999). At high temperature, emission of near- and mid-IR ro-vibrational lines of H_2 can also contribute to gas cooling. Emission in the lines of [C I], CO and other very abundant molecules can also play a significant role in the gas cooling at moderate cloud depths.

PDR models need to solve the thermal balance of the gas, which requires a proper description of the physics of the heating and cooling mechanisms. Even though these processes are quite well understood, the quantitative description of the heating depends on the properties of PAHs and dust grains. This can be achieved by a comparison of models with observations. However, these observations are often very demanding, and before the *Herschel* Space Observatory, they were difficult. For instance, to constrain the contribution of the PAH-related populations to the photo-electric heating of the gas, one needs to disentangle the spatial structure of the AIBs, the [C II] and [O I] lines and the far-IR continuum. This demands high spectral and spatial resolution observations in the far-IR, that *Herschel* is nowadays providing. Finally, to interpret the observations, not only models are needed but also an (accurate) knowledge of the geometry of the source being studied.

3.3 OBJECTIVES OF THIS THESIS

In this thesis, I will present how observations at different wavelengths can be combined to get further insights into chemical and physical process involving very small dust particles in PDRs.

3.3.1 THE EVAPORATION OF eVSGs

Previous observational and modeling works (Rapacioli *et al.*, 2005; Berné *et al.*, 2007; Compiègne *et al.*, 2008) have shown that an evaporation process involving very small dust particles is an important process in the evolution of carbonaceous species in the

ISM. However a direct, observational link with the physical conditions (i.e. the intensity and hardness of the radiation field and the local gas density) is still missing.

In this thesis, I will present the observational study of the evolution of the different AIB carriers under UV irradiation in PDRs. In particular, I will quantify the evaporation of the eVSGs as a function of the local physical conditions in the PDR. In Chap. 5, I will present the method I have developed to interpret the mid-IR emission of very small dust particles in PDRs. In Chap. 6, I will apply this method to a sample of PDRs presenting very different physical conditions, and quantitatively interpret the results in terms of the evaporation process involving eVSGs and PAHs and the carbon content in each of these species.

In Chap. 8, I will show how this photo-destruction process may be related to the chemistry of small gas-phase hydrocarbons in PDRs, by combining data at near-IR, mid-IR and mm wavelengths. In particular, I will correlate the aliphatic-aromatic transitions observed in the near-IR with the results of the mid-IR analysis, and with the interferometric observations at mm wavelengths.

3.3.2 Search for a specific PAH: corannulene

As already mentioned in Sect.2.3, the PAH hypothesis lacks the identification of a specific PAH molecule in the ISM. In Chap. 7, I will present the first search at mm wavelengths for a specific PAH, corannulene ($C_{20}H_{10}$), in the nebula of the Red Rectangle, that have led to a very strict upper limit to its abundance in this post-AGB environment.

Moreover, the formation mechanism of PAHs in the ISM is still subject of debate, being related to chemical accretion of smaller species, or to the destruction of larger particles (Sect. 3.1.1). I will show how corannulene can be used as a probe of the small PAH population, and discuss the influence of its non-detection on our current knowledge of the formation process of small PAHs in post-AGB environments.

3.3.3 Physics and chemistry in a template PDR: NGC 7023

Numerical models of PDRs such as the Meudon code[1] progress very rapidly, describing more accurately the physical and chemical processes in PDRs. However, to compare these models with observations an accurate description of the geometry of the source is needed. In the last part of this thesis, I will show how a multi-wavelength approach can be used to study the geometry of a specific source, NGC 7023. I will show how this source is indeed a template object for future quantitative analysis with PDR models of the heating and cooling mechanisms in PDRs.

[1] http://pdr.obspm.fr/PDRcode.html

Part II

Observing facilities and analysis tools

Chapter

4

Observing gas and dust particles in the ISM

4.1 Infrared and sub-mm from space

The infrared spectra of PDRs contain a wealth of spectral features. For example, the AIBs are observed in the mid-IR between 3.3 and 18 μm, where fine structure gas lines such as the forbidden [Ne II] and [Ar III] transitions as well as ro-vibrational H_2 lines are also observed. The dust extinction curve presents also two strong absorption features at 9.7 and 18 μm produced by silicate grains (Li and Draine, 2001b) and a feature at 3.4 μm corresponding to aliphatic C-H stretching modes. The continuum emission in the IR and sub-mm domains provides a unique tool to study the size, composition and temperature of larger grains. Furthermore, the sub-mm domain is rich of molecular transitions from warm and dense media. The far-IR domain contains the main PDR cooling lines, and even possibly ro-vibrational transitions characteristic of specific PAH molecules.

Often some confusion arises on the sub-divisions of the infrared part of the electromagnetic spectrum. In this manuscript, the conventions reported in Table 4.1 will be used.

Table 4.1: Subdivision of the IR and sub-mm spectral domains

	Spectral domain (μm)
Near-IR	0.7 - 5
Mid-IR	5-40
Far-IR	40-200
Sub-mm	200-900

Only very small windows in the mid-IR domain can be observed from the ground (see fig. 4.1). Except for these very small windows, the atmosphere is opaque to IR radiation and observations from space are needed. The *Kuiper Airborne Observatory* (KAO) consisted in a 91.5 cm telescope mounted on a dedicated aircraft and operating at an altitude of about 14 km. At these altitudes, the opacity of the Earth's atmosphere due to water vapour is sensibly reduced, and KAO was able to perform observations in the IR and sub-mm domain between 1 and 500 μm. KAO operations started in 1975 and lasted for 20 years. The first infrared space mission was the *InfraRed Astronomical Satellite* (IRAS, Neugebauer *et al.*, 1984) that was launched in 1984 and mapped more than 90% of the sky in four different IR filters: 12, 25, 50 and 100 μm. Since then, many progresses have been made with the Infrared Space Observatory, the *Spitzer* Space Telescope and the AKARI telescope followed for the far-IR by the *Herschel* Space Observatory.

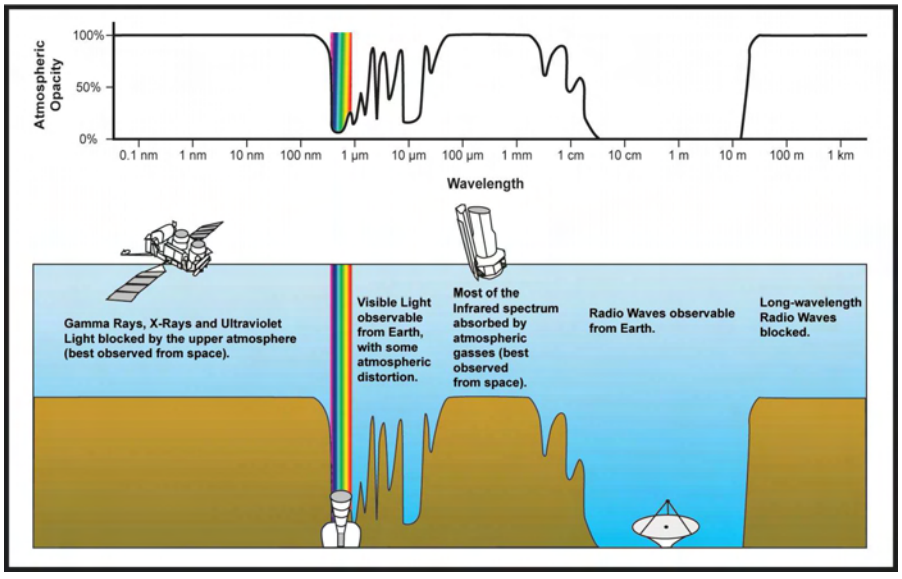

Figure 4.1: Transmission of the Earth's atmosphere along the electromagnetic spectrum. Source: ESA/NASA

4.1.1 Infrared Space Observatory

The *Infrared Space Observatory* (Kessler, 1999), better known as ISO, was launched in November 1995 and its routine phase lasted for 28 months. After the all-sky photometric observations of IRAS, ISO provided the opportunity to perform specific on-demand observations to assess different science topics (for some of the mission highlights, see Salama, 2004). ISO observed the infrared sky between 2.5 and 240 μm and was equipped with a 60 cm telescope cooled by liquid helium to temperatures of 2-4 K. Some of the detectors were directly coupled to the helium tank, and were cooled down to a temperature of about 2 K, ensuring a sensitivity thousands times better than IRAS. The angular resolution of ISO was also much better than IRAS. All ISO data are public and can be retrieved from the *ISO Data Archive*[1], in fully reprocessed and calibrated format. ISO was equipped of the following instruments:

ISOCAM (Cesarsky *et al.*, 1996) An infrared camera that covered the 2.5-17 μm band, either with several individual filters, or with a circular variable filter (CVF) providing spectro-imagery at a spectral resolution of $R \sim 45$. The long-wavelength detector (4-17 μm) had a much better performance than the short wavelength one. The spatial resolution varied between 1.5 and 12″ per pixel.

ISOPHOT (Lemke *et al.*, 1996) A photo-polarimeter with the task of mapping the sky in several filters in the 2.5-240 μm range. It could also be used as a Spectrophotometer at medium spectral resolution ($R \sim 90$) in the 2.5-12 μm range.

SWS (de Graauw *et al.*, 1996) The Short-Wave Spectrometer could perform high resolution spectroscopic observations covering the 2.4-45 μm band at low ($R \sim 1000 - 2000$) or high spectral resolution ($R \sim 3 \times 10^4$). The area of the aperture varied between 14 and 40 arcsec^2.

LWS (Clegg *et al.*, 1996) The Long-Wave Spectrometer provided for the first time high sensitivity spectroscopic information in the far-IR (43-196.7 μm). at low ($R \sim 200$) or high spectral resolution ($R \sim 10^4$). The radius of the effective aperture of LWS varied between 33 and 43″.

4.1.2 Spitzer Space Telescope

The *Spitzer Space Telescope* (or *Spitzer*) (Werner *et al.*, 2004a) was developed by NASA and launched on August 2003. *Spitzer* improved our knowledge of the infrared sky thanks to its better sensitivity compared to ISO. The instruments were cooled down to 1.4 K, and the entire telescope was kept to about 40 K for routine observations. *Spitzer* covered the 3-180 μm range and was equipped with a 85 cm-diameter mirror. The angular resolution of all the instruments were diffraction limited at wavelengths higher than 5.5 μm. *Spitzer* disposed of the following instruments:

[1] http://www.iso.vilspa.esa.es

IRAC (Fazio *et al.*, 2004) The InfraRed Array Camera was a photometer covering simultaneously 4 filters in the near- and mid-IR at 3.6, 4.5, 5.8 and 8 μm. Each channel covered a field of view of $5.2' \times 5.2'$ with a pixel size of $\sim 1.5''$.

MIPS (Rieke *et al.*, 2004) The Multiband Imaging Photometer for Spitzer (MIPS) could image the sky with three filters at 24, 70 and 160 μm, with an angular resolution of $6''$, $18''$, and $40''$, respectively. MIPS could also be used in the spectral energy density (SED) mode, where the whole 55-95 μm range can be observed with a spectral resolution $R \sim 15 - 20$.

IRS (Houck *et al.*, 2004) The InfraRed Spectrograph was an imaging spectrometer, covering the 5.5-38 μm range. The instrument was split in four modules, two for the low resolution observing mode ($R \sim 64 - 128$) called short-low (SL) and long-low (LL), and two for the high resolution ($R \sim 600$), called short-high (SH) and long-high (LH). The pixel size for the SL module is $1.8''$, which enabled to sample the point spread function of IRS at these wavelengths ($3.6''$), while for the LL module it was $5.1''$.

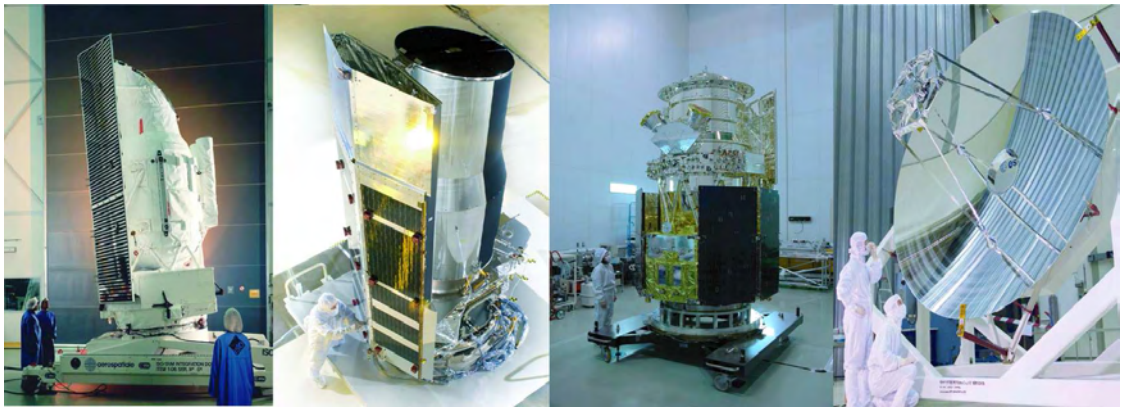

Figure 4.2: From left to right, the ISO, *Spitzer*, AKARI and *Herschel* space telescopes. Sources: ESA, NASA, JAXA, and ESA

4.1.3 AKARI

AKARI (Murakami *et al.*, 2007) (which means *light* in japanese) is an infrared satellite developed by the Japan Aerospace Exploration Agency (JAXA) that was launched in February 2006. Its main goal was to provide an all-sky map in several filters in the near-, mid- and far-IR, with a much better sensitivity and angular resolution than IRAS. With its 68.5 diameter mirror, AKARI mapped the 90% of the IR sky during its 15 months lifetime. In August 2007, the liquid helium reservoir finished, and the mid- and far-infrared observations ended. AKARI was equipped with the two following instruments:

FIS (Kawada *et al.*, 2007) The Far-Infrared Surveyor, a photometer capable of imaging the whole sky in four far-infrared bands at 65 and 90 μm (pixel size of 27 arcsec^2) and at 140 and 160 μm (pixel size of 44 arcsec^2).

IRC (Onaka *et al.*, 2007) The InfraRed Camera consists of three cameras covering the 1.8-26 μm range in 9 bands with fields of view of approximately 10″ ×10″. The near-IR (NIR) camera could also be used for slit spectro-imagery (2-5 μm)

4.1.4 Herschel Space Observatory

The previous space missions were mostly concentrated in the near- and mid-IR part of the electromagnetic spectrum, and provided only scarce information in the far-IR, mainly consisting in photometric images at low angular resolution and average resolution/sensitivity spectroscopy. The *Herschel* Space Observatory (*Herschel*, Pilbratt *et al.*, 2010) offers a new set of tools to observe the far-IR and sub-millimeter domains, covering the 56-671 μm spectral range with its three instruments. This observatory has a 3.5 m diameter telescope, providing a high angular resolution at these wavelengths, $\sim 7'' \times (\lambda_{obs}/100\mu m)$, and its instruments are cooled down to 0.3 K to provide excellent sensitivity. The observatory was launched on May 2009 and the operational phase will last for about 3.5 years. The last open time call for proposal (OT-1) was closed on July 22th, 2010 and offered 6592 hours of observing time. The observatory disposes of the following instruments:

HIFI (de Graauw *et al.*, 2010) The Heterodyne Instrument for the Far Infrared (HIFI) is constituted by 7 receivers tuneable in the ranges 480-1250 GHz (612-240 μm, bands 1-5) and 1440-1910 GHz (157-208 μm, bands 6 and 7). The most important characteristics of HIFI are its stunning spectral resolution (up to $R \sim 10^7$) and sensitivity. HIFI can be used in mapping or single pointing mode, with angular resolution between 10″ and 40″ at 1910 and 480 GHz, respectively. HIFI is equipped with double side band (DSB) receivers: for each polarisation, two frequency ranges are simultaneously covered with a single observation, separated by about 8 GHz. The band width of the receivers are 4 GHz for bands 1 to 5 and 2.4 GHz for bands 6 and 7. The whole bandwidth is processed by a Wide Band Spectrometer (WBS, $\Delta\nu \sim 1$ MHz), and multiple High Resolution Spectrometers (HRS) can be set for a single observation.

PACS (Poglitsch *et al.*, 2010) The Photodetector Array Camera and Spectrometer (PACS) can be operated either as an imaging photometer or as an imaging spectrometer. Its spectrometer receivers consist in two photoconductor arrays of 16×25 pixels and the photometer detectors are bolometer arrays. When used as a photometer, PACS can simultaneously map a field of view of $\sim 1.75' \times 3.5'$ in two different far-IR bands, either the 60-85 μm or 85-125 μm (the so-called blue channels) and 125-210 μm (the red channel) with almost Nyquist sampling. When used as a

spectrometer, the total field of view covered is $47'' \times 47''$ in a 5×5 spatial pixels array sizing $9''$. The spectral resolution of this mode can be varied between $1000 < R < 5000$.

SPIRE (Griffin *et al.*, 2010) The Spectral and Photometric Imaging Receiver (SPIRE) is an imaging photometer and an imaging Fourier Transform Spectrometer (FTS) operating between 194 and 671 μm (447-1550 GHz). As a photometer, SPIRE simultaneously maps the sky at 250, 350 and 500 μm, in a field of view of 4.8' $\times$ 4.8'. The spectrometer observing mode uses 37 detectors in the short wavelength array and 19 in the long wavelength array, with a circular field of view of about 2.6' diameter. The beam width of the short wavelength detectors is $33''$, whereas for the long-wavelength detector is $51''$. The FTS mode covers in one single observation the whole spectral domain of SPIRE, with a spectral sampling between 1.2 GHz and 25 GHz.

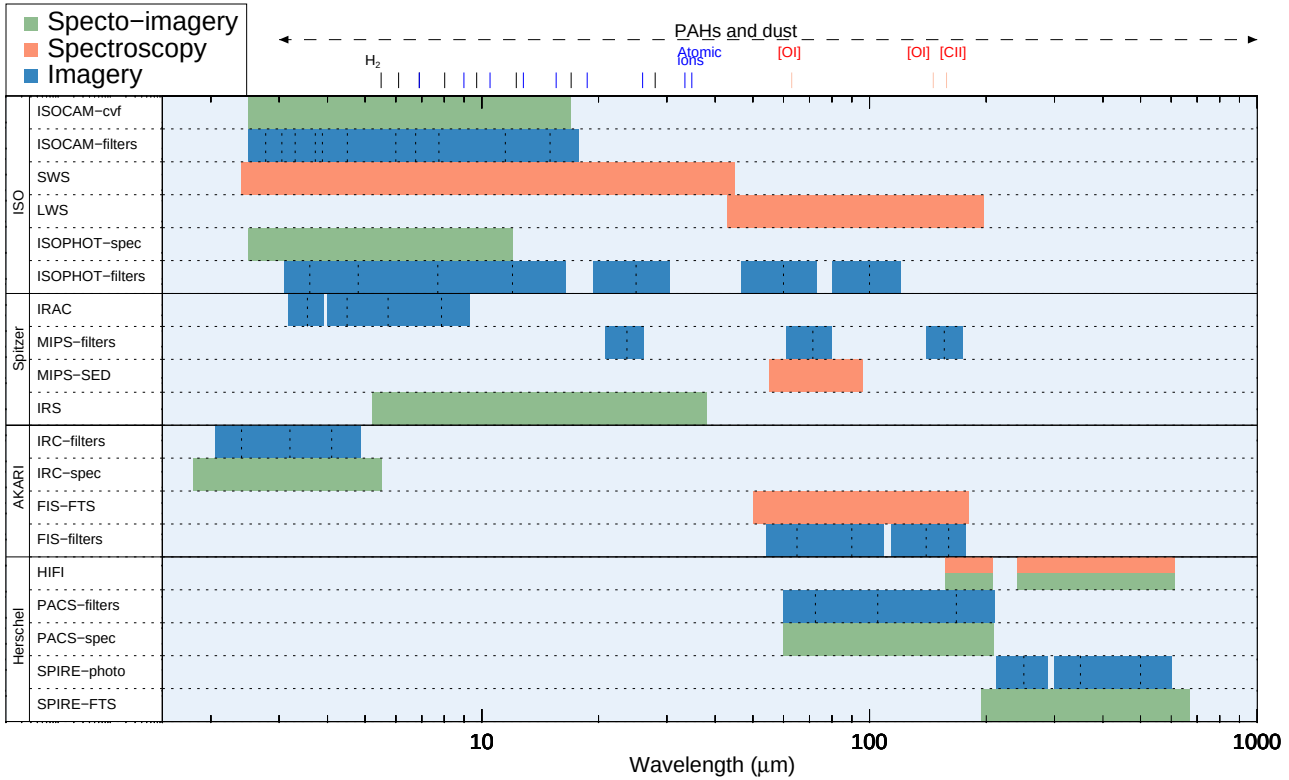

Figure 4.3: Summary of the wavelength coverage for the instruments onboard ISO, *Spitzer*, AKARI and *Herschel*, in their spectroscopy, spectro-imagery or photometry observing modes (OMs). For photometry OMs, the centers of the passbands are displayed with vertical lines, as well as the total passband. HIFI is designed for spectroscopy, but is able to produce spectral cubes in its On-The-Fly mode.

Figure 4.4: *Left:* The IRAM 30 m telescope in Pico Veleta. *Right:* The IRAM Plateau de Bure interferometer. *Sources: www.iram.fr*

4.2 RADIO ASTRONOMY IN THE MILLIMETER DOMAIN

Figure 4.1 shows that the Earth's atmosphere is almost transparent to millimeter wavelengths, except for a few bands. The exact limits and transmission in the observable bands depend on the site and on the atmospheric conditions. Astronomical sources can emit in the mm domain through several physical processes such as dust thermal emission, spectral line radiation and free-free emission. Since the first observation of the OH molecule by Dieter (1964), more than 125 molecules have been identified in the ISM by radio astronomical observations.

4.2.1 IRAM 30M TELESCOPE

The IRAM 30m telescope is one of the largest and more sensitive single-dish millimeter telescope, located on Pico Veleta (2850 m altitude) in the Sierra Nevada (Spain). The telescope is equipped with a series of heterodyne receivers that are used to detect line radiation in the 0.8-3 mm domain and 1.2 mm bolometers used for continuum mapping. The telescope beam size varies from 9″ at the highest frequencies to about 30″ at 3mm.

EMIR consists of single pixel DSB receivers with 2×4 GHz bandwidths in the two polarisations. It substituted the old ABCD receivers in 2008. The system configuration is highly customisable, so that several spectral domains are accessible at the same time. The receivers are connected with the high resolution VESPA spectrometer, and simultaneously with WILMA, the 2 MHz resolution spectrometers that cover the full receiver bandwidth. The VESPA receivers are very versatile, allowing a large number of bandwidth-spectral resolution configuration, and can be set in the receiver upper side band (USB) or lower side band (LSB).

HERA This HEterodyne Receiver Array is a receiver system tuneable between 215 and 272 GHz, that consists in a 3x3 dual polarisation pixel array. The main purpose

of this spectral line receiver is to image large maps of extended sources in on-the-fly mode very efficently. The main beam size at these frequencies at the 30m telescope is between 12″ and 9″.

MAMBO is a large field bolometer camera operating at 1.2 mm, with a beam size of 11″. It is a very sensitive and efficient continuum receiver, and it is used to map dust emission over large areas of the sky.

4.2.2 IRAM Plateau de Bure Interferometer

The Plateau de Bure Interferometer (PdBI) is located at 2550 m on the Plateau de Bure in the French Alps. It consists of an array of six 15 m diameter antennas, which can be positioned to have a maximum baseline length of 760 m (E-W direction) and 368 m (N-S direction). Such large baselines permit to achieve an angular resolution down to 0.5″ at 1 mm. Even in its most compact configuration (the D configuration) and at 3 mm, the angular resolution of the PdBI is 5″, which is better than the best beam size obtainable at 0.8 mm at the 30 m telescope. The interferometer has an instantaneous field of view of $\sim$ 40″ at 3 mm. Since the interferometer filters the shortest spatial frequencies, the PdBI is often used in combination with the 30m telescope to retrieve the total flux in extended sources. The receiver can be used either in single side band (SSB) or DSB mode, and has a 4 GHz bandwidth. Up to 8 backends, both for spectral line and continuum measurements, can be used at the same time.

4.3 One step in the future

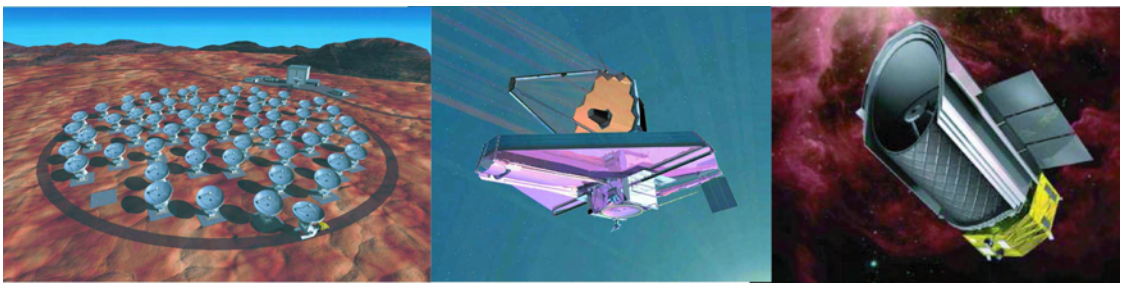

Figure 4.5: The ALMA interferometer array and the JWST and SPICA telescopes *Sources: NRAO / AUI / NSF, NASA and JAXA*

4.3.1 SOFIA

The Stratospheric Observatory for Infrared Astronomy (SOFIA) is the successor of the KAO mission, and consists in a 2.5 m telescope onboard a Boeing 747. SOFIA will be a

very versatile facility, equipped by several instruments covering most of the IR and sub-mm range. Initially, it will be equipped with imaging instruments covering the near-IR (1-5 μm FLITECAM), mid-IR (5-40 μm, FORCAST), and far-IR/sub-mm (40-400 μm, HAWC), and with spectrometers covering the whole observable range. SOFIA saw first light in May 2010 providing imagery of the M 82 galaxy. First science operations are scheduled to begin in 2011, and SOFIA will be fully operational in 2014.

4.3.2 ALMA

ALMA, the Atacama Large Millimeter/sub-millimeter Array, will be the largest mm and sub-mm interferometer of the world, being constituted by more than 60 antennas, and located in the District of San Pedro de Atacama (Chile), at an altitude of 5000 m. ALMA will operate at wavelengths of 0.3 to 9.6 mm and will provide an unprecedented sensitivity and angular resolution at these wavelengths. The antennas will have configurable baselines ranging from 15 m to 18 km. Resolutions as fine as 0.005" will be achievable at the highest frequencies. The call for early science with ALMA will be opened at the beginning of 2011.

4.3.3 NOEMA

The NOEMA (Northern Extended Millimeter Array) project consists in a major upgrade of the IRAM Plateau de Bure Interferometer, which will double the number of antennas of the current array, improving drastically both the spatial resolution and resolution of the PdBI. The spatial resolution available with the more extended configuration will be of $\sim 0.1''$. NOEMA will be the largest interferometer operating at mm wavelengths in the northern hemisphere, complementary to ALMA.

4.3.4 JWST

The James Webb Space Telescope (JWST) will be the largest infrared telescope ever launched in space, with its 6.5 m diameter mirror. It will be mainly designed to work in the near- to mid-IR part of the spectrum, even though it will have also some capabilities in the visible part of the spectrum. The telescope is scheduled for launch in 2014, and will provide the best angular resolution and sensitivity in these spectral domain. JWST instruments will consist in a Near Infrared Camera (NIRCam), a Near Infrared Spectrograph (NIRSpec), the Mid-Infrared Instrument (MIRI) and the Fine Guidance Sensor Tuneable Filter Camera (FGS-TFI).

4.3.5 SPICA

The Space Infra-Red Telescope for Cosmology and Astrophysics (SPICA) will be the following infrared telescope and is planned to be launched in 2017. The telescope primary mirror of 3 m diameter will be cooled to 4.5 K, providing a high sensitivity in the

far-IR range. The planned instruments to be placed onboard SPICA are SAFARI, a European 30-200 μm imaging spectrometer, an imaging coronograph and a high resolution spectrometer for the mid- and far-IR.

4.4 Combination of spectro-imagery data

The IR, sub-mm and mm domains can be used to study the different physical and chemical processes found in PDRs. In the near- and mid-IR, the emission from PAHs and very small dust particles, H_2 and ionised atomic species reveal the warmer part of PDRs. The far-IR and sub-mm domains can be used to study the emission from warm and dense gas and dust such as the [O I] and [C II] cooling transitions. Finally, the mm domain is rich in molecular transitions arising from the cooler interior of PDRs. To study the physical and chemical processes involved in PDRs, observations in these different domains have to be used. The combination of different instruments is often not straightforward, due to differences in the characteristics of the instruments and data handling.

4.4.1 Spectral resolution

The spectral resolution of an instrument is defined as $R = \frac{\lambda}{\Delta\lambda}$ where $\Delta\lambda$ is the smallest difference in wavelengths between two features that can be distinguished, at a wavelength λ. In the IR domain, the instruments onboard ISO and *Spitzer* enabled spectro-imagery observations with R = 45 (ISOCAM-cvf), 80 (IRS-SL), and 600 (IRS-SH). In the mm domain the heterodyne receivers enable much higher spectral resolution ($R \gtrsim 10^7$) that is adapted to distinguish velocity structures in the gas lines and therefore to perform kinematics studies. The HIFI instrument onboard *Herschel* extends this capability to the sub-mm range.

4.4.2 Spatial resolution

The angular resolution of an ideal optical instrument depends on the observed wavelength λ and on the telescope diameter D, and is given by the diffraction pattern:

$$\sin\theta = 1.22\frac{\lambda}{D} \tag{4.1}$$

in which θ is the angular distance (in radiants) of two points that are resolved by the instrument. The imaging capabilities of an instrument depend also on the optical design of the instrument. Often, the optics are designed such that the pixel size samples the point spread function of the instrument following the Nyquist criterium.

IR spectro-imagery

To perform spectroscopy in the IR, one needs to observe from space, since only few windows are available from the ground due to the atmospheric opacity (cf Sect. 4.1).

The telescope size for a space telescope is limited due to technical reasons. The IRC (AKARI), IRS (*Spitzer*) and ISOCAM (ISO) instruments provided spectral mapping observing modes in the near- and mid-IR that are limited to few arcseconds in spatial resolution. In particular, the circular variable filter observing mode of ISOCAM allowed spectro-imagery observations with 6″ resolution in the mid-IR (5.5-15) μm. The spatial resolution in this domain was then improved by the SL module of IRS, which provided a similar spectral coverage with a higher (3.6″) spatial resolution, which was sampled following the Nyquist criterion.

The millimeter domain

Observing in the millimeter domain using ground-based facilities is easier since the atmosphere is less opaque over wider frequency ranges. The IRAM 30m telescope has an angular resolution (or beam size) comprised between 9″ (at 1 mm, $\sim$ 300 GHz) and 30″ (at 3 mm, $\sim$ 100 GHz). At these frequencies, to achieve spatial resolutions comparable to that of IRS and IRC in the infrared, larger collecting surfaces as given by an interferometer are needed. The Plateau de Bure interferometer allows a spatial resolution of few arcsecs ($\sim$ 5″) at 3 mm with its most compact configurations (with baseline lengths between 24 and 229 m). However, observing with an interferometer presents some difficulties: a) the instantaneous field of view is quite small ($\sim$ 40″ in diameter) and mosaicing needs to be performed for extended regions, b) the large scale informations are filtered and the interferometric data needs to be combined with single-dish data; finally c) the data reduction is more complex and time-demanding compared to mm single-dish or IR observations.

Far-IR and sub-mm with Herschel

Herschel provided a step forward in far-IR and sub-mm observations, in terms of sensitivity, spectral and angular resolution. The HIFI, PACS and SPIRE instruments cover the 120-600 μm wavelength range. The large diameter of the telescope, 3.5 m, allows to achieve angular resolutions of 5″ (PACS, at short wavelengths), 9″ (HIFI for the [C II] line at 158 μm) and 45″ (HIFI, at the longest wavelengths). At sub-mm wavelengths, the spatial resolution obtained with *Herschel* is still larger than few arcsec, but the far-IR sky can finally be spatially resolved and more easily compared with the mid-IR and mm data. ALMA will allow to observe part of the sub-mm domain at higher spatial resolution. A sub-mm interferometer in space has still to come.

Chapter

5

Decomposing the mid-IR spectra of PDRs

5.1 Fit of the AIBs with band template spectra

Different methods have been proposed to study the variations in the mid-IR spectrum of PDRs. In general, they consist in the fit of each band with an analytical function consisting of either a Lorentzian, a Gaussian or a Voigt profile. In particular, PAHFIT (Smith *et al.*, 2007) fits at the same time the individual AIBs and the principal gas lines superimposed to a continuum and after correction for the extinction in the silicate band at 9.7 μm. Tools such as PAHFIT have been used to retrieve the variations in intensities, widths and central positions of the bands and correlate them with the characteristics of the environment (see, for example, Galliano *et al.*, 2008).

Rapacioli *et al.* (2005) and Berné *et al.* (2007) proposed a different approach which consists in the fit of the general shape of the whole mid-IR spectrum with few, physically consistent template spectra extracted using blind source separation methods. In Joblin *et al.* (2008) and Berné *et al.* (2009a), the authors constructed a set of synthetic band spectra based on these template spectra by fitting the most intense AIB features at 6.2,

7.7, 8.6, 11.3 and 12.7 μm with Lorentzian profiles. A combination of these synthetic spectra is then used to fit the observed AIB spectrum of different sources, in particular of objects in different evolutionary stages such as planetary nebulae (Joblin *et al.*, 2008) and proto-planetary disks (Berné *et al.*, 2009a). In order to fit the spectra of more highly irradiated environments, they had to introduce a fourth PAH-related component, which they attributed to large, ionised PAHs (PAH^x). The relative intensities of the different mid-IR components are found to correlate with physical quantities such as the spectral type of the central illuminating star for proto-planetary disks (Berné *et al.*, 2009a), and the ionisation parameters for the compact HII region Monoceros R2 (Berné *et al.*, 2009b).

5.1.1 The fitting model

We present here a fitting procedure that can be applied directly to the observed mid-IR (5.5-14 μm) spectrum of an AIB source, which is an update of the method of Joblin *et al.* (2008). It consists of a linear combination of the four template band spectra, gas lines, a linear continuum, and three smaller Lorentzian features (see below). Finally, a simple extinction correction is applied to take into account the absorption of silicate grains at 9.7 μm.

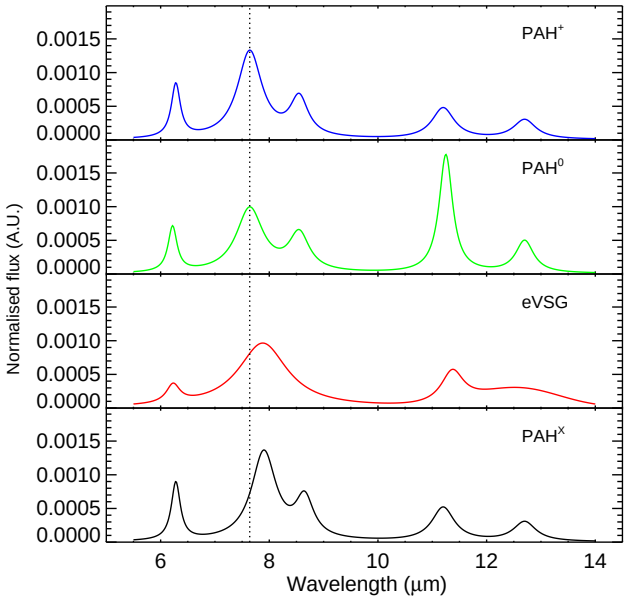

Figure 5.1: Template spectra used to fit the mid-IR spectrum of PDRs

	6.2			7.7			8.6		
	Pos.	FWHM	Int.	Pos.	FWHM	Int.	Pos.	FWHM	Int.
PAH^0	6.22	0.17	0.75	7.64	0.60	1.0	8.55	0.45	0.57
PAH^+	6.28	0.20	0.65	7.64	0.55	1.0	8.55	0.40	0.45
PAH^x	6.28	0.20	0.65	7.90	0.55	1.0	8.65	0.40	0.45
eVSG	6.23	0.30	0.64	7.88	1.10	1.0	-	-	-
	11.3			12.7					
	Pos.	FWHM	Int.	Pos.	FWHM	Int.			
PAH^0	11.25	0.3	1.60	12.70	0.4	0.54			
PAH^+	11.20	0.5	0.38	12.70	0.5	0.22			
PAH^x	11.20	0.5	0.38	12.70	0.5	0.22			
eVSG	11.37	0.5	0.32	$12.60^\dagger$	$1.7625^\dagger$	$0.3636^\dagger$			

† Parameters for a Gaussian profile

Table 5.1: The parameters for the band profiles used to build the template spectra. If not otherwise indicated, the profiles are Lorentzian. Adapted from Joblin *et al.* (2008)

PAHs and evaporating VSGs

The basis of our fitting procedure is the template spectra that are reported in Joblin *et al.* (2008) and assigned to PAH cations (PAH^+), neutrals (PAH^0), large ionised PAH^x and eVSGs. These template spectra are presented in Fig. 5.1, where they have been normalised to their integrated flux between 5.5 and 14 μm. The parameters of the synthetic spectra are reported in Table 5.1. The eVSG spectrum has been continuum subtracted as in Joblin *et al.* (2008). In the present work, it has been slightly improved to better fit the observed spectra by adding a plateau in the 12-14 μm range, which was originally present in the eVSG spectrum of Berné *et al.* (2007) (Fig. 6.1).

The continuum

The four template spectra are combined with a linear continuum, representing the linear rise of eVSGs in the 5-14 μm domain (see Fig. 6.1). In highly-irradiated objects, larger grains at thermal equilibrium can also contribute to the mid-IR continuum (Compiègne *et al.*, 2008). In such cases, the continuum is not linear anymore and a bi-linear slope is more representative of the total continuum.

Gas lines

Gas lines are fitted assuming Gaussian profiles with a fixed central wavelength and a FWHM given by the average spectral resolution R of the instrument (R = 45 for ISO-

CAM, and R = 80 for IRS). Table 5.2 reports the adopted central wavelengths and line widths for the fitting procedure.

The H_2 S(3) line is well distinguished from the PAH features. The H_2 S(6) and H_2 S(4) lines at 6.1 and 8.0 μm are strongly blended with the broad PAH features in ISOCAM/IRS low resolution spectra, and their intensity cannot be retrieved, or it is subject to large uncertainties. The H_2 S(2) and the [Ne II] lines can significantly contribute to the shape of the 12 μm complex, and their intensity can be more accurately estimated.

Line	Wavelength [μm]	FWHM$_{IRS}$ [μm]	FWHM$_{ISOCAM}$ [μm]
H_2 S(7)	5.511	0.069	0.122
H_2 S(6)	6.109	0.076	0.136
H_2 S(5)	6.909	0.086	0.153
[Ar II]	6.985	0.087	0.155
H_2 S(4)	8.026	0.100	0.178
[Ar III]	8.991	0.112	0.200
H_2 S(3)	9.665	0.121	0.214
[S IV]	10.511	0.131	0.234
H_2 S(2)	12.278	0.1153	0.273
[Ne II]	12.813	0.160	0.285

Table 5.2: Parameters for the gas lines used in the fitting procedure

Smaller features

Using all the above components, we found that three additional features are present at 6.7, 12.0 and 13.5 μm in most objects. These are likely PAH-like features and we added three Lorentzians at 6.7, 11.55 and 13.5 μm with a FWHM of 0.2, 0.4 and 0.25 μm, respectively. These are small features and their introduction does not change the results significantly.

Optical depth effect

Finally, our model takes into account extinction effects assuming that the emitting and absorbing materials in the considered column of material are fully mixed (see, for instance Disney *et al.*, 1989; Smith *et al.*, 2007).

The optical depth at each wavelength is calculated using the relation:

$$\tau_\lambda = C_{ext}(\lambda) \times N_H \tag{5.1}$$

where $C_{ext}(\lambda)$ is the extinction cross-section per H nucleon, calculated by Weingartner and Draine (2001) for $R_V = 5.5$. The hydrogen column density N_H is left as a free parameter in the fit.

The column density calculated with this method provides another diagnostic compared to other column density estimates that use mm observations. By using the AIB emission to calculate the extinction, such estimate concerns the gas associated to the PDR, i.e. only the slab of material that is emitting in the AIBs. On the contrary, the use of CO isotopes and continuum observations provide information on the whole molecular cloud, which may have a larger depth than its illuminated side (the PDR) where AIB emission arises.

Summary of the model

In summary, the model can be written as:

$$I_{model}(\lambda) = \left(I_{AIB} + I_{gas} + I_{Lorentzians} + I_{continuum}\right) \frac{1 - e^{-\tau_\lambda}}{\tau_\lambda} \tag{5.2}$$

where I_{AIB} represents the band template spectra of $PAH^{0,+,x}$ and eVSGs, I_{gas} consists in all the mid-IR H_2 and ionised gas lines, $I_{Lorentzians}$ in the features at 6.7, 11.5 and 13.5 μm and $I_{continuum}$ is the (bi-)linear continuum.

The quantity $|I_{model}(\lambda) - I_{obs}(\lambda)|$ is minimised using the IDL procedure *mpfit* (Markwardt, 2009), which uses a Levenberg-Marquardt non-linear square fitting algorithm. The number of free parameters can be modified according to the observed spectrum. For instance, ionised lines are not necessary in many mild UV-excited PDRs. Also, when sources different than PDRs are fitted (such as proto-planetary disks and PNe), broader features at 8 and 12 μm have to be included in the fit. In this work, however, we are interested in PDR spectra, and such features do not need to be taken into account.

5.2 Some examples

5.2.1 The prototype PDR: NGC 7023 NW

Single spectra analysis

As a first example, we analyze the fit results for three different regions in NGC 7023 NW at increasing distance from the star (respectively 35, 48 and 56″ along the cut shown in Fig. 6.2). The fitted spectra and the results are reported in Fig. 5.2. The three spectra show spectral variations in terms of band intensity ratios and continuum emission.

- Region (1) is located in the cavity between the star and the PDR front, at a distance of 35″ from the star. The spectrum shows a high ($I_{7.7}/I_{11.3}$), suggesting that band emission is dominated by ionised PAHs, which is consistent with the fit results.

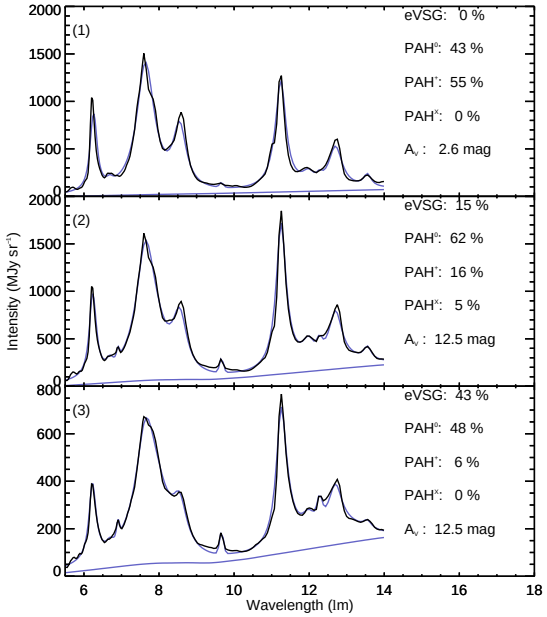

Figure 5.2: Example of the fit in three different regions of NGC 7023 NW observed by IRS at an average spectral resolution $R \sim 80$. For each spectrum, we report the relative weights of the integrated intensities of each PAH population and eVSGs and the estimated column densities (expressed in magnitudes of visual extinction).

- Region (2) is on the PDR border, at the interface of the diffuse region and the molecular cloud, at a distance of 48″. The $(I_{7.7}/I_{11.3})$, ratio is lower, indicating an higher abundance of PAH^0 compared to region (1).

- Region (3) is further inside the cloud, at a distance of 56″. Here, the relative weight of PAH^+ is negligible, and eVSGs are predominant, as expected in a region more protected from the UV radiation.

5.2.2 Spectral mapping: M 82

A direct application of this analysis tool is to determine the spatial distribution of the fit components in sources observed in spectro-imagery in the mid-IR. This yields maps of the integrated intensity for each of the components. In the next chapter, we will present the results of this procedure for several galactic PDRs. As a first example, we applied our fitting procedure to the *Spitzer* IRS spectral cubes of the M 82 galaxy. Engelbracht *et al.* (2006) showed that PAH emission is detected towards the galactic plane as well as in an outflow perpendicular to it, and Beirão *et al.* (2008) studied the spectral AIB variations in these environments. Our procedure allows to disentangle the relative contribution of the $PAH^{0/+/x}$ and eVSG to the total AIB emission, as well as the intensity of the [Ar II] line and the column density for all the spatial pixels in the IRS observations.

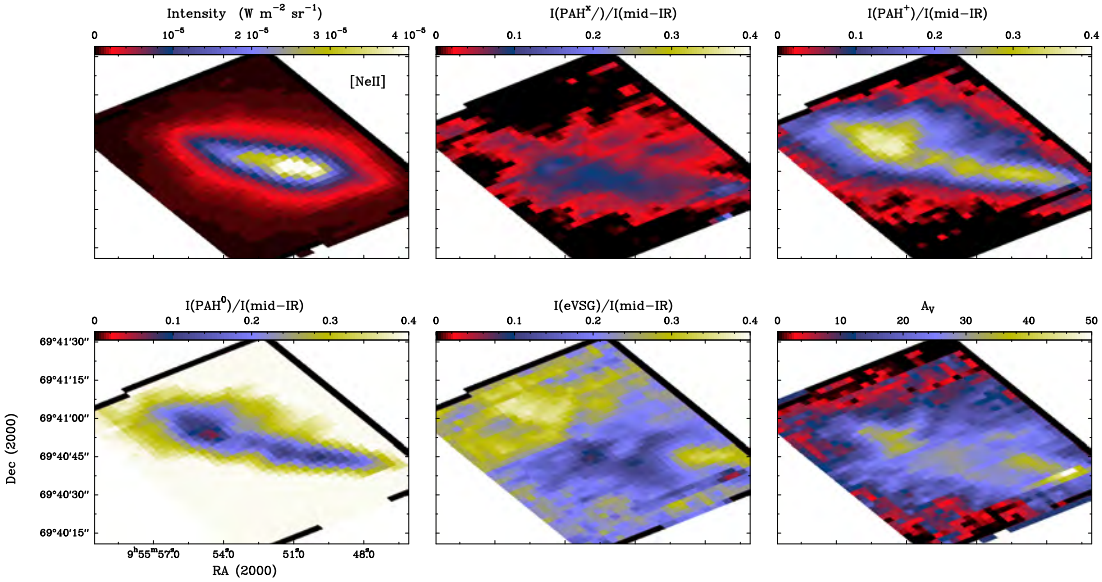

Figure 5.3: Decomposition of the *Spitzer* IRS spectral cube for M82. The relative contribution of the four principal components to the mid-IR (5.5-14 μm) flux four PAH-related components are shown , as well as the intensity of the [Ar II] intensity and the column densities.

The relative contributions of the different populations to the AIB flux are displayed in Fig. 5.3. PAH$^+$ and PAH^x dominate the emission towards the galactic plane, where star formation is taking place and the UV field is stronger compared to the outflow, whereas PAH^0 dominate the emission in the latter. eVSGs dominate the emission in the north-eastern end of the galactic plane and the column density peaks in several distinct regions towards the nucleus. Such variations can be used to obtain new insights into the physical conditions and the geometry of the source.

5.3 Caveats

5.3.1 IRS spectral resolution

The PAH template spectra were obtained from ISOCAM spectro-imagery data, at a spectral resolution that is lower than that could be achieved by the Spitzer IRS instrument. Repeating the signal processing analysis of Berné *et al.* (2007) to the IRS data of NGC 7023 NW we found that the PAH bands have comparable widths but with additional sub-structure. The higher-resolution data show also small variation in the integrated intensities and the peak positions of the bands. In particular, the 6.28 μm band of PAH$^+$ is shifted to 6.23 μm. The major difference in band intensities concerns the 8.6 μm band which is fainter in the new PAH^0 spectra and stronger in the new PAH$^+$ spectra. The principal cause for these discrepancies is most likely related to the impurity of the extracted spectra, that may consist in a combination of more than one single population.

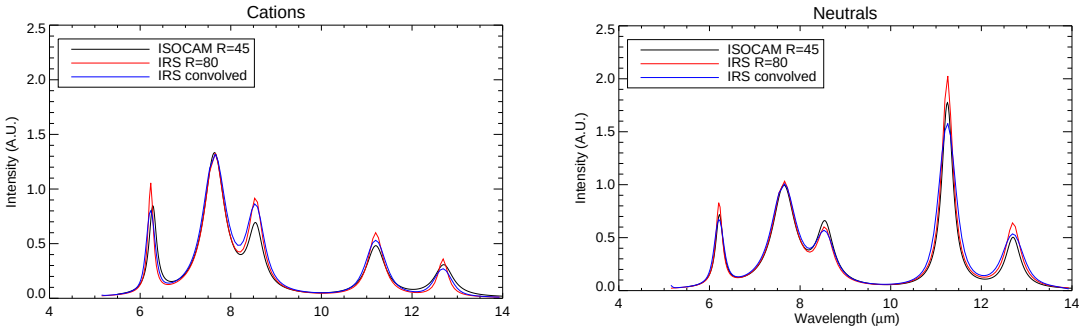

Figure 5.4: New synthetic spectra of PAH cations and neutrals fitted from the results of Blind Signal Separation on the IRS cube of NGC 7023 (black). Their convolution to R=45 (blue) are compared with the templates of Joblin *et al.* (2008, red) used in the fitting procedure.

The use of higher resolution spectra would therefore add some complexity and is not necessary for this work dedicated to eVSGs. Therefore, we used as templates the lower resolution spectra of Joblin *et al.* (2008), with the additional plateau in the 12-14 μm range.

5.3.2 Uncertainties in column density

We tested the effect of using different values of R_V for the extinction curve and found a difference of about 20% in the estimated hydrogen column density but no effect on the weights of the band templates when using $R_V = 3.1$ instead of $R_V = 5.5$.

Uncertainties by up to a factor 2 in the column densities are due to the fact that the correction of the extinction and the fit by a bi-linear continuum are degenerated. This is a systematic effect, and when the procedure is applied to a spectral cube, it is applied to all spatial pixels. This can result in a systematic overestimate of the column densities, but the derived spatial structure is still reasonable. A study of the parameter space is presented in Appendix A.

Part III

Chemical evolution of PAHs in interstellar and circumstellar environments

Chapter

6

Evolution of PAH-related species in PDRs

Whereas it is clear that the evolution of the eVSGs into PAHs is related to the intensity of the UV field, a quantitative description of this process is still missing. In this chapter, we will study the relative contributions to the mid-IR emission of PAHs and eVSGs in a wide range of excitation conditions using the procedure described in the previous chapter. From the results of the fit, we derive the fraction of carbon f_C locked in eVSGs and compare it to the intensity of the local radiation field.

6.1 Data sample

We selected a set of PDRs spanning a wide range of irradiation conditions. Some of these PDRs (Table 6.1) were chosen on the basis of proximity and simplicity of their geometry to study spatial variations of the mid-IR properties and physical conditions. We used observations obtained with the Short-Low (SL) module of the Infrared Spectrograph (IRS) onboard Spitzer (Werner *et al.*, 2004a) in spectral mapping mode. Data reduction was performed with the CUBISM software (Smith *et al.*, 2007) and consisted in cube assembling, calibration, correction for flux of extended source and bad pixel

removal. Three PDRs (NGC 7023 East and South, *rho*-Ophiuchus filament) were not observed with the IRS-SL instrument. For these objects, we used ISOCAM data available in the ISO data archive as highly-processed data products (Boulanger *et al.*, 2005).

6.2 Evaporating VSGs and reconstruction of their mid-IR emission

eVSGs do not only emit in bands, but also in continuum. In the observed spectra, the slope of the (bi-)linear continuum can vary significantly in different PDRs, due to variation of the excitation conditions that impact the relative contribution of grain populations to the mid-IR emission. In order to estimate the continuum emission of eVSGs, we used the following approach based on the eVSG spectrum retrieved in Ced 201 by Berné *et al.* (2007). Ced 201 is a mild-UV excited object and large grains are not expected to contribute to the mid-IR emission. We modelled this spectrum up to 14 μm using a distribution of 100 grey bodies having temperatures ranging between T_{min} and T_{max}. The emissivity was taken to be proportional to $\lambda^{-\alpha}$, with $\alpha = 0.85$, following the measurements performed on carbonaceous grains by Mennella *et al.* (1995). We found $T_{min} \sim 110$ K and $T_{max} \sim 260$ K, which is consistent with previous estimates by Rapacioli *et al.* (2005). Using the same approach as described in Rapacioli *et al.* (2005), we estimated that these temperatures correspond to eVSG sizes between 500 and 2500 carbon atoms approximately. Comparing the total integrated intensity in the bands vs continuum for eVSGs we obtained $I_{eVSG}^{bands}/I_{eVSG}^{continuum} = 0.5$.

The integrated mid-IR intensity I_0 emitted by very small dust particles can be expressed after correction for extinction as:

$$I_0 = I_{AIB} + I_{eVSG}^{continuum} = I_{PAH} + I_{eVSG}^{bands} + I_{eVSG}^{continuum} = I_{PAH} + 3 \times I_{eVSG}^{bands} \qquad (6.1)$$

In the following, the intensity in eVSG bands (I_{eVSG}^{bands}) is obtained as a result of the fitting procedure, and the total intensity in the eVSG continuum can be estimated using the ratio $I_{eVSG}^{bands}/I_{eVSG}^{continuum} = 0.5$ as determined above.

As will be shown in Sect. 6.4.2, the ratio I_{eVSG}/I_0 can be used to quantify the fraction of carbon atoms f_C locked in eVSGs compared to all carbon atoms contained in mid-IR emitters.

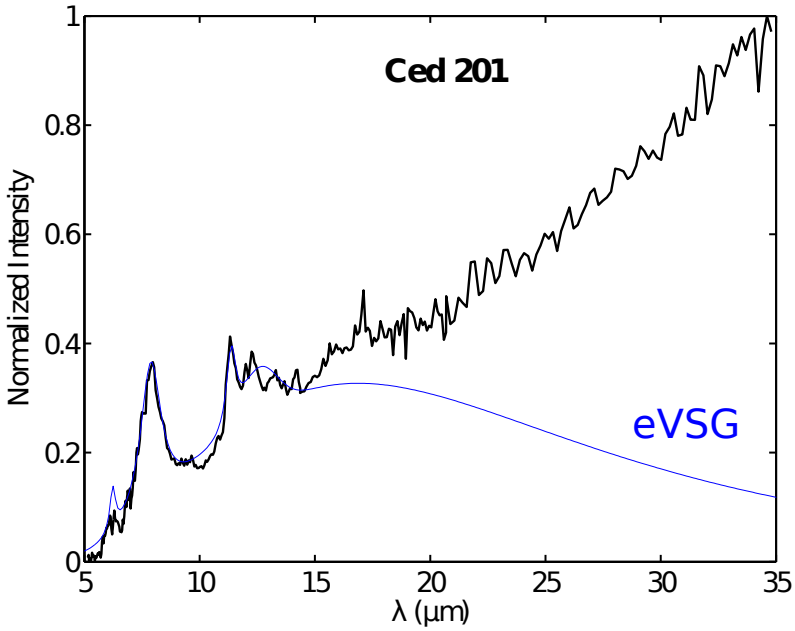

Figure 6.1: The VSG spectrum of Ced 201 (black line) extracted by signal processing algorithms by Berné *et al.* (2007) and the synthetic eVSG spectrum that has been obtained by combining the band spectrum of Fig. 5.1 with a continuum. The latter is calculated by fitting the continuum in the 5.5-14 μm with a distribution of grey bodies with temperatures between T_{min} ~ 110 and T_{max} ~ 260 K (blue line).

Object	Star	Distance (pc)[a]	Spectral Type	Kurucz Spectrum * (K)	Radius * ($R_\odot$)	d_{front} ($''$)	$G_0(d_{front})$ Habings	n_H ** (cm^{-3})
NGC 7023 NW	HD 200775	430	B3Ve — B5[b,c,d]	2×15000[e]	10	42	2600	2×10^4 [f]
NGC 7023 S						55	1500	1.4×10^4 [f]
NGC 7023 E						155	250	1.4×10^4 [f]
NGC 2023 N	HD 37903	470	B1.5V[g]	24000	6	164	400	2×10^4 [h]
NGC 2023 S						67	4000	2×10^4 [h]
ρ-Oph filament	HD 147889	118	B2III — B2V	22000	5	610	520	4×10^4 [l]

* Derived from spectral type.

** Total hydrogen density inside the molecular cloud derived from molecular observations.

Table 6.1: Input parameters for the modelling of the selected PDRs in which the PAH^+, PAH^0, eVSG transition is spatially resolved and a simple geometrical model can be applied.
(a) van den Ancker *et al.* (1997) — (b) Racine (1968) — (c) Finkenzeller (1985) — (d) Witt *et al.* (2006) — (e) Alecian *et al.* (2008) — (f) Gerin *et al.* (1998) — (g) Diplas and Savage (1994) — (h) Fuente *et al.* (1995) — (l) Habart *et al.* (2003)

6.3 The physical conditions in the PDRs

The procedure presented above provides the total IR intensity emitted by each of the very small dust populations, PAHs and eVSGs. In order to study the variations of the eVSG abundance with the local radiation field, we need to quantify the relations between the mid-IR intensity, the abundance of the carriers and the radiation field.

For all the PDRs in Table 6.1, we assume an edge-on geometry and use a simple geometrical model to estimate the intensity of the radiation field at the PDR front. We then describe the profile of the radiation field intensity using PDR modelling along a star-PDR cut (see Fig. 6.9). For the PDRs selected in Table 6.2, such geometrical model is not appropriate and a mean value of the radiation field is taken from the literature.

6.3.1 Emissivity of AIB carriers

The power absorbed by the AIB carriers can be expressed as:

$$P_{abs} = \int_{91.2nm}^{\lambda_{max}} \left(n^C_{PAH} \sigma^C_{PAH}(\lambda) + n^C_{eVSG} \sigma^C_{eVSG}(\lambda) \right) F(\lambda) d\lambda \tag{6.2}$$

where $F(\lambda)$ is the radiation field flux, n^C_X is the number of C atoms per unit volume contained in grain type X (X=PAH, eVSG), and $\sigma^C_X(\lambda)$ represents the PAH or eVSG absorption cross-section per carbon atom. Since ionized PAHs and large neutral PAHs can absorb significantly in the visible (Salama *et al.*, 1996), we assume $\lambda_{max} = 1000nm$.

The absorbed energy is mainly reemitted in the mid-IR. Using the energy balance, the emitted power P_{em} equals the absorbed power P_{abs}. It is convenient to write P_{em} as proportional to the radiation field characterised by its value in Habing unit G_0 (1 Habing $= 1.6 \times 10^{-3}$ erg cm^{-2} s^{-1} between 91.2 and 240 nm, Habing, 1968). Thus we define the mean emission power of the AIB carriers per H atom and per Habing, or local emissivity, ϵ_{AIB} so that:

$$P_{em} = \epsilon_{AIB} \times n_H \times G_0 \tag{6.3}$$

where ϵ_{AIB} includes both the bands and the continuum emissions. Its value *a priori* depends on the hardness of the radiation field and the distribution of carbon atoms between PAHs and eVSGs.

If we assume that $\sigma^C_{PAH} = \sigma^C_{eVSG} = \sigma^C$, then conservation of energy implies that for the emission powers per carbon atom, one can write $\epsilon^C_{PAH} = \epsilon^C_{eVSG} = \epsilon^C_{AIB}$. Then, ϵ_{AIB} can be expressed as a function of the carbon contained in the AIB carriers:

$$\epsilon_{AIB} = \left(\frac{n^C_{PAH}}{n_H} + \frac{n^C_{eVSG}}{n_H} \right) \times \epsilon^C_{AIB} = \frac{n^C_{AIB}}{n_H} \times \epsilon^C_{AIB} \tag{6.4}$$

where n^C_X represents the number of C atoms per unit volume contained in PAHs or eVSGs.

Rapacioli *et al.* (2005) have shown that PAHs are produced by photo-destruction of eVSGs. We can consider, in first approximation, that all carbon contained in these

eVSGs is transferred into PAHs. Therefore, ϵ_{AIB} can be considered as independent of the relative abundance of PAHs and eVSGs:

$$\epsilon_{AIB} = \frac{n^C_{AIB}}{n_H} \times \frac{1}{G_0} \times \int_{91.2nm}^{1000nm} \sigma_C(\lambda) F(\lambda) d\lambda. \quad (6.5)$$

In order to estimate the variation of ϵ_{AIB} with the hardness of the radiation field we have calculated ϵ_{AIB} with the appropriate Kurucz spectra for the PDRs of Table 6.1. Our calculations show that, for the studied objects, ϵ_{AIB} marginally depends on the hardness of the radiation field.

To avoid deriving the absorption cross section σ^C from a specific PAH, we computed ϵ_{AIB} for a variety of PAHs of different sizes and charges from the on-line database of Malloci *et al.* (2007) [1]. The results scatter within 10%. Assuming a value of $n^C_{AIB}/n_H = 4.2 \times 10^{-5}$ (Draine, 2003, for $R_V = 5.5$) we obtain $\epsilon_{AIB} \sim 5 \times 10^{-32}$ W H^{-1} Habing^{-1}, consistent with previous estimates by Habart *et al.* (2001) and Habart *et al.* (2003).

6.3.2 Estimation of the impinging radiation field

To estimate the value of the impinging radiation field at the PDR front we used stellar spectra from Kurucz (1993) and applied a dilution factor based on the projected distance to the PDR front. In the case of NGC 2023 an extinction of $A_V = 1.1$ mag has been applied, reflecting the presence of absorbing dust around HD 37903 (Compiègne *et al.*, 2008). The calculated values of the radiation field are given in Habing units. They are consistent with previous estimates reported in Burton *et al.* (1998) and Habart *et al.* (2003) for NGC 2023 and ρ-Oph, respectively. The estimate of the radiation field intensity at the PDR front in NGC 7023 NW is more uncertain. (Chokshi *et al.*, 1988) estimated a $G_0 \sim 2.4 \times 10^3$ through far-IR observations and modelling, but values as high as $G_0 \sim 10^4$ have been proposed to explain the observed H_2 ortho-to-para ratio (Fuente *et al.*, 1999) towards this PDR. This latter value is in agreement with the value determined by assuming typical stellar properties for the corresponding spectral type of the illuminating binary star (Alecian *et al.*, 2008) and geometrical dilution to the PDR front. However, extinction between the star surface and the PDR may attenuate the radiation field, yielding a lower value at the PDR front. In this work, an extinction correction of $A_V = 1.5$ was derived from the IUE spectrum measured on the star and was applied on the corresponding Kurucz spectra. Assuming that the same extinction factor apply between the star and the PDR leads to an estimate for the NW PDR of $G_0 \sim 2.6 \times 10^3$ Habing, which is consistent with the value of (Chokshi *et al.*, 1988). All the parameters used to model the radiation field intensity are reported in Table 6.1.

6.3.3 Constraints on density and radiation field profile

The local radiation field inside the PDR depends on the impinging radiation field at the PDR surface and on the gas density profile that determines its attenuation. According to

[1] http://astrochemistry.ca.astro.it/database/

Eq. (6.3), the local mid-IR emissivity at each position is related to the same two physical parameters n_H and G_0. The total intensity can be obtained by integrating along the line of sight for each position z on the sky:

$$I_0(z) = \frac{1}{4\pi}\int_0^L G_0(r) \times n_H(r) \times \epsilon_{AIB}\, dl = K(z) \times \epsilon_{AIB} = K(z) \times \frac{n_{AIB}^C}{n_H}\epsilon_{AIB}^C \tag{6.6}$$

where r is the distance from the star and L is the thickness of the PDR perpendicular to the plane of the sky. We assume a spherical shell model as in Habart *et al.* (2003, their figure 6), in which the cloud is divided in successive layers of increasing density. The density gradient follows a power law $n_H \propto r^\alpha$ up to a maximum density determined by molecular observations (see references in table 6.1). Due to its attenuation by dust, the radiation field evolves as:

$$G_0(r) = G_0^{front} \times e^{-\sigma_{UV}\int_0^r n_H(r)dr} \tag{6.7}$$

in which σ_{UV} is the dust extinction cross-section at 1000 Å (1.5×10^{-21} cm^2 H^{-1}, Weingartner and Draine, 2001).

We used Eq. (6.6) to fit the spatial profiles of the corrected AIB emission derived as in Eq. (6.1). The free parameters of the fit are the density gradient (determined by the value of α), the position of the cutoff of the gradient, and the cloud physical length. This yields the density and radiation field profiles along each of the cuts. The parameters used for each of the selected PDRs are summarised in Table 6.1, and the modelled profiles are reported in Fig. 6.9.

6.4 Results

6.4.1 Mid-IR decomposition of PDRs

We applied the fitting procedure to all observed pixels in the PDRs listed in Table 6.1. This yields maps of the integrated intensity for each of the components included in the fit. As an example, Fig. 6.2 shows the obtained spatial decomposition for NGC 7023 NW. The spatial distributions of the PAH and eVSG components are coherent with the results of Rapacioli *et al.* (2005) and Berné *et al.* (2007), but as shown in Fig. 6.2, more information is retrieved with our approach such as the spatial distribution of gas lines and an estimate of the column density of the considered column of material.

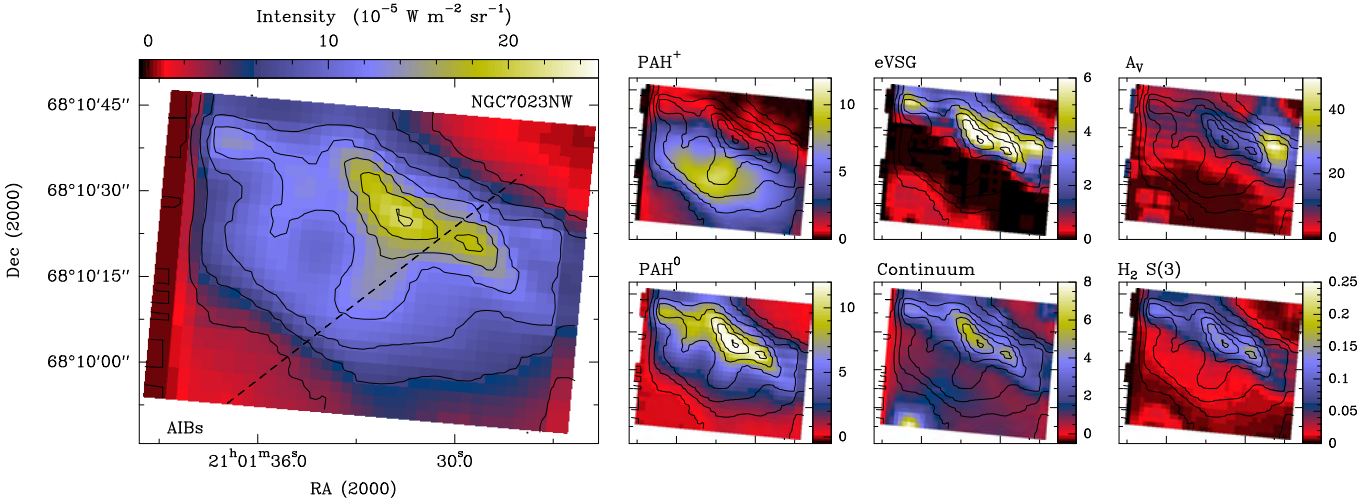

Figure 6.2: Results of the mid-IR decomposition for the NGC 7023 NW PDR, showing the integrated mid-IR intensity in the observed spectrum and in each of the template populations. The column density A_V is also shown, as well as the flux in the H_2 S(3) line. For reference, contours (in steps of 3×10^{-5} W m^2 sr^{-1}) of the total AIB flux in the 5.5-14 μm range are displayed. Similar plots for the other PDRs of Table 1 can be found in the appendix. The intensity scales are in units of 10^{-5} W m^2 sr^{-1}, while the column density is expressed in magnitude of visual extinction.

Figure 6.3 shows fits of the mid-IR spectrum for different objects, and the main results of the decomposition. The spectra show large variations in the relative intensities of the bands, reflecting variations of the local physical conditions. The fit results show indeed large variations in the relative weights of eVSG and PAH emissions. The PAH^x emission is significant (> 5%) only in highly-irradiated sources, coherently with the fact that these species are likely large ionised PAHs that can better resist in harsher environments and can reach there higher temperatures. The derived value of the column densities is high in the high-density filaments of NGC 7023 NW and NGC 2023 S (Fuente *et al.*, 1996; Joblin *et al.*, 2010; Fuente *et al.*, 1995).

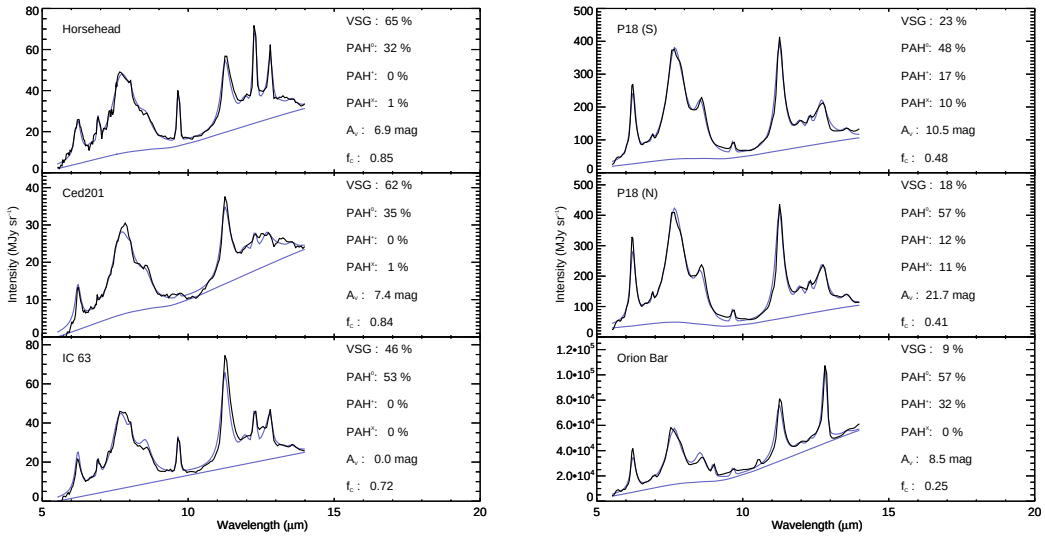

Figure 6.3: Mid-IR spectra (solid lines) and their fit (blue) for the PDRs listed in Table 6.2. For each spectrum, we report the resulting contributions for each of the PAH and eVSG populations to the mid-IR flux, the extinction along the line of sight and f_C, the fraction of carbon atoms locked in eVSGs relative to the total carbon in the AIB carriers.

6.4.2 Evolution of f_C along the PDRs

Equation (6.6) shows that, at each position z, the total IR emission due to PAHs and eVSGs is proportional to ϵ^C_{AIB}. A similar equation can be written for eVSGs only, using ϵ^C_{eVSG}:

$$I_{eVSG}(z) = K(z) \times \frac{n^C_{eVSG}}{n_H} \epsilon^C_{eVSG} \tag{6.8}$$

Combining Eqs. 6.6 and 6.8, and since $\epsilon^C_{AIB} = \epsilon^C_{eVSG}$, we can calculate for each z in the cut:

$$f_C(z) = \frac{I_{eVSG}(z)}{I(z)} = \frac{n^C_{eVSG}}{n^C_{AIB}} \tag{6.9}$$

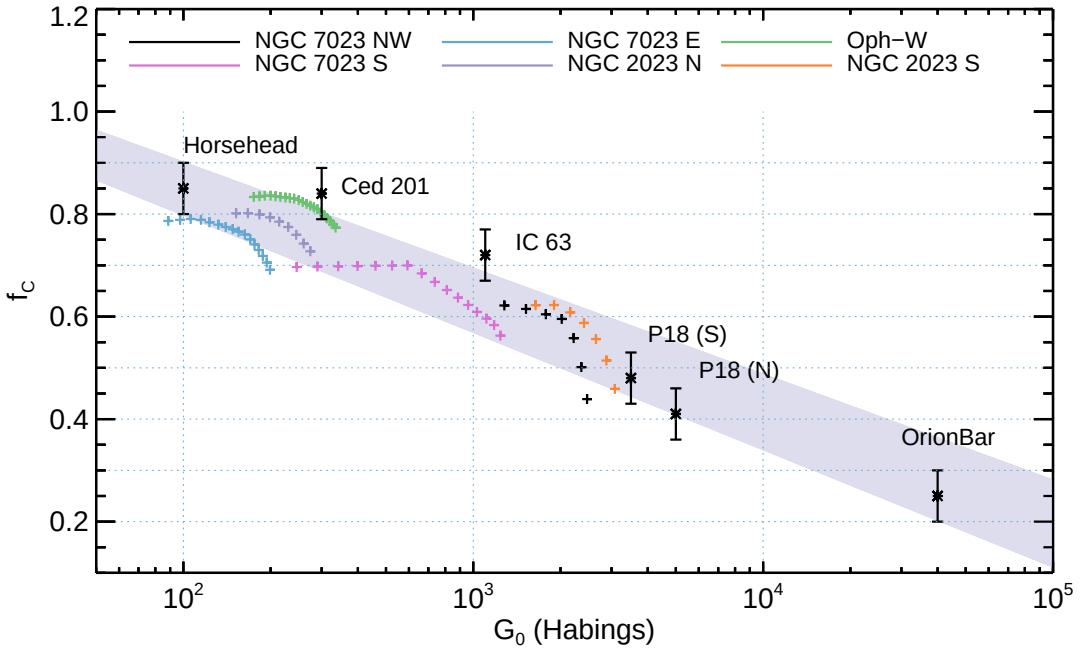

Figure 6.4: The fraction of carbon atoms locked in eVSGs relative to the total carbon in the AIB carriers as a function of the intensity of the local radiation field. Several points refer to each of the objects in Table 1, for which we determined the spatial variation of f_C and of the radiation field.

which represents the fraction of carbon atoms locked in eVSGs compared to all carbon atoms in the AIB carriers. The fit of the mid-IR spectra for PDRs is reliable in mild UV-irradiation conditions ($50 \lesssim G_0 \lesssim 5 \times 10^4$). At milder UV field intensities, f_C seems to stabilise at values of ~ 0.9, but in these regimes the mid-IR fits are less reliable because the AIB emission is fainter and sometimes barely detected. The extrapolation of the $G_0 - f_C$ relation to more intense UV fields is also difficult, since in these environments, the photo-processing of the eVSG and PAH populations is extreme leading in particular to the difficulty to observe the fragile eVSG species

6.4.3 Determination of the impinging radiation field from the eVSG abundances.

The lower panels in Fig. 6.9 show the profiles of f_C for each PDR in the sample. The procedure explained in Sect. 6.3.3 fails to reproduce the AIB profiles in the deepest parts of the PDRs, most likely because the presence of high density filaments (Fuente *et al.*, 1995, 1996) is not taken into account in the density profiles. We concentrate our analysis around the AIB peak, where the eVSG emission is a considerable part of the total AIB emission.

Figure 6.4 shows the values of f_C obtained for all the PDRs in our sample (Tables

6.1 and 6.2) as a function of the radiation field intensity G_0. For the resolved PDRs, the value of G_0 was derived at each position as explained in Sect. 6.3.3. For the unresolved PDRs, we applied the fitting procedure to the mean spectrum at a position for which a reliable estimate of the radiation field is found in the literature. Figure 6.4 shows a clear decrease of the fraction of carbon in eVSGs with the increase of the radiation field intensity. This trend can be fitted by the expression:

$$f_C = (-0.21 \pm 0.01) \log_{10}(G_0) + (1.29 \pm 0.03) \tag{6.10}$$

This relation can be inverted to estimate the radiation field intensity from the fit of the mid-IR spectrum, the value of f_C being a direct output of the fitting procedure.

To test the applicability of our method on unresolved objects, we applied the fitting procedure to the averaged spectra of larger fields of view (up to 1 arcmin) in our template object, NGC 7023 NW and derived a value for f_C. This value can be compared with the average value $< f_C >$ that can be calculated from the values obtained on all individual pixels contained in the same region. The agreement between the two values is very good for regions close to the eVSG peak. For regions close to the PDR front, the value of $< f_C >$ is higher by less than 0.05. This yields an overestimate of the mean radiation field by less than 40 %. Although this error is not directly transposable to other PDRs, it shows that the method can be used to derive an effective UV radiation field in unresolved objects with an uncertainty of a factor ~ 2.

As an example, we applied our fitting procedure to the IRS spectra of the nucleus and outflow of M82. The fit results are reported in Fig. 6.5. The derived column densities are high, especially in the nucleus region. The values of f_C derived from the mid-IR fit yield a radiation field of $G_0 = 5^{+5}_{-3} \times 10^3$ for the nucleus and $G_0 = 3^{+3}_{-2} \times 10^3$ for the outflow. Previous studies based on chemical modelling of the nucleus of M82 by Fuente *et al.* (2008) have predicted a $G_0 \sim 1 \times 10^4$, whereas previous modelling of far-IR observations (Colbert *et al.*, 1999; Kaufman *et al.*, 1999) report lower values ($10^{2.8} \lesssim G_0 \lesssim 10^{3.5}$). This is in reasonable agreement with our estimates.

6.5 Conclusion

In this chapter, we present an updated method to analyse the mid-IR spectra of PDRs with the use of a physically consistent set of template spectra. We have shown that such decomposition can be used as a tool to determine the fraction of C atoms in eVSGs. By combining the results with PDR modelling, we determined a relation between the relative carbon content in eVSGs compared to all AIB carriers and the UV radiation field intensity. This relation constitutes a useful tool to determine the mean UV radiation field in objects in which the eVSG population is quite abundant. The whole code will be made publicly available to the community as an IDL package, together with the template spectra used in this work. This procedure combined with the high spatial resolution and sensitivity of the forthcoming JWST mission will allow to determine the spatial variation of the UV radiation field in galaxies and distant objects.

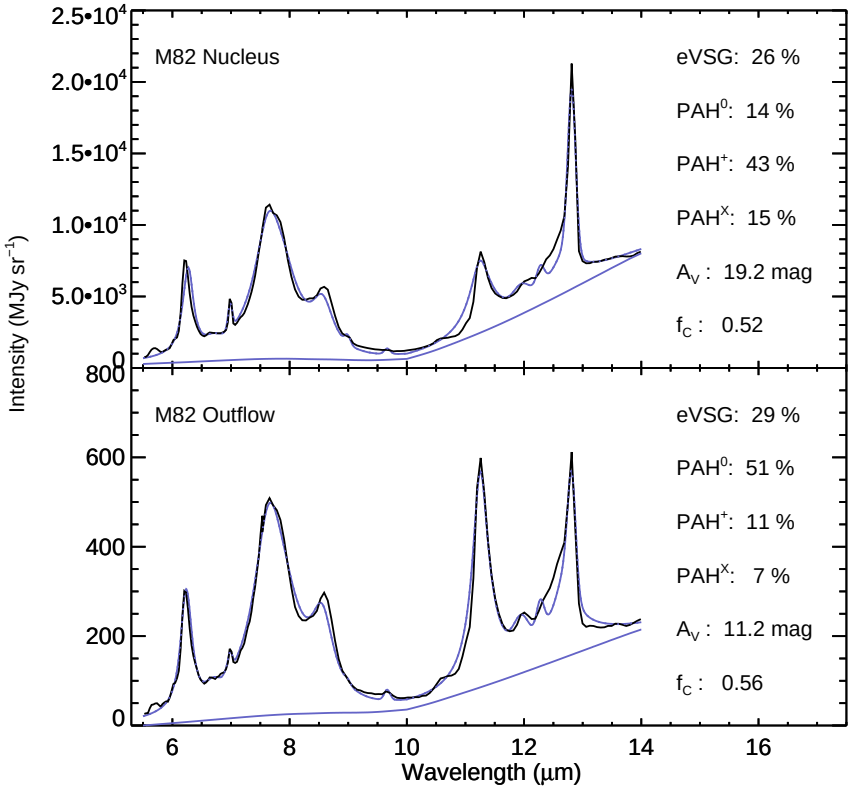

Figure 6.5: Mid-IR spectra (black line) of the nucleus and the outflow of M82 and their fits. The results of the fit suggest that the radiation field in the nucleus is slightly higher, as well as the column densities of the AIB emitters.

Object	Position $(\alpha_{2000}, \delta_{2000})$	Aperture	f_C^*	G_0^{**}	Ref.
Horsehead	(05:40:53; -02:28:00)	$9'' \times 7''$	0.85	100	Habart *et al.* (2005)
Ced 201	(22:13:25; 70:15:03)	$22'' \times 22''$	0.84	300	Young Owl *et al.* (2002)
IC 63	(00:59:01; 60:53:19)	$30'' \times 40''$	0.72	1100	Gerin *et al.* (2003)
Parsamyan 18 S	(06:59:41; -07:46:45)	$9'' \times 8''$	0.48	3500	Ryder *et al.* (1998)
Parsamyan 18 N	(06:59:41; -07:46:12)	$4'' \times 8''$	0.41	5000	Ryder *et al.* (1998)
Orion Bar	(05:35:21; -05:25:15)	$4'' \times 6''$	0.25	4×10^4	Tauber *et al.* (1994)

* This work
** Literature

Table 6.2: Fraction of carbon atoms in eVSGs and corresponding radiation fields for the PDRs used in this work. The correlation of these quantities is shown in fig. 6.4

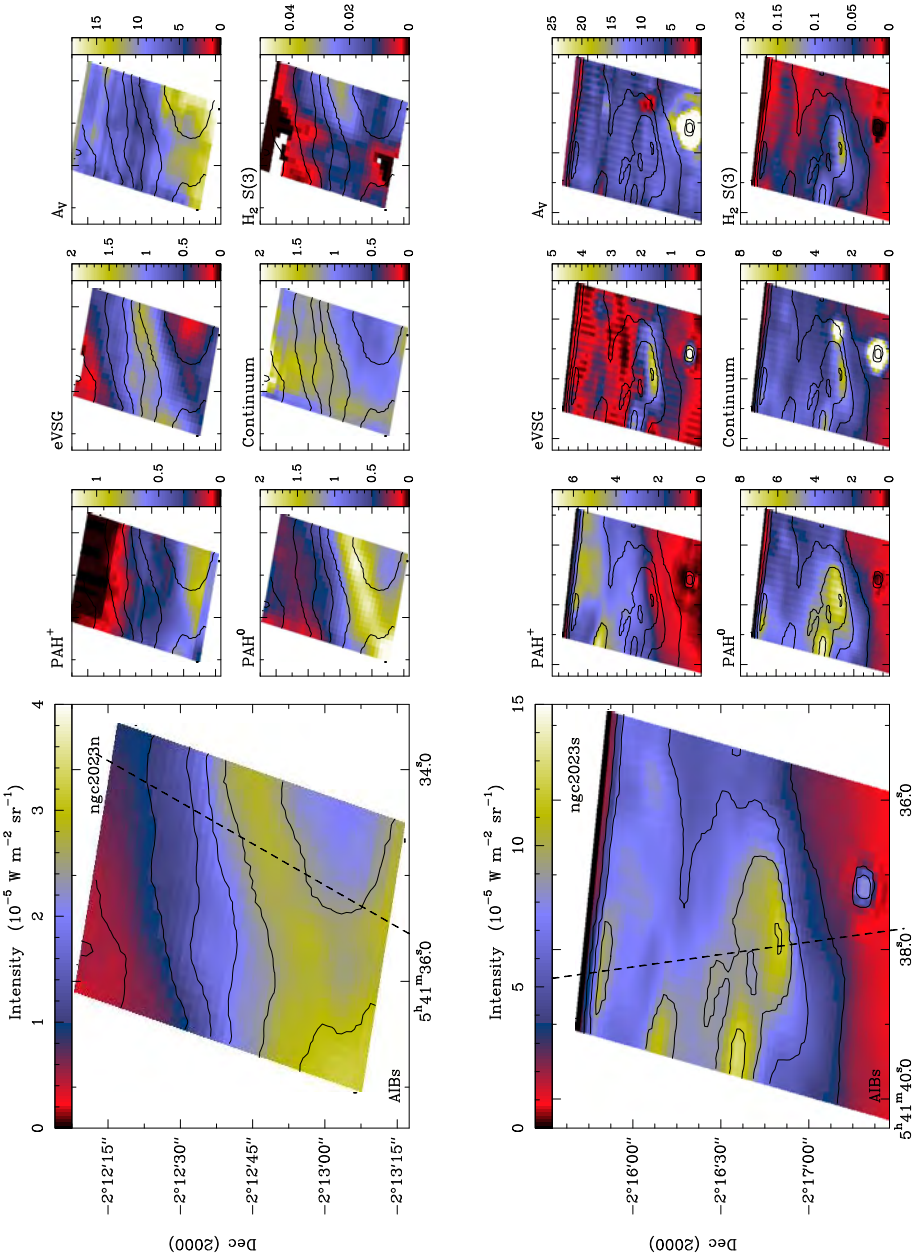

Figure 6.6: As Fig. 6.2, for NGC 2023 N and NGC 2023 S.

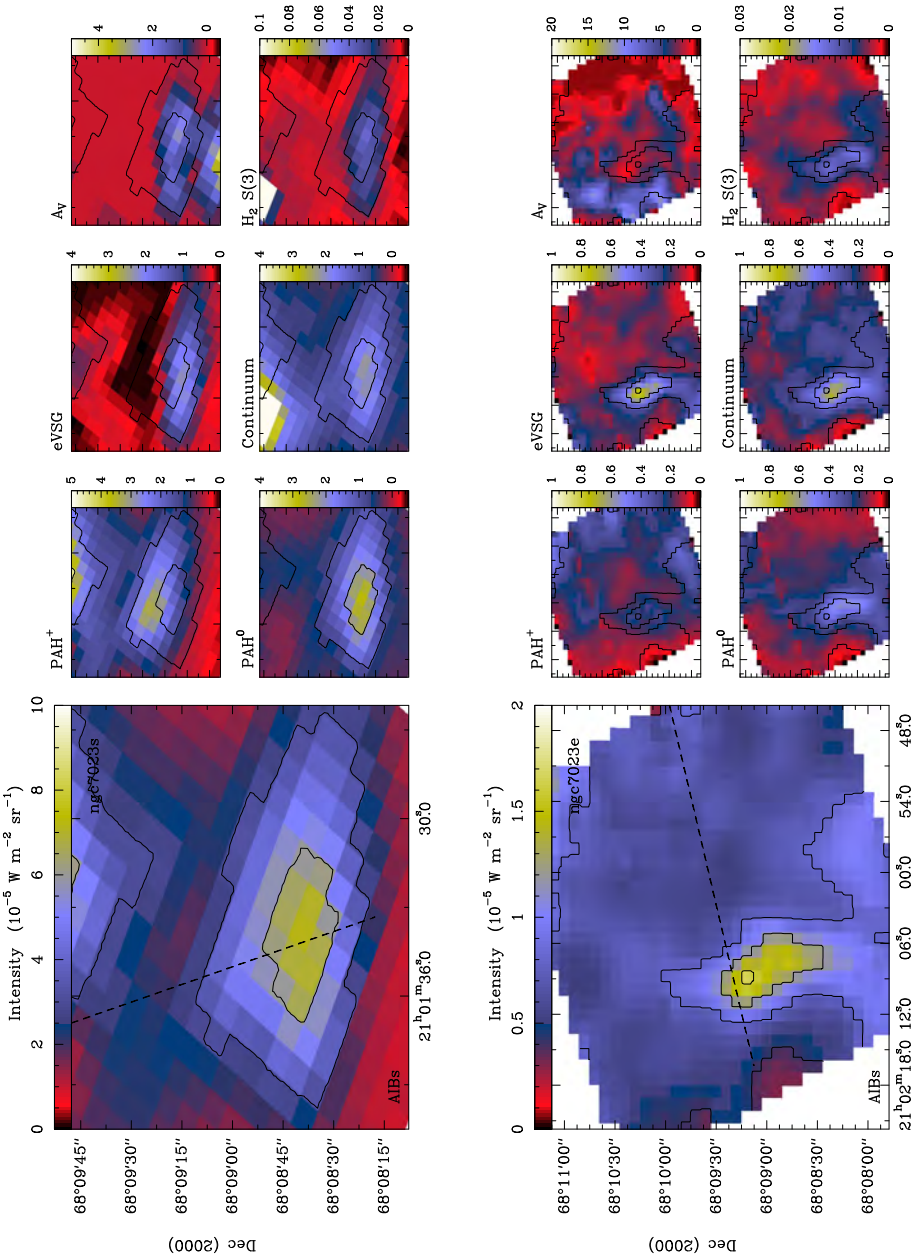

Figure 6.7: As Fig. 6.2 for NGC 7023 S and NGC 7023 E

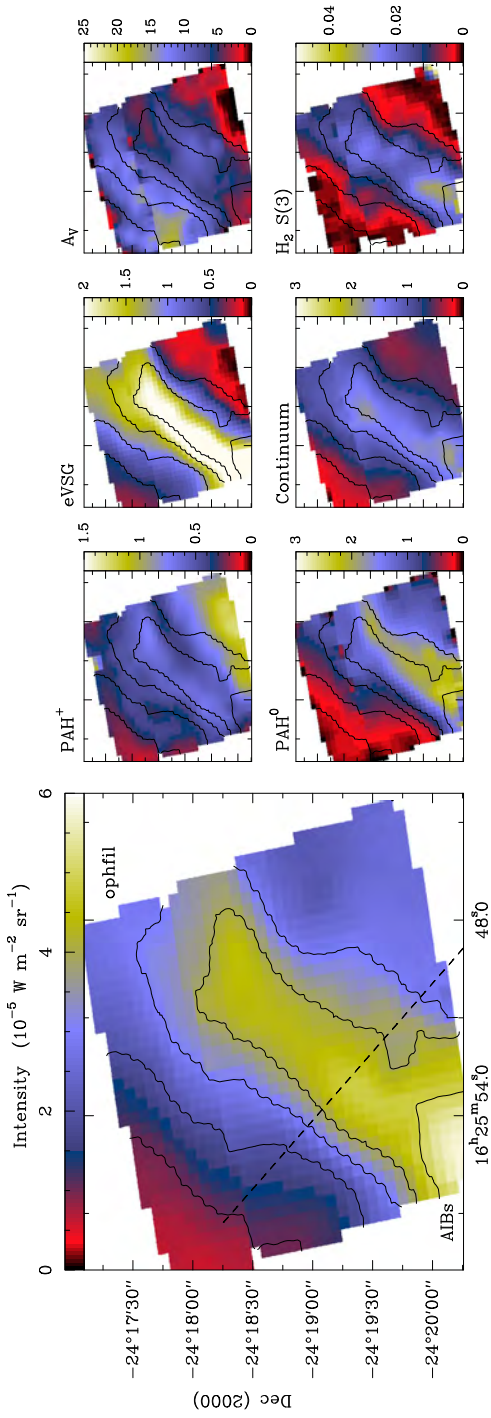

Figure 6.8: As Fig. 6.2 for the ρ-Ophiucus Filament.

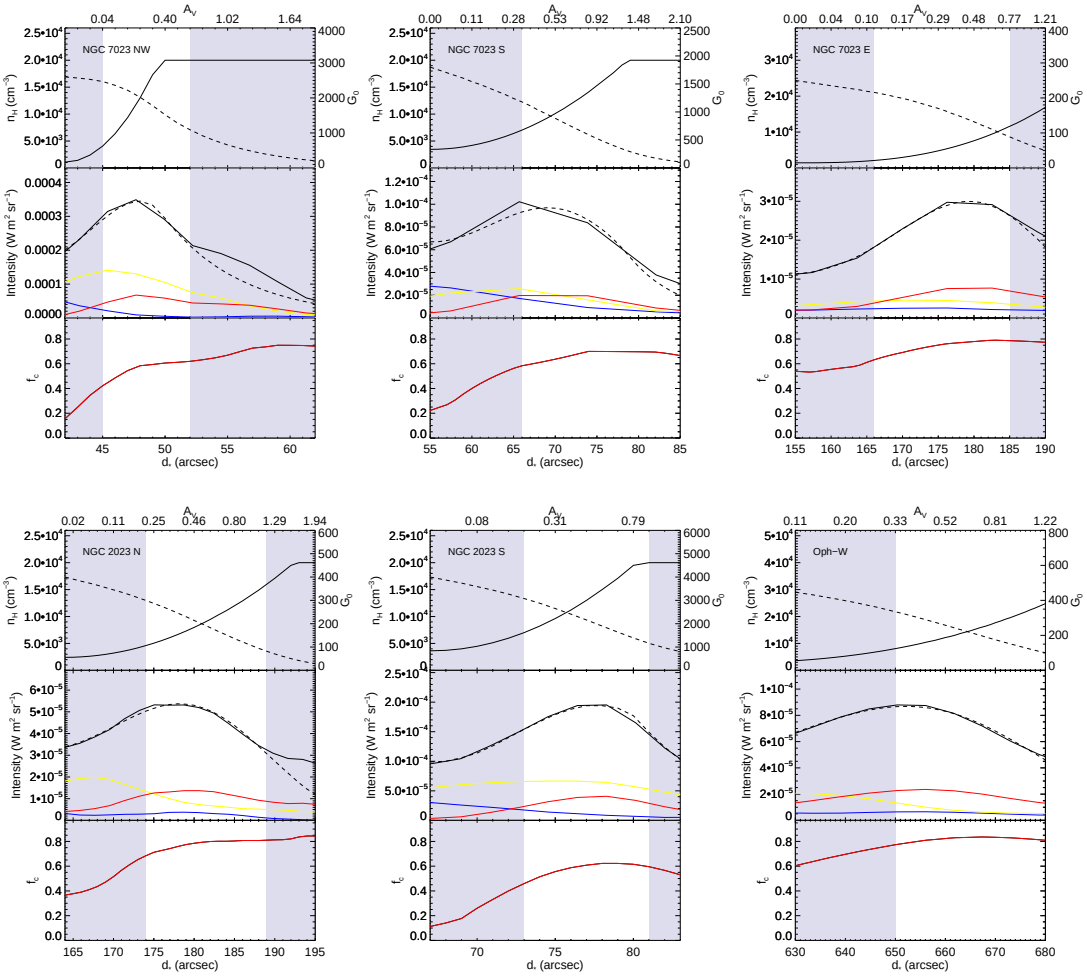

Figure 6.9: *Upper panels:* for each PDR cut, the density and radiation field profiles as a function of the distance from the star. *Central panels*: Blue, yellow and red represent the contribution of PAH^+, PAH^0 and eVSGs, as extracted from the fit. Solid black lines represent the corrected mid-IR emission profile after the continuum correction explained in 6.2. The dotted lines represent the fit obtained with the geometrical model described in Sect. 6.3.3 *Lower panels:* the variation in the fraction of carbon atoms locked in eVSGs relative to the total carbon in all the AIB carriers.

Chapter

7

Search for corannulene in the Red Rectangle[1]

7.1 INTRODUCTION

In the last 25 years, many efforts have been made towards the identification of a single PAH species. The Aromatic Infrared Bands in the mid-IR are not characteristic of individual species, and therefore cannot be used to identify specific PAHs. This is not the case of the ro-vibrational emission bands that arise in the far-IR at the end of the cooling cascade. These are associated to the whole carbon skeleton of the molecule, and are specific for each species (Mulas *et al.*, 2006). However, the far-IR and sub-mm domains cannot be easily observed from the ground, and a search for PAH bands in these domains is planned with *Herschel*. On the other hand, the pure rotational transitions of these molecules fall in the millimeter domain, and are readily accessible with ground-based radio telescopes.

Most common neutral PAHs present a very low (or zero) permanent dipole moment. Since the intensity of the rotational spectrum scales with the square of the dipole moment, the rotational emission for most PAHs is expected to be very weak. However,

[1]The work contained in this chapter has been published in Pilleri *et al.* (2009)

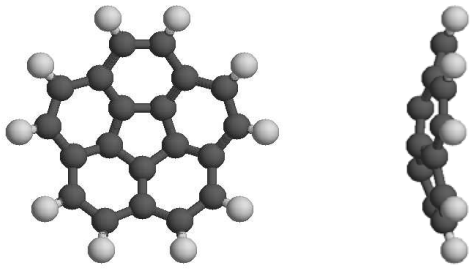

Figure 7.1: Structure of the corannulene molecule ($C_{20}H_{10}$). The central pentagonal carbon ring determines the bowl-shaped structure of the molecule, with a permanent dipole moment of 2.07 D along the symmetry axis.

Lovas *et al.* (2005) proposed the corannulene ($C_{20}H_{10}$) molecule as a good PAH candidate for radio identification since it has a large dipole moment (2.07 D, see Fig. 7.1). A first search for the low-J rotational transitions of corannulene in the molecular cloud TMC-1 was performed by Thaddeus (2006). However, since PAHs are expected to be free molecules only at the UV-irradiated surface of molecular clouds (Boulanger *et al.*, 1990; Rapacioli *et al.*, 2005; Berné *et al.*, 2007), the search for higher J rotational lines is more suited for an astronomical PAH (Rouan *et al.*, 1992).

There are several motivations for the search for corannulene in space. First, its detection would provide the first firm evidence for the presence of PAHs in space. Due to its curved structure, it is also representative of the transition between planar PAHs and fullerenes. The prototype fullerene molecule, C_{60}, has been proposed in its cationic form (C_{60}^+) to account for at least two DIBs in the near-IR (Foing and Ehrenfreund, 1994; Galazutdinov *et al.*, 2000), and has been observed in the reflection nebulae NGC 7023 and NGC 2023 by Sellgren *et al.* (2007, 2010) and in the proto-planetary nebula Tc-1 by Cami *et al.* (2010).

7.2 A SEARCH FOR CORANNULENE IN THE RED RECTANGLE

7.2.1 SPECTROSCOPY IN THE LABORATORY

Corannulene is a symmetric-top PAH with a bowl shaped structure (see Fig. 7.1). Whereas an ideal rigid rotor has a relatively simple rotational spectrum, centrifugal distortion can modify the separation of the energy levels and yield a complex rotational spectrum, composed by a large number of weaker lines. The search for corannulene in the mm domain requires a precise knowledge of the frequencies at which the rotational lines are expected to arise. This motivates experimental studies to quantify the rotational spectrum (rotational constants, stiffness of the molecule, ...).

These experimental studies have been performed by D. Herberth and T. Giesen at the Experimental Spectroscopy Group at the University of Cologne. They have detected a high J (J = 112 ← 111) rotational line of corannulene at 114.18 GHz (see Fig. 7.2) de-

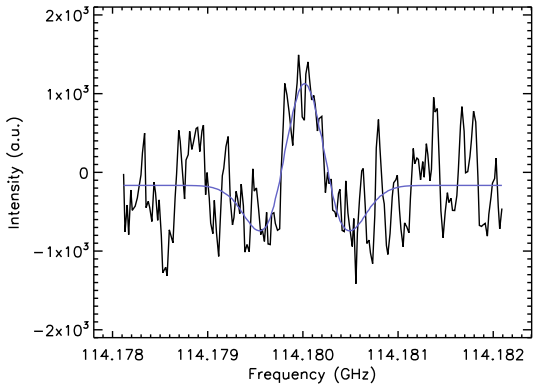

Figure 7.2: The line detection at 114.18 GHz measured in the laboratory with the OROTRON jet spectrometer, assigned to the J = 112 ← 111 transition of corannulene.

termining the rotational constants and evidencing that no centrifugal splitting is detected up to this transition. The stiffness of the molecule, and the high polarity of the molecule make corannulene an excellent candidate for astronomical detection in the mm domain.

7.2.2 Observations

The Red Rectangle

Using the rotational constants determined from the experiments, the frequencies of all the rotational transitions can be calculated assuming no centrifugal splitting. For the observations, the Red Rectangle (RR) nebula was chosen since it is the brightest source in the AIBs in the sky.

The Red Rectangle (RR) is a biconical C-rich nebula which surrounds a post-AGB binary system composed of the primary star HD 44179 (spectral type A0) and its luminous giant companion. It has been observed in the mid-IR with the SWS instrument onboard ISO and with the IRS instrument onboard *Spitzer*. The dimensions on the plane of the sky of the infrared bipolar nebula at 11.3 μm are about 10" x 15" (Waters *et al.*, 1998, see Fig. 7.3). A warm, high density disk ($n_H > 3 \times 10^4\,\mathrm{cm}^{-3}$, 30 K < T < 400 K) traced by CO emission (Bujarrabal *et al.*, 2005) surrounds the binary star with a thickness of roughly 3" along the symmetry axis.

Observations at the IRAM 30m telescope

We obtained 22 hours of observing time at the the IRAM 30m telescope in Pico Veleta. I was involved in the observations in February 2008. The observational parameters are reported in Table 7.1 for each of the observed frequency range. Weather conditions were acceptable for most of the time. The observed frequency ranges cover several high-J transitions of $C_{20}H_{10}$ at 1, 2 and 3 mm. Since the PAH emission pattern of this source is

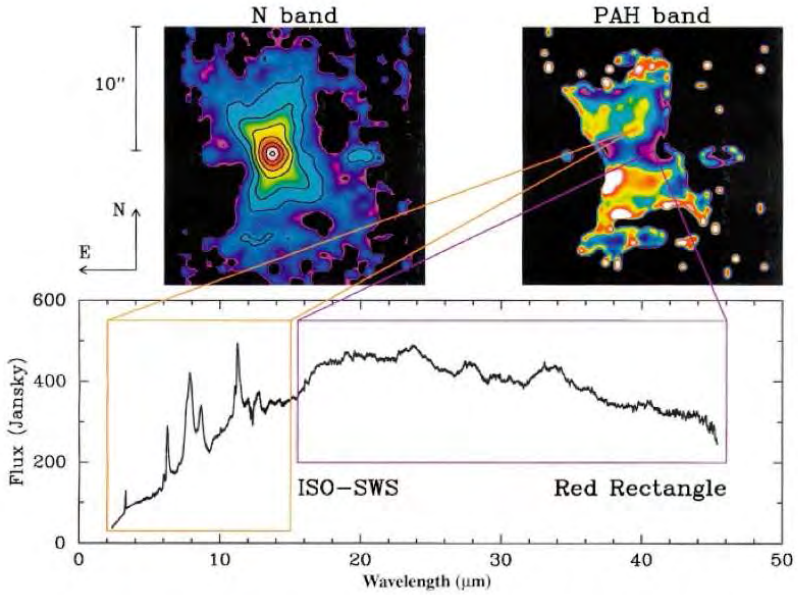

Figure 7.3: Spatial distribution of the dust component (N-band) and PAHs (continuum-subtracted 11.3 μm band) of the Red Rectangle. The figure shows that the PAH emission arises from a region of about 10″ ×15″. *Source: Waters* et al. *(1998)*

rather compact (the 11.3 μm intensity decreases by a factor of 10 in 20″), the wobbling secondary observing mode is appropriate using a separation of ±100" in azimuth. This observing mode ensures stable and flat baselines and is well adapted to compact sources such as the Red Rectangle.

Pointing was made on the central binary star HD 44179 (α_{2000}: 06:19:58.216, δ_{2000}: -10:38:14:691). Mars and Orion (α_{2000}: 05:35:14.5, δ_{2000}: -05:22:30.00) were used as reference sources for calibration and pointing. Pointing was accurate within 3" during all observations.

The flexibility of the four receivers and of the VESPA correlator allowed to cover several frequency ranges within one configuration, with a spectral resolution of 40 kHz and a total band pass of at least 40 MHz. We also used the 1 MHz resolution filterbanks to obtain broadband spectra (250 MHz) with lower spectral resolution. During all observations, one of the backends was dedicated to the ^{13}CO (1-0), (2-1), or ^{12}CO(2-1) transition, to check whether the telescope was pointed on source, and to monitor the calibration accuracy. The observed ^{12}CO intensity and line width are in good agreement with previous observations of the Red Rectangle with the IRAM 30 m telescope reported by Jura *et al.* (1995). The summary of the ^{12}CO and ^{13}CO observations is given in Table 7.2.

Data reduction and results

To improve the quality of the observed spectra, we manually cut isolated spikes at 4σ level and discarded observations with anomalous system temperature or with a high sky opacity. Different observations of the same transitions were averaged, and the antenna temperature was scaled with the telescope main beam efficiency η_{mb} by the relation $T_{mb} = T_A^*/\eta_{mb}$, where $\eta_{mb} = F_{eff}/B_{eff}$. The expected flux derived from the synthetic spectrum and the 3σ detection limit corrected for beam dilution for the corannulene observations are reported in Table 7.1. The rms level was calculated after smoothing the spectra to the velocity resolution of 0.4 km s^{-1}. We show in Fig. 7.4 the observed spectra in the regions where the 135 → 134 and 86 → 85 transitions of $C_{20}H_{10}$ are expected, and the ^{12}CO and ^{13}CO observations. We did not detect any corannulene line at any frequency. The best rms level for corannulene has been obtained for the transitions J+1 → J = 135 → 134, 84→ 83 and 86→ 85.

Transition (J+1 → J)	Frequency (GHz)	Beam size (")	B_{eff}	T_{sys} (K)	σ_{mb} (mK)	Bandwidth (MHz)	$F_{3\sigma}$ (10^{-25} W cm^{-2})	F_{model} (10^{-21} W cm^{-2})
84 → 83	85.643	29	0.78	117	10	80	1.4	5.7
86 → 85	87.682	28	0.77	107	12	80	1.7	6.2
108 → 107	110.104	22	0.75	170	14	80	1.6	13
111 → 110	113.316	22	0.74	276	21	120	2.3	14
135 → 134	137.615	17	0.70	219	8	80	0.9	19
215 → 214	219.059	11	0.55	346	45	80	5.4	5.3
216 → 215	220.076	11	0.54	328	20	80	2.4	5.2
223 → 222	227.197	11	0.53	269	23	80	2.9	4.0
226 → 225	230.248	11	0.52	389	30	80	3.8	3.7
238 → 237	242.450	10	0.50	525	22	80	2.8	2.3
257 → 256	261.763	8	0.46	546	39	40	5.4	0.9

Table 7.1: Summary of the observations towards the RR in different frequency ranges, corresponding to the expected rotational transitions of corannulene. On average, the 3 mm observations have a lower rms, but suffer more from beam dilution effects compared to the 1 mm observations.

Transition (J+1 → J)	Frequency (GHz)	Beam size (")	B_{eff}	T_{sys} (K)	Area (K km s^{-1})	Bandwidth (MHz)
^{12}CO (2 → 1)	230.538	10	0.52	486	6.8	40
^{13}CO (1 → 0)	110.201	22	0.75	159	0.3	40
^{13}CO (2 → 1)	220.398	11	0.55	339	1.7	40

Table 7.2: Summary of ^{12}CO and ^{13}CO observations towards the Red Rectangle.

7.3 An upper limit to the abundance of Corannulene

7.3.1 Modelling

The interpretation of the observational upper limits of the line intensities in terms of abundances of corannulene needs an a-priori knowledge of the intensity of its rotational spectrum in the Red Rectangle environment. This requires detailed modelling of the photo-physical processes that drive to the emission of rotational lines (cf. Sect. 2.3.2). The modelling was performed by the Astro-CHemistry group of the University of Cagliari (Italy) by G. Mulas and G. Malloci, using a well-established theoretical model (Mulas, 1998; Mulas *et al.*, 2006). The model needs as input the UV-visible absorption cross-section, the vibrational modes and their Einstein A coefficients, the rotational constants and the dipole moment of the molecules, which are obtained either by laboratory measurements (cf. Sect. 7.2.1) or by state-of-the-art quantum chemical calculations (Malloci *et al.*, 2004). The modelling was performed for a single corannulene molecule in the specific radiation field of the Red Rectangle.

7.3.2 Comparison of observations and modelling

To calculate an upper limit to the abundance of corannulene in the source, we assumed a 3σ detection limit and a gaussian profile with a FWHM of $1\,\mathrm{km\,s^{-1}}$. Before comparing the observed rms to the model, we have to take into account the effect of beam dilution. As a first approximation, we assume that PAH emission is distributed homogeneously in a $10'' \times 15''$ area as observed for AIB emission (Waters *et al.*, 1998).

The best noise levels are reached, on average, with the 3 mm observations, but the 1 and 2 mm observations suffer less from beam dilution. To compute a reliable upper limit to the abundance of corannulene, we chose the $135 \rightarrow 134$ transition at 2 mm, which is not only the transition with the lowest rms, but also the best compromise between the loss of flux due to beam dilution and expected intensity derived from the synthetic spectrum.

The ratio between observations and theoretical predictions can be turned into an upper limit for the fraction of AIB flux due to corannulene, which corresponds to the fractional abundance of carbon locked up into corannulene relative to the total abundance of carbon in PAHs. For this, we have scaled the mid-IR part of the synthetic spectrum to the total AIB intensity measured in the Red Rectangle. This led to an integrated flux of $F_{model} = 1.9 \times 10^{-20}\,\mathrm{W\,cm^{-2}}$ in the $135 \rightarrow 134$ line. We compare this value with the area of the 3σ gaussian for the same transition, corrected for beam dilution: $\mathrm{F}_{3\sigma} = 9.0 \times 10^{-26}\,\mathrm{Wcm^{-2}}$.

Comparing this upper limit with the results from modelling, we derive a value of 1.0×10^{-5} as our best limit for the fraction of carbon in $C_{20}H_{10}$ relative to the total carbon in all PAHs. Assuming that $\sim$ 20% of total carbon atoms are locked in PAHs (Joblin *et al.*, 1992), this turns into a value of 2.0×10^{-6} of total carbon in corannulene. This

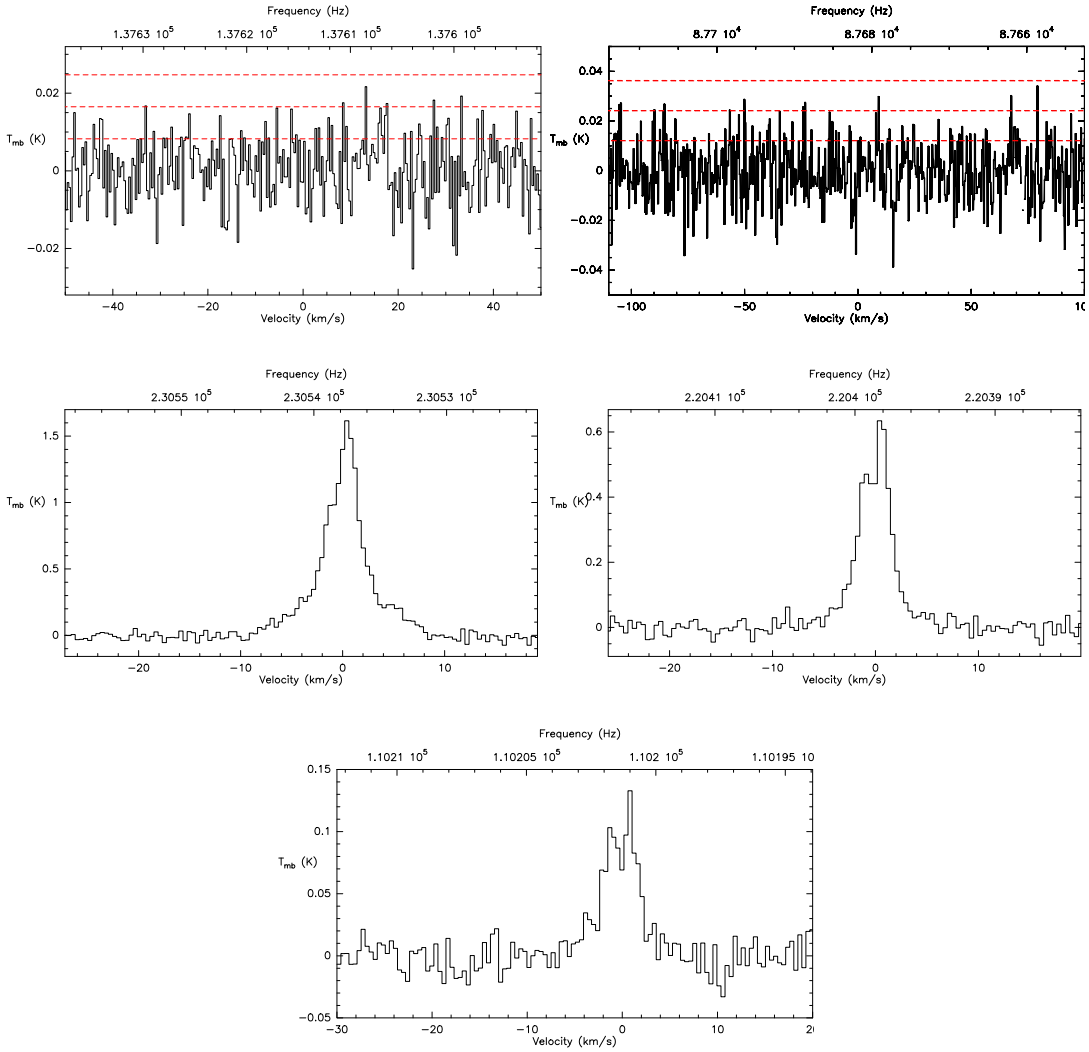

Figure 7.4: Observations of the expected frequency range for the 135 → 134 transition at 137 GHz, the 86 → 85 transition at 88 GHz of $C_{20}H_{10}$, the ^{12}CO(1-0) and ^{13}CO(1-0),(2-1) transitions. Horizontal red lines indicate the 1σ, 2σ and 3σ levels.

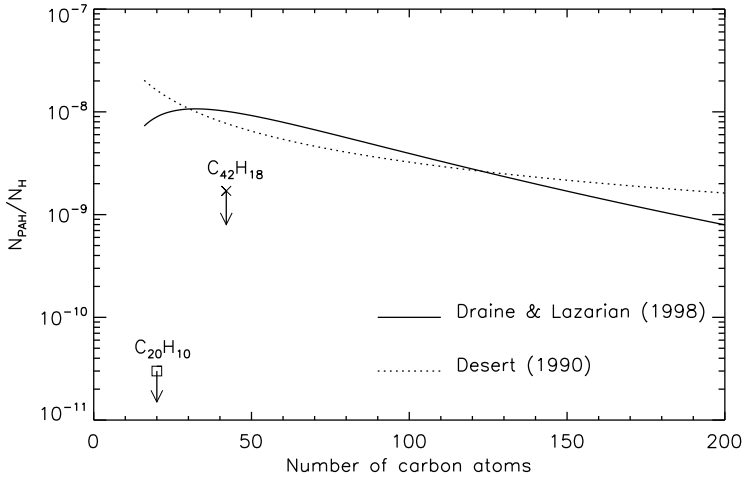

Figure 7.5: Size distributions of PAHs according to Désert *et al.* (1990) and Draine and Lazarian (1998), normalised to a carbon abundance in PAHs of 6×10^{-5} relative to hydrogen (Joblin *et al.*, 1992; Draine and Lazarian, 1998). The two upper limits reported refer to the observations of corannulene in the RR (this work) and of $C_{42}H_{18}$ in the diffuse interstellar medium (Kokkin *et al.*, 2008). The discrepancy between models and observations supports the underabundance of small PAHs in space.

result is much more stringent than the limit derived by Thaddeus (2006) for corannulene in TMC-1, 1×10^{-5}.

7.4 Conclusions

Experimental studies (Lafleur *et al.*, 1993) indicate that corannulene is not a peculiar PAH and is indeed observed as a sizable fraction of small PAHs produced by pyrolysis of hydrocarbons that is commonly considered to be the formation mechanism of PAHs in C–rich outflows (Frenklach and Feigelson, 1989; Cherchneff *et al.*, 1992; Cernicharo *et al.*, 2001). Corannulene can be considered as a good tracer of the small PAH population. Using the experimental results of Lafleur *et al.* (1993), it is possible to translate the upper limit of corannulene in an upper limit of the C atoms contained in small PAHs. This yields to an upper limit of ∼2% for the mass fraction of small PAHs containing less than 50 C atoms with respect to the total mass in PAHs. Current models for interstellar PAHs use a size distribution with about 20% of the mass in small PAHs (Draine and Lazarian, 1998, cf. Fig. 7.5). There is therefore a difference of one order of magnitude between the observations and the models.

This discrepancy can be interpreted in terms of the photo-destruction and production processes of small PAHs in the environment of the Red Rectangle. The photodissociation rate of corannulene in the Red Rectangle was calculated using a Monte-

Carlo model and experimental results from the PIRENEA setup (Joblin et al., in preparation). Comparing this dissociation rate with the recombination rate with hydrogen atoms, we determined that corannulene is expected to survive in its neutral hydrogenated form in the Red Rectangle. Therefore, the observed underabundance of small PAHs is most likely related to the production mechanism of small PAHs in C-rich outflows.

Mon. Not. R. Astron. Soc. (2009) doi:10.1111/j.1365-2966.2009.15067.x

Search for corannulene ($C_{20}H_{10}$) in the Red Rectangle

P. Pilleri,[1,2]⋆ D. Herberth,[3] T. F. Giesen,[3] M. Gerin,[4] C. Joblin,[1,2] G. Mulas,[5] G. Malloci,[5] J.-U. Grabow,[6] S. Brünken,[7] L. Surin,[3] B. D. Steinberg,[8] K. R. Curtis[8] and L. T. Scott[8]

[1]*Université de Toulouse; UPS; CESR; 9 avenue du colonel Roche, F-31028 Toulouse cedex 9, France*
[2]*CNRS; UMR5187; F-31028 Toulouse, France*
[3]*I. Physikalisches Institut, Universität zu Köln, Zülpicher Str. 77, 50937 Köln*
[4]*LERMA-LRA, CNRS-UMR8112, Observatoire de Paris et École Normale Supérieure, 24 rue Lhomond, 75231 Paris Cedex 05, France*
[5]*INAF Osservatorio Astronomico di Cagliari, Astrochemistry Group, Strada n.54, Loc. Poggio dei Pini, 09012 Capoterra (CA), Italy*
[6]*Gottfried-Willhelm-Leibniz-Universität, Institut für Physikalische Chemie & Elektrochemie, Lehrgebiet A, Callinstraße 3A, D-30167 Hannover, Germany*
[7]*Laboratoire de Chimie Physique Moléculaire (LCPM), École Polytechnique Fédérale de Lausanne (EPFL), Station 6, CH-1015 Lausanne, Switzerland*
[8]*Merkert Chemistry Center, Boston College, Chestnut Hill, MA 02467-3860, USA*

Accepted 2009 May 6. Received 2009 May 4; in original form 2009 April 2

ABSTRACT

Polycyclic Aromatic Hydrocarbons (PAHs) are widely accepted as the carriers of the Aromatic Infrared Bands (AIBs), but an unambiguous identification of any specific interstellar PAH is still missing. For polar PAHs, pure rotational transitions can be used as spectral fingerprints for identification. Combining dedicated experiments, detailed simulations and observations, we explore d the mm wavelength domain to search for specific rotational transitions of corannulene ($C_{20}H_{10}$). We performed high-resolution spectroscopic measurements and a simulation of the emission spectrum of ultraviolet-excited $C_{20}H_{10}$ in the environment of the Red Rectangle (RR), calculating its synthetic rotational spectrum. Based on these results, we conducted a first observational campaign at the IRAM 30-m telescope towards this source to search for several high-J rotational transitions of $C_{20}H_{10}$. The laboratory detection of the J = 112 ← 111 transition of corannulene showed that no centrifugal splitting is present up to this line. Observations with the IRAM 30-m telescope towards the RR do not show any corannulene emission at any of the observed frequencies, down to a rms noise level of $T_{\rm mb} = 8$ mK for the J =135 → 134 transition at 137.615 GHz. Comparing the noise level with the synthetic spectrum, we are able to estimate an upper limit to the fraction of carbon locked in corannulene of about 1.0×10^{-5} relative to the total abundance of carbon in PAHs. The sensitivity achieved in this work shows that radio spectroscopy can be a powerful tool to search for polar PAHs. We compare this upper limit with models for the PAH size distribution, emphasizing that small PAHs are much less abundant than predicted. We show that this cannot be explained by destruction but is more likely related to the chemistry of their formation in the environment of the RR.

Key words: astrochemistry – ISM: abundances – ISM: individual: Red Rectangle – ISM: lines and bands – ISM: molecules.

1 INTRODUCTION

Polycyclic Aromatic Hydrocarbons (PAHs) have been proposed more than 20 yr ago as an important constituent of the interstellar medium (ISM) (Léger & Puget 1984; Allamandola, Tielens & Barker 1985), being the most likely carriers of the Aromatic Infrared Bands (AIBs), the mid-IR emission features at 3.3, 6.2, 7.7, 8.6, 11.3 and 12.7 μm that dominate the spectra of many interstellar ultraviolet (UV)-excited dusty environments (Allamandola, Tielens & Barker 1989; Léger, d'Hendecourt & Defourneau 1989). PAHs are also thought to be responsible for some of the Diffuse Interstellar Bands (DIBs), more than 300 unidentified absorption features in the UV-visible range observed in the spectra of reddened stars (Léger & d'Hendecourt 1985; van der Zwet & Allamandola 1985). Finally, PAHs are nowadays a crucial ingredient in all models of interstellar extinction by dust, playing the role of the 'Platt particles' (Platt 1956; Donn 1968) in contributing to the bump at

⋆E-mail: paolo.pilleri@cesr.fr

Figure 1. Structure of the corannulene molecule ($C_{20}H_{10}$). The central pentagonal carbon ring determines the bowl-shaped structure of the molecule, with a permanent dipole moment of 2.07 D along the symmetry axis.

220 nm and producing the far-UV rise in the extinction curve (Li & Draine 2001; Cecchi-Pestellini et al. 2008). This has motivated much experimental and theoretical work, but still an unambiguous identification of a single species is missing. This task faces the difficulty that bands in the region of the AIBs, which are associated with vibrations of aromatic C–C and C–H bonds, are common to the whole class of PAHs. It is therefore difficult to use these IR bands to identify single species, even though their study led many authors to obtain information on the nature of their carriers (see e.g. Pech, Joblin & Boissel 2002; Peeters et al. 2002; Berné et al. 2007; Joblin et al. 2008). Vijh, Witt & Gordon (2004, 2005) proposed a tentative identification of neutral pyrene ($C_{16}H_{10}$) and anthracene ($C_{14}H_{10}$) towards the Red Rectangle (RR) nebula but this identification was challenged by Mulas et al. (2006c). Recently, Iglesias-Groth et al. (2008) claimed a tentative identification of ionized naphthalene ($C_{10}H_8^+$) by the correspondence of three bands from its electronic spectrum with three observed DIBs.

Mulas et al. (2006b) showed that, in principle, it is possible to identify specific interstellar PAHs by the detection of the ro-vibrational emission bands that arise in the far-IR during the cooling cascade following UV excitation. The observation of these bands in the far-IR domain however requires airborne and satellite instruments due to strong atmospheric absorption, and will be one of the goals of the Herschel Space Observatory (HSO).[1] On the other hand, the rotational transitions of these molecules fall in the mm domain, and are readily accessible with ground-based radio telescopes.

In a PAH, the absorption of a UV photon generally leads to fast internal conversion of its energy into vibrational energy of the electronic ground state. This energy is then released by ro-vibrational emission in the mid-IR and far-IR range s (cf. e.g. models by Joblin et al. 2002; Mulas et al. 2006a). The intensity of the rotational spectrum scales with the square of the dipole moment but, unfortunately, most common neutral PAHs present very low (or zero) permanent dipole moments. Still there are a few exceptions (Lovas et al. 2005; Thorwirth et al. 2007), and Lovas et al. (2005) proposed that a good PAH candidate for radio identification is corannulene ($C_{20}H_{10}$), which has a large dipole moment of 2.07 D (see Fig. 1). Thaddeus (2006) conducted a first search for corannulene in the molecular cloud TMC-1 searching for the low-J transitions reported in Lovas et al. (2005). One difficulty with such observational strategy is that free PAHs are expected to be present at the surface of molecular clouds (Boulanger et al. 1990; Rapacioli, Joblin & Boissel 2005; Berné et al. 2007). In these regions, the molecules are excited by UV photons and their rotational spectrum will differ from that of cold molecules excited by collisions (Rouan et al. 1992).

[1] http://herschel.esac.esa.int/

There are several motivations to put further effort into the search for corannulene in space. It is a member of the PAH population and its detection would provide the first firm evidence for the presence of such species in space.

Experimental studies (Lafleur et al. 1993) indicate that corannulene is not a peculiar PAH and that it should not be classified as an unlikely component in natural mixtures. It is indeed expected to constitute a sizeable fraction of a mixture of small PAHs produced by pyrolysis of hydrocarbons which is commonly considered to be the formation pathway of PAHs in C–rich outflows (Frenklach & Feigelson 1989; Cherchneff, Barker & Tielens 1992; Cernicharo et al. 2001). In short, corannulene should be a good tracer of the small PAH population.

Furthermore, with its bowl-shaped geometry, it is also representative of the transition between planar PAHs and curved fullerenes, and several authors have proposed chemical pathways for the formation of C_{60} involving corannulene (Haymet 1986; Kroto 1988; Chang et al. 1992). The prototype fullerene molecule, C_{60}, has been proposed in its cationic form (C_{60}^+) to account for at least two DIBs in the near-IR (Foing & Ehrenfreund 1994; Galazutdinov et al. 2000).

In this paper, we discuss the concerted efforts between modelling and laboratory work that led us to perform a first observational campaign to search for corannulene in UV-irradiated environments. The RR nebula was chosen since it is the brightest source in the AIBs in the sky and because it exhibits emission features at nearly the same wavelengths as some DIBs (Schmidt, Cohen & Margon 1980; Scarrott et al. 1992; Sarre, Miles & Scarrott 1995; Van Winckel, Cohen & Gull 2002), making it a good source for validating the PAH model. Modelling and laboratory work are described in Sections 2 and 3. Observations and data reduction are presented in Section 4, and discussion is provided in Section 5.

2 MODELLING

The emission model for a generic interstellar PAH molecule described in Mulas (1998) has been extended and applied to individual PAHs in Mulas et al. (2006a), where the far-IR spectra for a large sample of PAH species were presented. This model is applied here to calculate the rotational emission spectrum of a $C_{20}H_{10}$ molecule in the radiation field of the RR halo, as defined in Mulas et al. (2006c), that is the region of the RR nebula which is out of the bipolar cone and out of the dust torus surrounding the central binary system. The model input parameters are the UV-visible absorption cross-section, the vibrational modes and their Einstein A coefficients, the rotational constants and the dipole moment. The rotational constants were taken from Lovas et al. (2005), while the absorption cross-section, the frequencies and the A coefficients of the IR active modes were obtained by state-of-the-art quantum-mechanical calculations (available in the PAH spectral data base http://astrochemistry.ca.astro.it/database, Malloci, Joblin & Mulas 2007). For all other relevant molecular parameters, we used the same assumptions as in Mulas et al. (2006c).

Since calculations are for a single $C_{20}H_{10}$ molecule, the synthetic spectrum is then scaled in the following way to allow the comparison with the observations.

(i) Any PAH (including corannulene, if present) absorbs energy in the UV proportionally to its UV absorption cross-section, which scales with the number of carbon atoms in the molecule (Joblin, Léger & Martin 1992).

(ii) After the absorption of a UV photon, most of this energy is re-emitted in the AIBs. We integrated the AIB flux between 3 and

15 μm measured with the Short Wavelength Spectrograph (SWS) onboard the *Infrared Space Observatory (ISO)* (Waters et al. 1998) to estimate the energy absorbed by all PAHs in the nebula.

(iii) We calculated the expected integrated flux emitted by a single corannulene molecule between 3 and 15 μm, and derived the normalization factor to the flux measured by SWS.

(iv) We applied the same normalization factor to the whole spectrum, including the rotational transitions.

The Einstein A coefficients for spontaneous emission in the IR bands are typically between 10^{-2} and 10^{2} s^{-1}. In case of pure rotational transitions, typical A values are of the order of 10^{-5}–10^{-7} s^{-1}. Therefore, the IR and rotational emissions are expected to occur at different time-scales. However, the IR cascade can bring the molecule in to a vibrationally excited (metastable) state, where only IR inactive modes are populated. The molecule can therefore spend a non-negligible amount of time in states like this, since their main relaxation channel is via a forbidden vibrational transition. With the modelling parameters adopted, corannulene is estimated to spend roughly 60 per cent of its time in the ground vibrational state, the remaining 40 per cent being divided in a large number of different metastable states. A fraction of the pure rotational emission of the molecule occurs then from such states, in which rotational constants are slightly different from those of the ground vibrational state. Rotational lines from such metastable vibrational states are displaced from those emitted from the ground vibrational state, and do not contribute to the observed line intensity. The estimated time spent in the metastable state depends on the assumed radiation field, and therefore on the spatial distribution of corannulene within the nebula, which we assumed to be in the halo similarly to the observed 11.3 μm emission (Waters et al. 1998). If it is instead located more similarly to the 3.3 μm emission, which is closer to the central source, the photon absorption rate would be higher, the fraction of time spent in the ground state lower. The reverse is true if corannulene is located further away from the source than we assumed. The fraction of time spent in the ground vibrational state depends also on our assumptions for the Einstein coefficients for the IR–inactive modes (Mulas et al. 2006a). If corannulene turned out to have very unusual intensities for electric quadrupole vibrational transitions, with respect to IR-active ones, this would correspondingly change the estimated lifetimes of the metastable states.

The associated emission in the rotational levels is shown in Fig. 2, where a full width at half-maximum (FWHM) of 1 km s^{-1} is assumed and no scaling factor was applied to account for metastable states. The resulting rotational spectrum is expected to have its most intense lines around 150 GHz and to be spread over a few hundreds GHz with a line spacing of about 1 GHz.

3 LABORATORY WORK

Corannulene is a polar, symmetric-top PAH with a bowl shaped structure (see Fig. 1). The rotational energy levels of symmetric-top molecules are segregated into series of K-stacks, distinguished by the value of the rotational angular momentum K along the molecular symmetry axis. For parallel bands, the selection rule for the K quantum number is $\Delta K = 0$, so that only levels within the same stack can be connected through a rotational transition. In an ideal rigid symmetric top molecule, the J → J+1 transition has the same frequency along each stack, but in reality centrifugal distortion generally separates the transitions in well resolved lines, the high-J transitions being more affected by this effect. The high-resolution rotational spectrum of corannulene has been measured by Lovas et al. (2005) by Fourier transform microwave spectroscopy (FTMW) up to J = 19 with no K-splitting observed up to this line, leading to an upper limit of $\Delta_{JK} = 2.3 \times 10^{-6}$ for the centrifugal distortion constant. For a radio astronomical detection, higher J transitions ($J > 100$) are required because of the expected excitation pattern of corannulene by the impinging UV radiation field. It is thus of great importance to know whether K-splitting is still negligible for high-J transitions.

Our laboratory measurements were performed using the Intracavity OROTRON jet spectrometer in Cologne, which is characterized by a frequency range of 112–156 GHz and a frequency resolution of 10–15 kHz (Surin et al. 2001). In this setup, both the millimeter

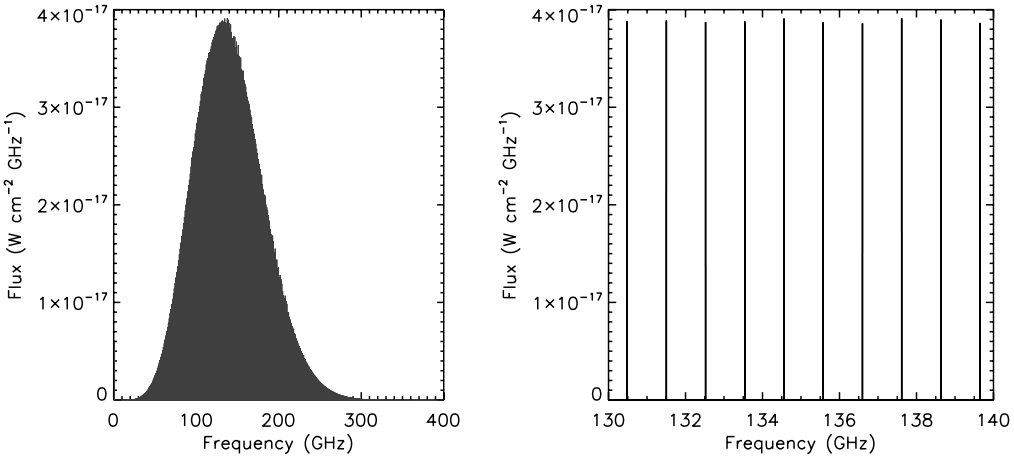

Figure 2. The rotational emission spectrum of corannulene in the RR calculated with the Monte Carlo model peaks around 150 GHz (left-hand panel) and is spread over a few hundreds GHz, with a spacing of about 1 GHz as shown by the zoom of a small region around the maximum (right-hand panel). In the figure, a FWHM of 1 km s^{-1} has been assumed for the lines. The plot refers to the emission of corannulene molecules situated in the halo of the RR, and has been normalized assuming that all the AIB flux measured by *ISO*-SWS was due to corannulene.

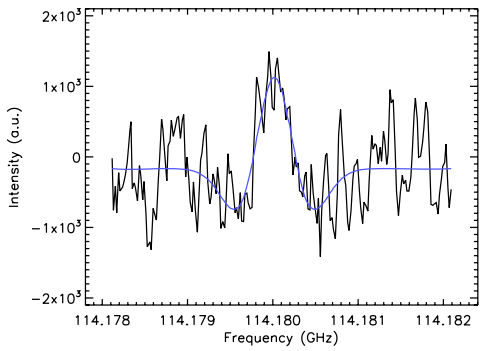

Figure 3. The line detection at 114.18 GHz measured in the laboratory with the OROTRON jet spectrometer, assigned to the J = 112 ← 111 transition of corannulene.

wave generator OROTRON and the supersonic jet apparatus are placed inside a vacuum chamber. Corannulene was prepared by solution phase methods (Sygula et al. 2001) and purified by chromatography on silica gel. The sample was crystalline powder which was evaporated at a temperature of about 170°C, and injected into the OROTRON cavity via a heated pinhole nozzle with Helium as carrier gas. A backing pressure of about 1 bar and a jet repetition rate of 5–10 Hz were used. At 114.18 GHz, a weak spectral feature was recorded after 10 min of integration time, which has been assigned to the J = 112 ← 111 transition of corannulene (see Fig. 3). The central frequency is in agreement with predictions based on the spectroscopic constants obtained from the FTMW measurements to within 250 kHz. The line shows no K-splitting from which can be concluded that the corannulene molecule is very rigid. Therefore, the intensities of different K-stack transitions sum up, enhancing the total intensity of each J → J+1 line by a factor of some tens, depending on the temperature of the gas (Thaddeus 2006). Combining the effects of polarity and the stiffness of the molecule, the intensity of the radio spectrum of corannulene is expected to be 3–4 orders of magnitude stronger than that of a typical polar PAH of the same size and abundance, making corannulene an excellent candidate for radio astronomical detection. The rotational constants derived from the laboratory work have been used to refine the band positions given in the synthetic spectrum. For the measurement of the corannulene line described in this paper, 30 mg of corannulene had to be spent. Further laboratory measurements in the mm-waveband are in progress and will be described in more detail elsewhere (Herberth, Giesen, in preparation).

4 SOURCE DESCRIPTION AND OBSERVATIONS

The RR is a biconical C-rich nebula which surrounds a post-asymptotic giant branch (AGB) binary system composed of the primary star HD 44179 (spectral type A0) and its luminous giant companion. It has been observed in the mid-IR with the SWS instrument onboard *ISO* and with the Infrared Spectrograph (IRS) onboard the *Spitzer Space Telescope*. The dimensions on the plane of the sky of the infrared bipolar nebula at 11.3 μm are about 10 × 20 arcsec^2 (Waters et al. 1998). A warm, high density disc ($n_H > 3\ 10^4$ cm^{-3}, 30 K < T < 400 K) traced by CO emission (Bujarrabal et al. 2005) surrounds the binary star with a thickness of roughly 3 arcsec along the symmetry axis.

Observations were performed with the IRAM 30-m telescope in Pico Veleta in 2008 February. The observed frequency ranges cover several high-J transitions of $C_{20}H_{10}$ at 1, 2 and 3 mm. Weather conditions were acceptable for most of the time. We used the wobbling secondary observing mode, with a beam separation of ±100 arcsec in azimuth. This observing mode ensures stable and flat baselines and is well adapted to compact sources such as the RR.

Pointing was made on the central binary star HD44179 (α_{2000}: 06:19:58.216, δ_{2000}: −10:38:14:691). Mars and Orion (α_{2000}: 05:35:14.5, δ_{2000}: −05:22:30.00) were used as reference sources for calibration and pointing. Pointing was accurate within 3 arcsec during all observations. The flexibility of the four receivers and of the VESPA correlator allowed to cover several frequency ranges within one configuration, with a spectral resolution of 40 kHz and a total band pass of at least 40 MHz. We also used the 1 MHz resolution filter banks to obtain broad-band spectra (250 MHz) with lower spectral resolution. During all observations, one of the back ends was dedicated to the ^{13}CO (1–0), (2–1) or ^{12}CO(2–1) transition, to check whether the telescope was pointed on source, and to monitor the calibration accuracy. The observed ^{12}CO intensity and line width are in good agreement with previous observations of the RR with the IRAM 30-m telescope reported in Jura, Balm & Kahane (1995). The summary of the ^{12}CO and ^{13}CO observations are reported in Table 1.

To improve the quality of the observed spectra, we manually cut isolated spikes out of 4σ (the two nearest channels being lower than 3σ), and discarded observations with anomalous system temperature or with a high sky opacity. Different observations of the same transitions were averaged, and the antenna temperature was scaled with the telescope main beam efficiency by the relation $T_{mb} = T_A^*/\eta_{mb}$, where $\eta_{mb} = F_{eff}/B_{eff}$. The central frequency, beamwidth, beam efficiency, system temperature, rms level and bandwidth are reported in Table 2 for each of the observed frequency ranges. The expected flux derived from the synthetic spectrum and the 3σ detection limit corrected for beam dilution are also reported for the corannulene observations. The rms level was calculated after smoothing the spectra to the velocity resolution of 0.4 km s^{-1}. In Fig. 4, we show the observed spectra in the regions where the 135 → 134 and 86 → 85 transitions of $C_{20}H_{10}$ are expected, and the ^{12}CO and ^{13}CO observations (further plots can be found in the electronic version of the article – see Supporting Information). We did not detect any corannulene line at any frequency. The best rms level for corannulene has been obtained for the transitions J+1 → J = 135 → 134, 84 → 83 and 86 → 85.

Table 1. Summary of ^{12}CO and ^{13}CO observations towards the RR.

Transition (J+1 → J)	Frequency (GHz)	Beam size (arcsec)	B_{eff}	T_{sys} (K)	Area (K km s^{-1})	Bandwidth (MHz)
^{12}CO (2 → 1)	230.538	10	0.52	486	6.8	40
^{13}CO (1 → 0)	110.201	22	0.75	159	0.3	40
^{13}CO (2 → 1)	220.398	11	0.55	339	1.7	40

Table 2. Summary of the observations towards the RR in different frequency ranges, corresponding to the expected rotational transitions of corannulene. On average, the 3 mm observations have a lower rms, but suffer more from beam dilution effects compared to the 1 mm observations.

Transition (J+1 → J)	Frequency (GHz)	Beam size (arcsec)	$B_{\rm eff}$	$T_{\rm sys}$ (K)	$\sigma_{\rm mb}$ (mK)	Bandwidth (MHz)	$F_{3\sigma}$ (10^{-25} W cm^{-2})	$F_{\rm model}$ (10^{-21} W cm^{-2})
84 → 83	85.643	29	0.78	117	10	80	1.4	5.7
86 → 85	87.682	28	0.77	107	12	80	1.7	6.2
108 → 107	110.104	22	0.75	170	14	80	1.6	13
111 → 110	113.316	22	0.74	276	21	120	2.3	14
135 → 134	137.615	17	0.70	219	8	80	0.9	19
215 → 214	219.059	11	0.55	346	45	80	5.4	5.3
216 → 215	220.076	11	0.54	328	20	80	2.4	5.2
223 → 222	227.197	11	0.53	269	23	80	2.9	4.0
226 → 225	230.248	11	0.52	389	30	80	3.8	3.7
238 → 237	242.450	10	0.50	525	22	80	2.8	2.3
257 → 256	261.763	8	0.46	546	39	40	5.4	0.9

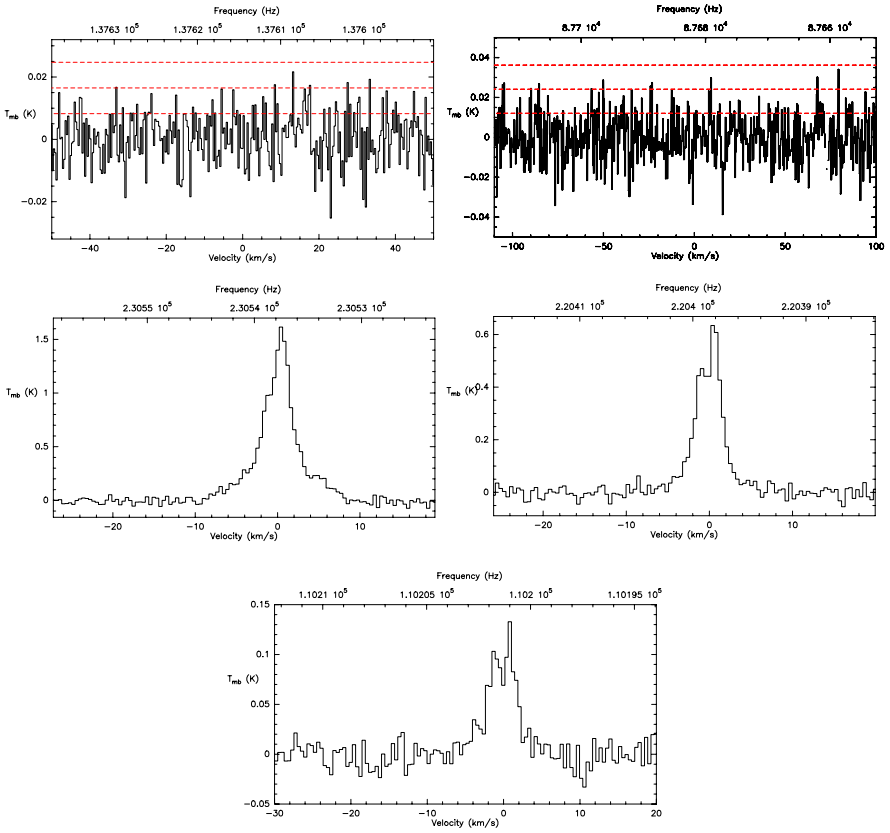

Figure 4. Observations of the expected frequency range for the 135 → 134 transition at 137 GHz, the 86 → 85 transition at 88 GHz of $C_{20}H_{10}$, the ^{12}CO(1–0) and ^{13}CO(1–0), (2–1) transitions. Horizontal red lines indicate the first 3σ levels. See the electronic version of the article (Supporting Information) for further plots.

5 RESULTS AND DISCUSSION

To calculate an upper limit to the abundance of corannulene in the source, we assumed a 3σ detection limit and a Gaussian profile with a FWHM of 1 km s^{-1}. Before comparing the observed rms to the model, we have to take into account the effect of beam dilution. As a first approximation, we assume that PAH emission is distributed homogeneously in a 20 × 10 arcsec^2 area as observed for AIB emission (Waters et al. 1998).

The best noise levels are reached, on average, with the 3 mm observations, but the 1 and 2 mm observations suffer less from beam dilution. To compute a reliable upper limit to the abundance of corannulene, we chose the 135 → 134 transition at 2 mm, which is not only the transition with the lowest rms, but also the best compromise between the loss of flux due to beam dilution and expected intensity derived from the synthetic spectrum.

The synthetic spectrum has been normalized as if all the AIB flux was due to corannulene, as explained in Section 2. The ratio between observations and theoretical predictions can be turned into an upper limit for the fraction of AIB flux due to corannulene, which corresponds to the fractional abundance of carbon locked up into corannulene relative to the total abundance of carbon in PAHs. The synthetic spectrum predicts for the 135 → 134 transition an integrated flux of $F_{\rm model} = 1.9 \times 10^{-20}$ W cm^{-2}. We compare this value with the area of the 3σ Gaussian for the same transition, corrected for beam dilution: $F_{3\sigma} = 9.0 \times 10^{-26}$ W cm $^{-2}$.

An upper limit for the fraction of carbon in $C_{20}H_{10}$ compared to the total abundance of carbon locked in PAHs can be obtained by the ratio $F_{3\sigma}/F_{\rm model}$. This ratio has to be modified to take into account the fact that emitting $C_{20}H_{10}$ is not always in its ground state. An average factor of 0.6 was derived in Section 2. Also, the resulting estimate applies for the $C_{20}H_{10}$ main isotope. Different isotopologues have slightly different rotational constants, which have rotational lines in displaced positions. Assuming standard Solar system isotopic ratios and no fractionation, about 25 per cent of corannulene molecules are expected to contain one or more ^{13}C atoms which results in an additional correction. Substitutions of ^{1}H with ^{2}D occur in a negligible fraction of the molecules. In a circumstellar envelope around a post-AGB star, isotopic ratios depend on the detailed history of the last phases of its precursor, and can be significantly different from the accepted solar values. For the RR, recent observations however failed to detect isotopomers of C_2, CN and CH containing ^{13}C, setting a lower limit of 22 for the ^{12}C/^{13}C ratio in the RR nebula (Bakker et al. 1997). Assuming this ratio, instead of the standard value of 89, would result in a factor of 1.7 for our final lower limit on the abundance and column density of corannulene. Given that the ^{12}C/^{13}C ratio in the RR must be $\geq$22, this does not significantly alter our conclusions.

With these assumptions, and solar ^{12}C/^{13}C ratio, we derive a value of 1.0×10^{-5} as our best limit for the fraction of carbon in $C_{20}H_{10}$ relative to the total carbon in all PAHs. Assuming that ∼20 per cent of total carbon atoms are locked in PAHs (Joblin et al. 1992; Tielens 2005), this turns into a value of 2.0×10^{-6} of total carbon in corannulene. This result is much more stringent than the limit derived by Thaddeus (2006) for corannulene in TMC-1, 1×10^{-5}.

This can be compared with the models of the size distributions of interstellar PAHs in the literature. With a the PAH radius, Désert, Boulanger & Puget (1990) used a size distribution $N_{\rm PAH}(a) \propto a^{-2}$ whereas Draine & Lazarian (1998) proposed a lognormal distribution. Assuming that the fraction of carbon locked in PAHs relative to hydrogen is 6×10^{-5} (Joblin et al. 1992; Li & Draine 2001), we can use the derived upper limit to constrain the corannulene abundance (relative to hydrogen) to be $N_{C_{20}H_{10}}/N_{\rm H} < 3 \times 10^{-11}$.

Fig. 5 shows both distributions using the relation $a = 0.9\sqrt{N_{\rm C}}$ Å for compact molecules (Omont 1986) and normalizing the carbon content in PAHs to 6×10^{-5} relative to hydrogen. In the figure, the distributions are represented as histograms with a bin size of 1 in $N_{\rm C}$, to be directly comparable with the upper limits derived for corannulene (this work) and for the larger species $C_{42}H_{18}$ that has been measured in the visible range for the diffuse ISM (Kokkin et al. 2008). It is difficult to assess the significance of such a straight comparison, however, since on one side we have a specific molecule and its abundance, on the other side we have the summed abundance of all PAHs in the same size bin. This would involve considering all isomers with the same chemical formula, and assuming some relative abundances among them. In the absence of more specific information, we will use the experimental results cited in Section 1 about the minimum mass fraction of corannulene that is always formed in pyrolysis experiments. In the chromatograms of the aromatic species produced in such flames, a few tens of species appear to constitute most of the mixture of molecules with less than 100 C atoms, fewer than 10 of them being by far more abundant (Lafleur et al. 1993).

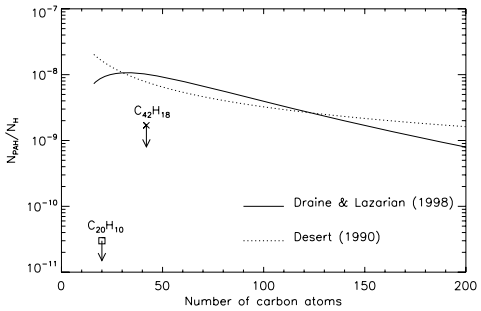

Figure 5. Size distributions of PAHs according to Désert et al. (1990) and Draine & Lazarian (1998), normalized to a carbon abundance in PAHs of 6×10^{-5} relative to hydrogen (Joblin et al. 1992; Draine & Lazarian 1998). The two upper limits reported refer to the observations of corannulene in the RR (this paper) and of $C_{42}H_{18}$ in the diffuse ISM (Kokkin et al. 2008). The discrepancy between models and observations supports the photodestruction of small PAHs in space.

Using the PAH spectral data base (Malloci et al. 2007), we determined that, for neutral PAHs, there is a tight linear correlation (correlation coefficient $r = 0.94$) between the number of carbon atoms and the absorbance integrated in the (236–500) nm range used by the chromatogram in fig. 3 of Lafleur et al. (1993). This means that we can use these integrated absorbances to quantify $N_{\rm C}$ for each identified PAH in that chromatogram. We then derived the mass fraction of pyrene compared to all PAHs, and that of corannulene, assuming it corresponds to 1 per cent of the pyrene mass, which is the lowest value reported by Lafleur et al. (1993). This leads to a lower limit of $\sim 4 \times 10^{-4}$ for the fraction in mass of corannulene in the mixtures of small PAHs produced in such experiments. Together with our observational upper limit on the fraction of carbon atoms in corannulene with respect to the total in all PAHs, this yields an upper limit of ∼2 per cent for the mass fraction of small PAHs with respect to the total (3.4 per cent assuming the lower limit for ^{12}C/^{13}C). Integrating the two size distributions (see Fig. 5) in the small molecule range ($N_{\rm C} \leq 50$) leads to a fraction of carbon in small PAHs versus the total of ∼19 per cent, an order of magnitude larger than our upper limit. Based on the general assumption that the formation of PAHs in evolved stars can be described by flame chemistry (cf. Section 1), we can conclude that small PAHs in the RR are significantly less abundant than the values predicted by the size distributions reported in Fig. 5.

The underabundance of small PAHs in the RR can be due either to selective destruction of small-sized PAHs (Allain, Leach & Sedlmayr 1996b,a; Le Page, Snow & Bierbaum 2003) or to the fact that PAHs grew to larger sizes directly in the C-rich outflow

of the RR nebula progenitor where they were originally synthesized. Interestingly, the analysis of observations of the 3.3 μm AIB and its overtone at 1.68 μm in the young planetary nebula IRAS 21282+5050 showed that PAHs emitting in these bands contain about 60 C (Geballe et al. 1994). This rises the question of the minimum size of PAHs that are formed in evolved stars, an important issue considering that these PAHs also appear to be the parental species of interstellar PAHs (Joblin et al. 2008).

To determine whether photodissociation can destroy small PAHs in the RR halo, we estimated the rate of the dominant photodissociation channel for corannulene, namely the loss of an H atom, as a function of the internal energy U. This dissociation rate $k_d(U)$ was calculated using the results on the coronene cation ($C_{24}H_{12}^+$) from the PIRENEA set-up (Joblin et al., in preparation), and including corrections for the variation of the density of states between $C_{20}H_{10}$ and $C_{24}H_{12}^+$ [cf. formula (7) in Boissel et al. (1997)]. We combined this rate with the distribution of excitation energies of $C_{20}H_{10}$ in the RR halo obtained from the Monte Carlo simulation discussed above. Multiplying the two and integrating, we obtained a photodissociation rate of $\sim 1.1 \times 10^{-8}$ s^{-1}, corresponding to a lifetime of $\sim$2.9 yr. The reaction rate of dehydrogenated corannulene with H can be estimated at a value of at least 2×10^{-5} s^{-1}, using a rate coefficient of $\sim 2 \times 10^{-10}$ cm^3 s^{-1} (Le Page et al. 1999) and a hydrogen density larger than 10^5 cm^{-3} (Men'shchikov et al. 2002). This is several orders of magnitudes larger than the dissociation rate. Therefore, corannulene is expected to survive in its neutral hydrogenated form in the RR nebula.

From this work, we can conclude that radio spectroscopy can be a powerful tool to detect specific polar PAHs. Our results in the RR show that it can also be an efficient way to constrain the abundance of small PAHs. Our analysis of these results suggests that the underabundance of small PAHs in the RR is related to the production mechanism for these species and not to subsequent UV destruction. This conclusion will have to be further tested by both observations in other environments and by laboratory studies on the formation of PAHs in conditions that mimic the environment of evolved carbon stars.

ACKNOWLEDGMENTS

We thank the referee for his useful comments. This work was supported by the European Research Training Network Molecular Universe (MRTN-CT- 2004-512302), and the CNRS PICS 4260 'Croissance et destruction des macromolécules carbonées interstellaires', which are acknowledged. PP acknowledges also financial support from the Master & Back program of the 'Regione Autonoma della Sardegna'. Financial support from the U.S. National Science Foundation (Department of Energy), the Deutsche Forschungsgemeinschaft and the Land Niedersachsen are also gratefully acknowledged. GM and GM acknowledge financial support by MIUR under project CyberSar, call 1575/2004 of PON 2000-2006.

REFERENCES

Allain T., Leach S., Sedlmayr E., 1996a, A&A, 305, 602
Allain T., Leach S., Sedlmayr E., 1996b, A&A, 305, 616
Allamandola L. J., Tielens A. G. G. M., Barker J. R., 1985, ApJ, 290, L25
Allamandola L. J., Tielens A. G. G. M., Barker J. R., 1989, ApJS, 71, 733
Bakker E. J., van Dishoeck E. F., Waters L. B. F. M., Schoenmaker T., 1997, A&A, 323, 469
Bernè O. et al., 2007, A&A, 469, 575
Boissel P., de Parseval P., Marty P., Lefèvre G., 1997, J. Chem. Phys., 106, 4973
Boulanger F., Falgarone E., Puget J. L., Helou G., 1990, ApJ, 364, 136
Bujarrabal V., Castro-Carrizo A., Alcolea J., Neri R., 2005, A&A, 441, 1031
Cecchi-Pestellini C., Malloci G., Mulas G., Joblin C., Williams D. A., 2008, A&A, 486, L25
Cernicharo J., Heras A. M., Tielens A. G. G. M., Pardo J. R., Herpin F., Guélin M., Waters L. B. F. M., 2001, ApJ, 546, L123
Chang T.-M., Naim A., Ahmed S. N., Goodloe G., Shevlin P. B., 1992, J. Am. Chem. Soc., 114, 7603
Cherchneff I., Barker J. R., Tielens A. G. G. M., 1992, ApJ, 401, 269
Désert F.-X., Boulanger F., Puget J. L., 1990, A&A, 237, 215
Donn B., 1968, ApJ, 152, L129
Draine B. T., Lazarian A., 1998, ApJ, 508, 157
Foing B. H., Ehrenfreund P., 1994, Nat, 369, 296
Frenklach M., Feigelson E. D., 1989, ApJ, 341, 372
Galazutdinov G. A., Krełowski J., Musaev F. A., Ehrenfreund P., Foing B. H., 2000, MNRAS, 317, 750
Geballe T. R., Joblin C., D'Hendecourt L. B., Jourdain de Muizon M., Tielens A. G. G. M., Leger A., 1994, ApJ, 434, L15
Haymet A. D. J., 1986, J. Am. Chem. Soc., 108, 319
Iglesias-Groth S., Manchado A., García-Hernández D. A., González Hernández J. I., Lambert D. L., 2008, ApJ, 685, L55
Joblin C., Léger A., Martin P., 1992, ApJ, 393, L79
Joblin C., Toublanc D., Boissel P., Tielens A. G. G. M., 2002, Mol. Phys., 100, 3595
Joblin C., Szczerba R., Berné O., Szyszka C., 2008, A&A, 490, 189
Jura M., Balm S. P., Kahane C., 1995, ApJ, 453, 721
Kokkin D. L., Troy T. P., Nakajima M., Nauta K., Varberg T. D., Metha G. F., Lucas N. T., Schmidt T. W., 2008, ApJ, 681, L49
Kroto H., 1988, Sci, 242, 1139
Lafleur A. L., Howard J. B., Marr J. A., Yadav T., 1993, J. Phys. Chem., 97, 13539
Le Page V., Keheyan Y., Snow T. P., Bierbaum V. M., 1999, Int. J. Mass Spectrom. Ion Process., 185, 949
Le Page V., Snow T. P., Bierbaum V. M., 2003, ApJ, 584, 316
Léger A., Puget J. L., 1984, A&A, 137, L5
Léger A., d'Hendecourt L., 1985, A&A, 146, 81
Léger A., d'Hendecourt L., Defourneau D., 1989, A&A, 216, 148
Li A., Draine B. T., 2001, ApJ, 554, 778
Lovas F. J., McMahon J., Grabow J. U., Schnell M., Mack J., Scott L., Luczkowsky L., 2005, J. Am. Chem. Soc., 127, 4345
Malloci G., Joblin C., Mulas G., 2007, Chem. Phys., 332, 353
Men'shchikov A. B., Schertl D., Tuthill P. G., Weigelt G., Yungelson L. R., 2002, A&A, 393, 867
Mulas G., 1998, A&A, 338, 243
Mulas G., Malloci G., Joblin C., Toublanc D., 2006a, A&A, 460, 93
Mulas G., Malloci G., Joblin C., Toublanc D., 2006b, A&A, 456, 161
Mulas G., Malloci G., Joblin C., Toublanc D., 2006c, A&A, 446, 537
Omont A., 1986, A&A, 164, 159
Pech C., Joblin C., Boissel P., 2002, A&A, 388, 639
Peeters E., Hony S., Van Kerckhoven C., Tielens A. G. G. M., Allamandola L. J., Hudgins D. M., Bauschlicher C. W., 2002, A&A, 390, 1089
Platt J. R., 1956, ApJ, 123, 486
Rapacioli M., Joblin C., Boissel P., 2005, A&A, 429, 193
Rouan D., Leger A., Omont A., Giard M., 1992, A&A, 253, 498
Sarre P. J., Miles J. R., Scarrott S. M., 1995, Sci, 269, 674
Scarrott S. M., Watkin S., Miles J. R., Sarre P. J., 1992, MNRAS, 255, 11P
Schmidt G. D., Cohen M., Margon B., 1980, ApJ, 239, L133
Surin L. A., Dumesh B. S., Lewen F., Roth D. A., Kostromin V. P., Rusin F. S., Winnewisser G., Pak I., 2001, Rev. Sci. Instrum., 72, 6
Sygula A., Xu G., Marcinow Z., Rabideau P., 2001, Tetrahedron, 57, 3637
Thaddeus P., 2006, Phil. Trans. R. Soc., 361, 1681
Thorwirth S., Theulé P., Gottlieb C. A., McCarthy M. C., Thaddeus P., 2007, ApJ, 662, 1309
Tielens A. G. G. M., 2005, The Physics and Chemistry of the Interstellar Medium, ISBN 0521826349. Cambridge Univ. Press, Cambridge
van der Zwet G. P., Allamandola L. J., 1985, A&A, 146, 76

Van Winckel H., Cohen M., Gull T. R., 2002, A&A, 390, 147
Vijh U. P., Witt A. N., Gordon K. D., 2004, ApJ, 606, L65
Vijh U. P., Witt A. N., Gordon K. D., 2005, ApJ, 633, 262
Waters L. B. F. M. et al., 1998, Nat, 391, 868

SUPPORTING INFORMATION

Additional Supporting Information may be found in the online version of this article.

Fig. A1. Observations of the expected frequency range for the pure rotational transitions of corannulene J +1 → J: 108 → 107, 111 → 110, 215 → 214 and 216 → 215.

Fig. A2. Observations of the expected frequency range for the pure rotational transitions of corannulene J +1 → J: 223 → 222, 226 → 225, 238 → 237 and 257 → 256.

Please note: Wiley-Blackwell are not responsible for the content or functionality of any supporting information supplied by the authors. Any queries (other than missing material) should be directed to the corresponding author for the article.

This paper has been typeset from a TEX/LATEX file prepared by the author.

Chapter

8

Production of small hydrocarbons in PDRs

8.1 INTRODUCTION

In PDRs, very small dust particles such as PAHs and eVSGs are processed by the UV radiation. In Chap. 6, we have analysed the photo-destruction process of eVSGs in PDRs that gives birth to free PAHs. Here we will discuss another possible product of this process, that is the production of small gas-phase hydrocarbons.

Hydrocarbon abundances in PDRs

As already introduced in Chap. 3, observational studies on PDRs have revealed that gas-phase chemical models provide too low values of the abundance of small hydrocarbons compared to that observed in several PDRs: NGC 7023 (Fuente *et al.*, 2003), the Orion Bar (Fuente *et al.*, 2003), IC63 Teyssier *et al.* (2004) and the Horsehead nebula (Teyssier *et al.*, 2004; Pety *et al.*, 2005). Several reasons may be invoked to explain this discrepancy:

- the photo-dissociation rates for hydrocarbons used in the models may not be accurate,
- the chemical models may lack important gas-phase reactions in the formation of the small hydrocarbons,
- the models are biased by not taking into account non gas-phase pathways of small hydrocarbons production such as the photo-destruction of larger species such as the AIB carriers.

Recently, high spatial resolution observations and detailed modelling of the Horsehead Nebula (Pety *et al.*, 2005) have shown that the latter mechanism is very promising to explain the discrepancy between observations and models. The authors showed a very good spatial correspondence between the AIB and the small hydrocarbon emission. However, since both PAHs and eVSGs contribute to the AIBs, it is not possible to conclude whether the destruction of one or the other population is the source of enhanced hydrocarbon abundance in the external layers of PDRs. In the Horsehead nebula, there is a strong density gradient (Habart *et al.*, 2005) and no spatial transition between the PAH/eVSG populations can be observed at the resolution of the Infrared Spectrograph (IRS) onboard Spitzer. In the north-west PDR of NGC 7023, the transition between the different AIB carriers is very well resolved by IRS (see Fig. 6.2): PAH^+ are mostly located in the low density medium (the so called *cavity*), PAH^0 at the PDR interface, and eVSGs further inside the molecular cloud. The transitions between the different populations are observed at typical scales of a few arcseconds. Observations at the IRAM 30m telescope towards NGC 7023 (Fossé *et al.*, 2000; Fuente *et al.*, 2003) reported detections of several hydrocarbon species such as c-C_3H_2 and C_2H towards both the PDR peak and the molecular cloud. The authors showed that chemical modeling predicts much lower abundance (by one order of magnitudes) for these molecules towards the PDR peak, but the large beam ($12'' - 27''$) at the observed frequencies did not allow a detailed spatial study. Observations of these species at high angular resolution are therefore essential to constrain the contribution of the fragmentation of PAHs and eVSGs to the hydrocarbon abundance in this prototype object.

The aliphatic-aromatic evolution in PDRs

The loss of aliphatic side-groups attached to very small carbonaceous grains or PAHs is a possible production pathway for small hydrocarbons in PDRs. Whereas pure aromatic compounds have sp^2 hybridisation, aliphatics are linked through sp^1 bonds. Such bonds are less stable against photo-dissociation than aromatic bonds, and upon absorption of UV photons they are therefore expected to be the first to break (Joblin *et al.*, 1996a). The observation and analysis of the aliphatic/aromatic evolution in the mid-IR is difficult since the bands associated with these transitions overlap and their contribution cannot be easily disentangled. Nevertheless, the combination of laboratory studies and observations suggests that complexes containing both aliphatic and aromatic groups

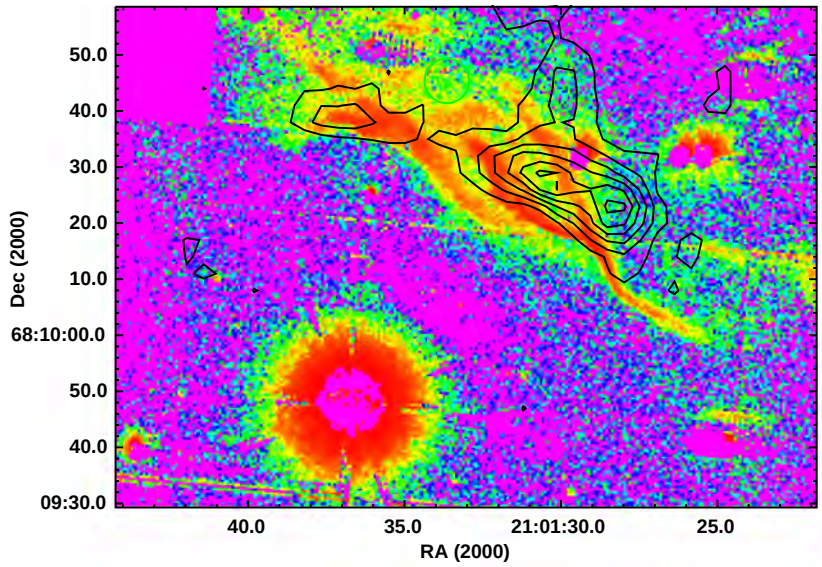

Figure 8.1: The north-west PDR of NGC 7023 observed in the H_2 2.1 μm emission (colorscale, Lemaire *et al.*, 1996) and the C_2H emission observed at the PDBI with contours of 0.25 K km s^{-1} (A. Fuente, private communication)

are evolving in PDRs (Sloan *et al.*, 2007) and circumstellar disks (Acke *et al.*, 2010). The near-IR domain offers the opportunity to study the aliphatic/aromatic evolution because aliphatic complexes have an intense vibrational mode at 3.4 μm, which can be well distinguished from the 3.3 μm aromatic band. Indeed, previous observations of PDRs (Geballe *et al.*, 1989; Joblin *et al.*, 1996a; Sloan *et al.*, 1997) show a spatial variation of the 3.4/3.3 μm band ratio, this ratio decreasing with longer exposure to UV photons.

This chapter presents the results and preliminary analysis of the high-angular resolution observations of different hydrocarbon lines in NGC 7023 NW. The data will be complemented by recent AKARI near-IR observation of the same source, that will enable to set up the study of the aliphatic/aromatic transition as given by the 3.4 μm band. The results of these observations will be also discussed in relation with the mid-IR decomposition presented in Chap. 5.

8.2 Interferometric observations

NGC 7023 NW was observed with the Plateau de Bure Interferometer (PDBI) in the C_2H ($1 \rightarrow 0$) transition at 87.316 GHz, with a beam size of $\sim 5''$ (A. Fuente, priv. comm.). The observed C_2H emission peaks just behind the H_2 emission at 2.1 μm (Lemaire *et al.*, 1996) that traces the high density filaments at the PDR edge (see Fig. 8.1).

Using the PDBI, we observed the north-west PDR of NGC 7023 at the frequencies of several hydrocarbon lines, i.e. c-C_3H_2, C_3H, and C_4H. The corresponding frequencies

are reported in Table 8.1. The observations were performed in the CD configuration[1], leading to an angular resolution of $\sim 3.5''$. The on-source time was about 10 hours with very good weather conditions. The observations consist in a 5-field mosaic with full Nyquist sampling covering the whole filamentary region where C_2H emission arises. The fields of view of the all the fields superposed towards the filaments in correspondence with the C_2H emission to maximise the signal-to-noise ratio in this region. The data were reduced using standard GILDAS[2] tasks (Pety, 2005).

Molecule	Frequency (GHz)	E_{low} (cm^{-1})	Quantum Numbers
c-C_3H	85.272	7.5035	$(3_{1,2}, 5/2, 3) \rightarrow (3_{1,3}, 5/2, 2)$
c-C_3H_2	85.338	1.6332	$2_{1,2} \rightarrow 1_{0,1}$
C_4H	85.634	11.4234	(9,19/2) → (8,17/2)
C_4H	85.672	11.4346	(9,17/2) → (8,15/2)
c-C_3H	85.695	7.4888	$(3_{1,2}, 7/2, 3) \rightarrow (3_{1,3}, 7/2, 3)$

Table 8.1: Transition frequencies, lower state energies and quantum numbers for the interferometric observations.

The interferometric observations filter the large scale emission and they need to be combined with short-spacings information to retrieve the total flux of these lines. The short-spacings observations were performed at the IRAM 30m telescope in the on-the-fly observing mode, covering a $250'' \times 200''$ area centered on the filaments, for a total on-source time of about 6 hours. Both sidebands of the EMIR receivers were used: the LSB was used to observe the same lines as those observed at the PDBI, whereas the USB enabled to map the CS (2-1) transition at 91 GHz. The OFF reference position was chosen in the western lobe of the cavity ($\Delta\alpha = -144''$, $\Delta\delta = -47''$ offsets from HD 200775). Observations of ^{13}CO (1→0) and $C^{18}O$ (1→0) at the 30m telescope (J. Pety, priv. comm.) show a localised emission at blue-shifted velocities ($v_{lsr} \sim -1\,km\,s^{-1}$) at the chosen OFF position. This emission caused a contamination in the final subtracted ON-OFF spectra of c-C_3H_2 at these velocities, which was corrected off-line using specific GILDAS tasks. Typical v_{lsr} for these sources are in the 0-4 $km\,s^{-1}$ range (see, for example, Fuente *et al.*, 1996; Gerin *et al.*, 1998), and therefore the contamination from the OFF to the main line profile is negligible.

In figure 8.2 we show the channel maps of the observed c-C_3H_2 emission at 85.338 GHz and the comparison with the H_2 emission at 2.1 μm of Lemaire *et al.* (1996). Similarly to C_2H, the c-C_3H_2 emission arises mainly towards two regions: the infrared filaments and the northern bulk of the molecular cloud. Towards the filaments, the line peaks at $v_{lsr} = 2.4\,km\,s^{-1}$, which is the same central velocity as C_2H, and the blue-shifted velocities ($1.8 \lesssim v_{lsr} \lesssim 2.4\,km\,s^{-1}$) are mostly localised in this region. The red-shifted

[1]The C and D configurations are the two most compact configurations at the PDBI, with baseline lengths from 24m to 229m

[2]http://www.iram.fr/IRAMFR/GILDAS/

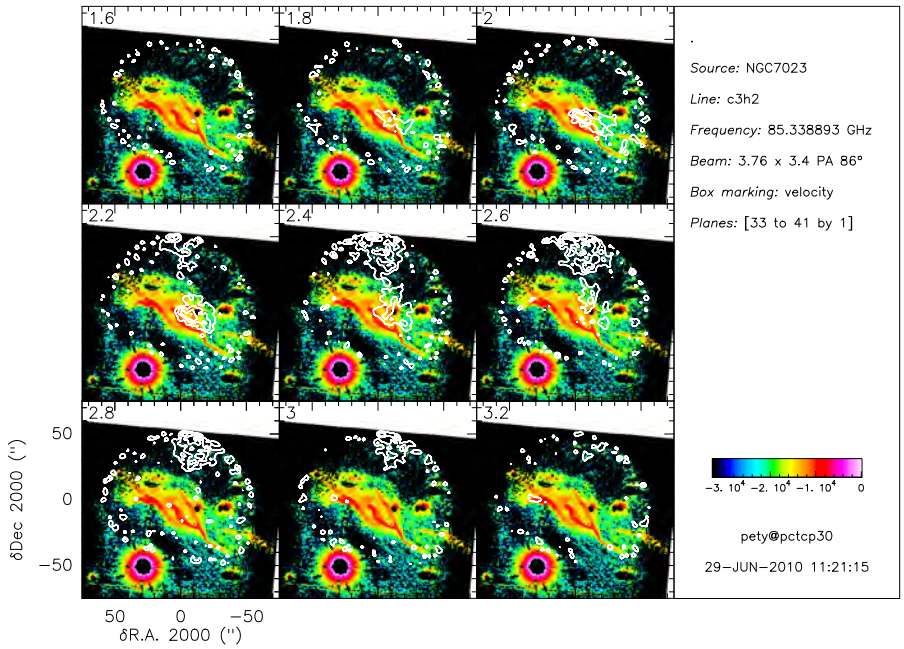

Figure 8.2: Channel maps for the c-C_3H_2 observations (contours) in NGC 7023 NW. The H_2 2.1 μm emission of Lemaire *et al.* (1996) is displayed in colour scale to evidence the high-density filaments at the PDR border. The hydrocarbon emission at $v_{lsr} \lesssim 2.4\,\mathrm{km\,s^{-1}}$ peaks just behind the hot infrared filaments. The more redshifted velocities ($v_{lsr} \gtrsim 2.4\,\mathrm{km\,s^{-1}}$) are associated to the bulk of the molecular cloud.

velocities ($v_{lsr} \gtrsim 2.4\,\mathrm{km\,s^{-1}}$) are mostly localised towards the bulk of the molecular cloud. The signal-to-noise ratio of the C_4H (85.634 and 85.672 GHz) transitions is low, which increases the complexity of the deconvolution process. In any case, the C_4H observations present very localised and faint detections. The C_3H radical was not detected down to a rms level of 100 mK. Figure 8.3 compares the spatial patterns of the emission in the C_2H and c-C_3H_2 lines and the mid-IR decomposition presented in Chap. 5, showing that the hydrocarbon emission peaks toward the eVSG/PAH^0 transition region. Possible interpretations for this spatial coincidence will be addressed in Sect. 8.4.

8.3 AKARI OBSERVATIONS

During the AKARI warm phase, we observed NGC 7023 NW using the IRC camera in spectroscopic mode. These observations were performed in the context of the NESID (Nature and Evolution of Small Interstellar Dust, P.I: F.Boulanger) project. The observations consisted in 20 stripes of length $\sim 50''$ and a pixel size of $3''$. For each spatial pixel, the instrument provides spectroscopy in the 2.5-5 μm range, with a spacing of $\sim 0.01\,\mu$m between channels ($90 \lesssim R \lesssim 160$). The calibration and data reduction for each of the stripes were performed by the Japanese team led by T. Onaka. The stripes

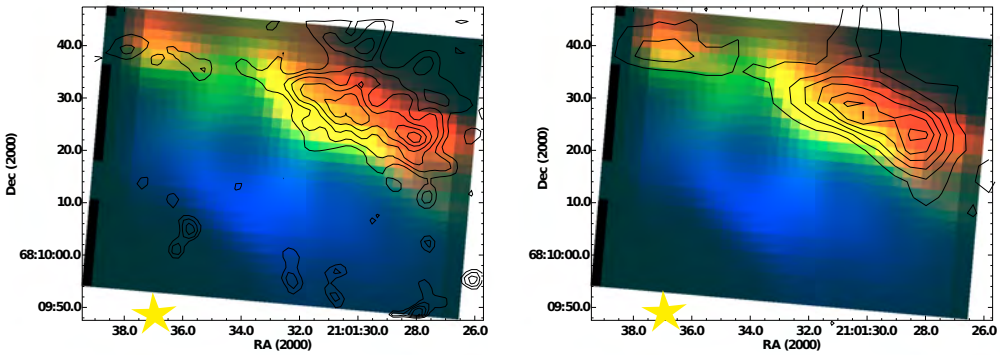

Figure 8.3: The NW PDR of NGC 7023 decomposed in PAH^+ (blue), PAH^0 (green) and eVSGs (red). Contours are c-C_3H_2 (steps of 0.25 K km s^{-1}, *left*) and C_2H (steps of 0.25 K km s^{-1}, *right*).

were then combined in a mosaic using the *montage* software[3]. The field of view of the final mosaic is displayed in Fig. 8.4. Unfortunately, the orientation of the slit could not be specified by the observer, which results in a non-optimised coverage of the PDR.

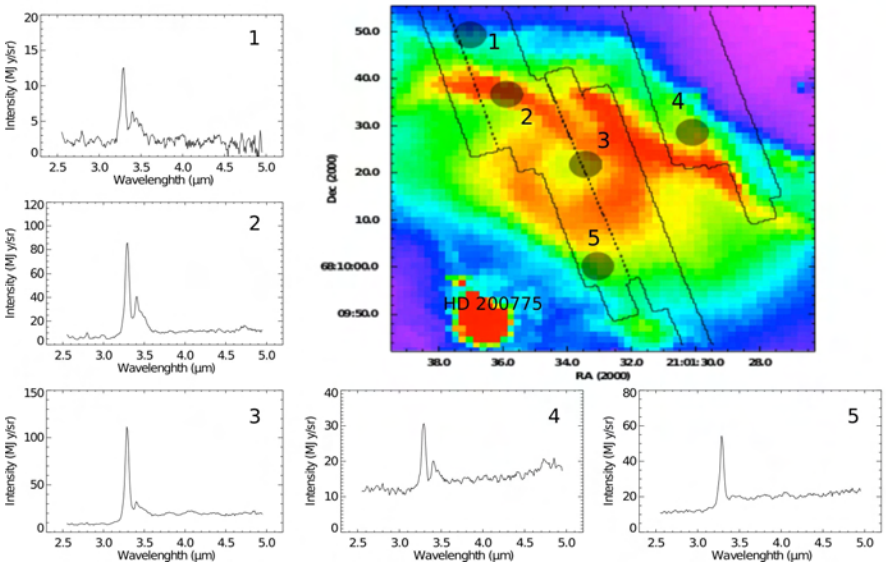

Figure 8.4: AKARI-IRC spectra at five different position in NGC 7023 NW. The positions of the extracted spectra are indicated as grey shadows on the IRAC 8 μm map. Contours trace the complete field of view of the observations. Position 5 is the closest to the star, in the cavity, and does not present any emission at 3.4 μm nor the plateau at 3.5 μm. Position 3 is located towards the PDR edge, and present very low $I_{3.4}/I_{3.3}$. The spectra extracted towards positions 1, 2 and 4, which are located deeper in the PDR, present a higher $I_{3.4}/I_{3.3}$ ratio, indicating that some photo-processing is taking place in the more exposed regions of the PDR.

[3] http://montage.ipac.caltech.edu

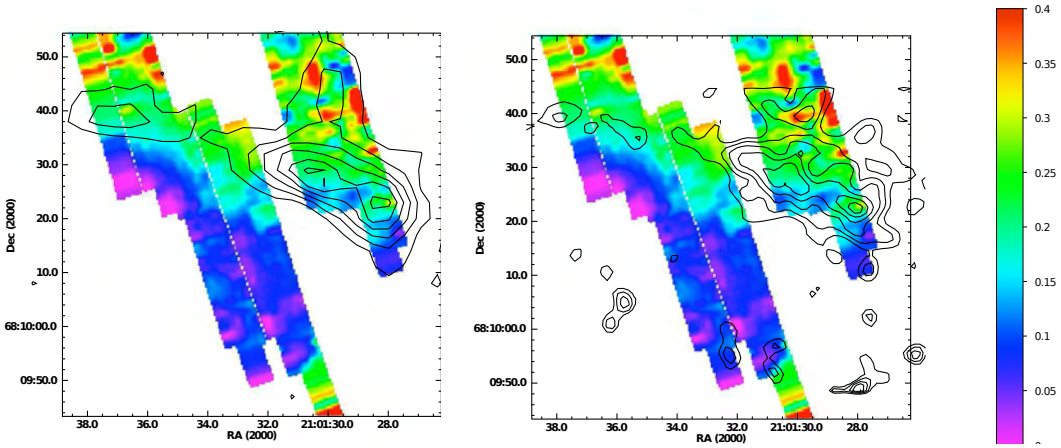

Figure 8.5: First results from the analysis of the AKARI-IRC spectral cubes: the color maps show the variation of the $I_{3.4}/I_{3.3}$ ratio extracted from the near-IR fit. Contours represent the C_2H and c-C_3H_2 emission detected at the PDBI. They are given by steps of $0.25\,\mathrm{K\,km\,s^{-1}}$.

Figure 8.4 shows some examples of AKARI-IRC spectra towards different positions in NGC 7023 NW. In general, the AKARI spectra of NGC 7023 NW show intense 3.3 and 3.4 μm band emission, a plateau in the 3.3-3.5 μm range, and a continuum that spans the whole wavelength range. To extract the intensity of each component separately, we fitted the spectrum in each pixel of the spectral cube with a set of Lorentzians centered at 3.29 and 3.4 μm to represent the main bands, a broader Gaussian centered at 3.5 μm representing the underlying broad feature and a linear continuum. The band FWHMs are $\sim 0.03\,\mu$m for the Lorentzian bands and $\sim 0.1\,\mu$m for the 3.5 μm Gaussian broad band, although these widths may vary at different positions and are set as free parameters in the fit. From the results of the fit, it is clear that the ratio of the 3.4 and 3.3 μm band integrated intensities (hereafter $I_{3.4}/I_{3.3}$) varies with position. In particular, Figs. 8.4 and 8.5 show that $I_{3.4}/I_{3.3}$ increases with distance from the illuminating star HD 200775. The near-IR continuum presents large variations, exhibiting a steep increase around 3.3 μm. Figure 8.5 shows the comparison between the $I_{3.4}/I_{3.3}$ ratio (color scale) and the hydrocarbon emission emission observed at the PDBI (contours as in Fig. 8.3).

8.4 Discussion

On the basis of the observations presented here, we can delineate a general evolution scheme:

1. The emission of the small hydrocarbons such as c-C_3H_2 and C_2H is more intense towards the IR filaments (Figs. 8.1 and 8.2). In particular, Fig.8.6 shows that the spatial patterns of the emissions of these two hydrocarbon lines are tightly corre-

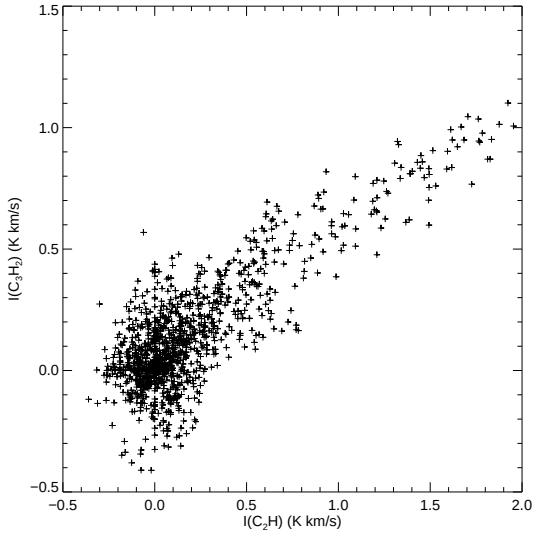

Figure 8.6: Pixel-to-pixel correlation of the integrated intensities of C_2H and c-C_3H_2 in the filamentary region of NGC 7023. The maps have been reprojected to the same grid, with a pixel size of 5″.

lated, as already observed in the Horsehead Nebula, whereas they are predicted to arise at different cloud depths. There are several mechanisms that can contribute to this effect: excitation conditions such as high densities and temperature (Fuente *et al.*, 1996), geometrical issues leading to high column densities (Field *et al.*, 1994), or indeed an enhanced abundance of these molecules. These three possibilities need to be assessed within a complete modelling of the chemistry and physics of the region. The study of the molecular filaments with high-resolution HCO^+ observations have shown that geometrical issues have only a minor impact in this region (Fuente *et al.*, 1996), and therefore the general scenario seems in favour of a combination of favourable excitation effects and an enhanced abundance of hydrocarbons in this region (Fuente *et al.*, 2003).

2. The emission of small hydrocarbons peaks at the transition between eVSGs and PAHs (Fig 8.3), where eVSGs are destroyed to produce free PAHs (Chap. 6). This is coherent with a scenario in which eVSGs are destroyed by the UV field and small hydrocarbons are produced in the same process. This may happen by direct loss of C_nH_m molecules from eVSGs or/and in a two-step process consisting in the production of gas-phase PAHs that can then release their aliphatic sides. It is also possible that hydrocarbons are released from the destruction of PAHs themselves, a process that should affect primarily small PAHs. Laboratory results (Useli Bacchitta and Joblin, 2007; Useli Bacchitta, 2009) show that for small PAHs under UV conditions, the direct loss of small hydrocarbons such as C_2H_2 or C_4H_2 is a possible fragmentation pathway. These species can then further evolve by gas-phase chemistry.

3. Whatever the origin of the 3.4 μm band in super-hydrogenated PAHs or in aliphatic sidegroups attached to PAHs, the spatial evolution of this band is coherent with the photo-processing of PAHs at the PDR front.

4. Interestingly, the peak of hydrocarbon emission in NGC 7023 NW coincides with the region where the Extended Red Emission (ERE) is observed (Fig. 8.7). ERE has been tentatively attributed to some PAH dimers that are expected to be produced during the photo-destruction of eVSGs (Berné *et al.*, 2008). A similar spatial pattern for the ERE is derived in NGC 2023 S, as shown in figure 8.7. However, this PDR has not been observed yet at high angular resolution in hydrocarbon lines. If, as suggested by Berné *et al.* (2008), the carriers of ERE are ionised PAH dimers, the spatial correspondence between the emission of ERE and small hydrocarbons may be due to the fact that all these species are produced in the same photo-destruction process of eVSGs.

To summarise, these observational results are coherent with a scenario that involves the photo-destruction of eVSGs by UV photons, producing a mixture of PAHs, ERE carriers and small hydrocarbons. However, the composition of eVSGs is still unclear. The observations presented here are coherent with eVSGs being a mixture of PAH clusters of various sizes, aliphatic groups and/or super-hydrogenated PAHs. A detailed analysis using PDR models, quantum-chemical calculations and experiments is needed to progress on the nature of these species. A model that quantitatively describes the photo-destruction of PAHs and eVSGs is needed to constrain the destruction processes, and is currently under development at CESR. Experiments on the photo-destruction of eVSGs are also in progress at CESR using the PIRENEA setup (Simon and Joblin, 2009), but face the difficulty of finding a reasonable composition for these interstellar species.

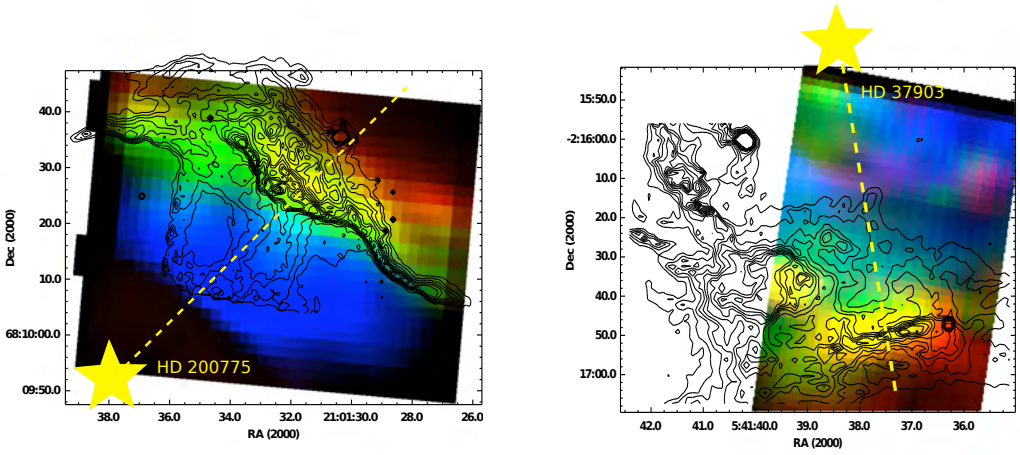

Figure 8.7: The NW PDR of NGC 7023 (*left*) and the South PDR of NGC 2023 (*right*) decomposed in PAH^+ (blue), PAH^0 (green) and eVSGs (red). The extended red emission (ERE) (Berné *et al.*, 2008) is displayed in contours.

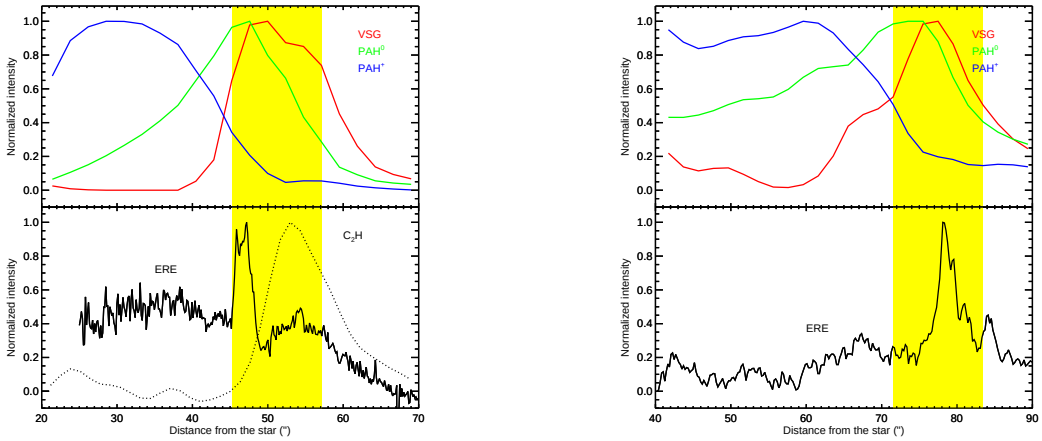

Figure 8.8: A cut along the star-PDR axis in NGC 7023 NW (*left*) and NGC 2023 S (*right*) illustrating the spatial variation of the different emission features. The extended red emission (ERE) peaks at the transition region between eVSGs and PAHs, indicated by the yellow stripe. The C_2H and c-C_3H_2 emissions in NGC 7023 NW are also found in the same region, suggesting that the photo-destruction of eVSGs may be the source of both the ERE carriers and small hydrocarbons.

Part IV

PAHs and gas in the physics of the photo-dissociation region NGC 7023

Chapter

9

On the morphology of NGC 7023

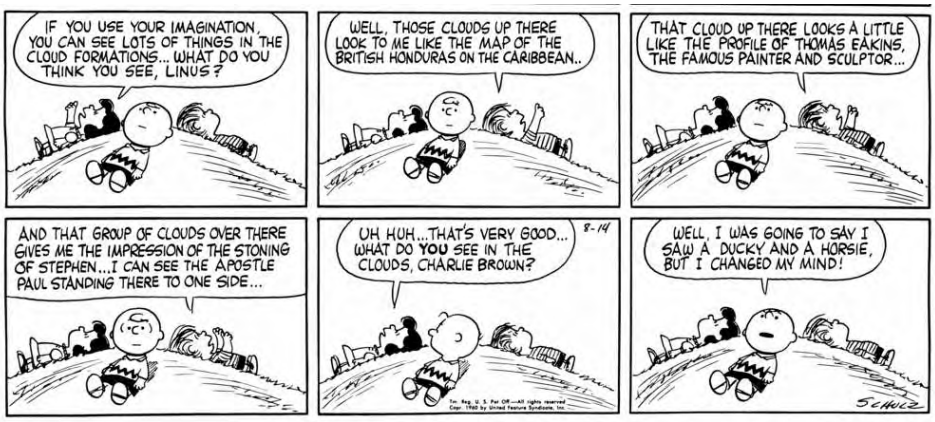

9.1 Introduction

NGC 7023, also called the Iris Nebula, is a reflection nebula in the Cepheus constellation illuminated by the B2-5Ve star HD 200775 [RA(2000) = 21h01m36.9s ; Dec(2000) = +68°09′47.8″]. It has been shaped by the star formation process leading to the formation of a cavity. NGC 7023 has been widely studied at many wavelengths. Recently, it has been mapped by the instruments PACS and SPIRE of *Herschel* to study the emission of large cold grains (Abergel *et al.*, 2010).

Previous molecular observations have shown that this region hosts structures at different gas densities: $n_H \sim 100\,\mathrm{cm}^{-3}$ in the cavity, $\sim 10^4\,\mathrm{cm}^{-3}$ in the PDRs that are located north-west (NW), south (S) and east, and $10^5 - 10^6\,\mathrm{cm}^{-3}$ in dense filaments and clumps that are observed in the mm (Fuente *et al.*, 1996; Gerin *et al.*, 1998, and references therein) and near-IR (Lemaire *et al.*, 1996; Martini *et al.*, 1997). In this chapter,

Figure 9.1: The reflection nebula NGC 7023 observed with the CFHT

.

we combine IR, sub-mm, and mm observations on the gas and dust components to better characterise the regions towards the north-west and south PDRs associated with the central star.

9.2 [C II] and AIB emission: insights from Herschel

The 158 μm [C II] and 63 μm [O I] lines are the major coolants of the gas at the surface of PDRs (Hollenbach and Tielens, 1999). In these regions, photoelectric effect dominates the heating, while H_2 formation provides a minor contribution. Since the smallest dust particles (PAHs and eVSGs) contribute to a large fraction to this process (Bakes and Tielens, 1994; Habart *et al.*, 2001), and these particles emit in the mid-IR most of the energy they absorb in the UV, we expect that the mid-IR and [C II] emissions arise in the same regions. We used the decomposition presented in Chap. 5 to disentangle the $PAH^{+/0}$ and eVSG components in the *Spitzer* IRS (for the star-NW cut) and ISOCAM (S-NW cut) spectral cubes. A comparative study of the [C II] emission and AIB emission can provide further insights into the origin of the [C II] emission and the morphology of

the gas associated with the PDR. The modelling of the [C II] emission and its connection with the energetics of the PDR is presented in the next chapter.

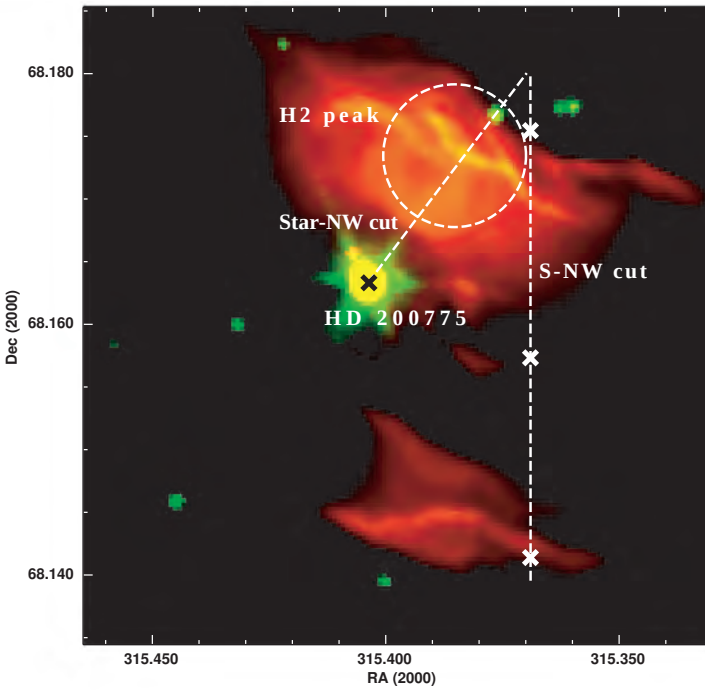

Figure 9.2: The NW and S PDRs of NGC 7023 observed by *Spitzer*-IRAC at 8 μm (red) and 3.6 μm (green). The white circle represents the HIFI beam at 535 GHz (41″) towards the H_2 peak . The dotted lines show the cuts that are studied in the [C II] emission line at 158 μm, whereas white crosses indicate the specific positions reported in Fig. 9.3 and Table 9.1. The star position is shown with a black cross.

HIFI observations and data reduction

The *Herschel* HIFI observations of NGC 7023 presented here were observed as part of the Guarantee Time Key Programme "Warm and dense interstellar medium" (WADI, P.I.: V. Ossenkompf). They consist in the on-the-fly (OTF) mapping of the [C II] 1901 GHz (158 μm) emission line using the band 7b receiver tuned in USB. The line was observed by both the wide band and the high resolution spectrometers. Two cuts were performed: a cut from the star to the NW PDR (hereafter star-NW cut) and a south-north cut (hereafter S-NW cut) covering the S PDR, the cavity and the NW PDR ($\Delta\alpha = -47'', -85 < \Delta\delta < +60''$ relative to the star position, see fig. 9.2). The pixel size after re-gridding is 6.5″ and the telescope beam size at this frequency is 11″. These observations include an OFF reference position in the western lobe of the cavity ($\Delta\alpha = -144'', \Delta\delta = -47''$). Data were reduced with HIPE 3.0 (Ott, 2010) on level-2 data produced with the standard pipeline. The [C II] WBS spectra required defringing, which was performed with

Table 9.1: Summary of the HIFI data

Transition	ν_{line} [GHz]	Position	Beam size [″]	v_{lsr} [km s^{-1}]	FWHM † [km s^{-1}]	T_A^* [K]	Area [K km s^{-1}]
HCO^+ (6−5)	535.062	H_2 peak	41	2.3 ± 0.3	1.4 ± 0.3	0.22	0.33 ± 0.07
^{13}CO (5−4)	550.926	H_2 peak	41	2.2 ± 0.3	1.2 ± 0.3	5.12	6.5 ± 1.5
^{13}CO (8−7)	881.272	H_2 peak	24	2.2 ± 0.2	0.9 ± 0.2	4.15	4.0 ± 0.8
$C^{18}O$ (5−4)	548.831	H_2 peak	41	2.1 ± 0.3	0.9 ± 0.3	1.12	1.1 ± 0.4
[C II]	1900.537	H_2 peak	11	2.7 ± 0.1	3.4 ± 0.2	23.6	85.6 ± 5.0
[C II]	1900.537	S-NW cut-N	11	2.5 ± 0.1	2.4 ± 0.2	17.9	45.8 ± 3.8
[C II]	1900.537	S-NW cut-Cav	11	4.0 ± 0.1	2.2 ± 0.2	6.89	16.2 ± 1.4
[C II]	1900.537	S-NW cut-S	11	2.5 ± 0.1	2.4 ± 0.2	13.3	34.0 ± 2.8

† For [C II], we report the FWHM of the Gaussian profile of equivalent area and peak intensity.

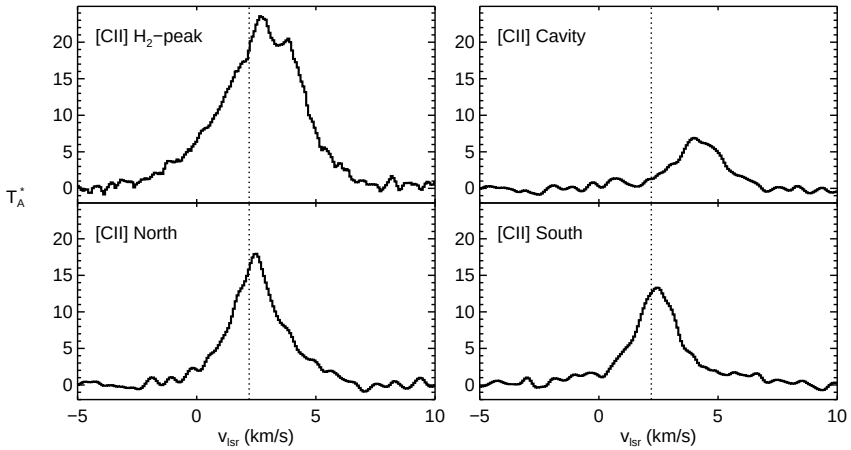

Figure 9.3: Examples of C II emission profiles at the H_2 peak and at the three positions shown by crosses on Fig. 9.2: north ($\Delta\alpha = -47''$, $\Delta\delta = +45''$), cavity ($\Delta\alpha = -47''$, $\Delta\delta = -20''$), and south ($\Delta\alpha = -47''$, $\Delta\delta = -80''$), with offsets relative to the star position. Vertical dotted line indicates $v_{lsr} = 2.2\,\mathrm{km\,s^{-1}}$.

standard HIPE tasks. The best data quality was produced with the subtraction of two sinusoidal fringes. To verify the biases introduced by the fringe removal, we compared the defringed WBS and HRS profiles (smoothed at the same spectral resolution), which showed good agreement both in profile and absolute intensity, except for the weakest lines ($T_a^* \lesssim 4\,\mathrm{K}$). Figure 9.3 shows some examples of the [C II] emission extracted at different positions along the S-NW cut and the H_2 peak. The typical noise level is $\sim 1\,\mathrm{K}$ in T_{mb} after smoothing the data to a $0.7\,\mathrm{km\,s^{-1}}$ spectral resolution.

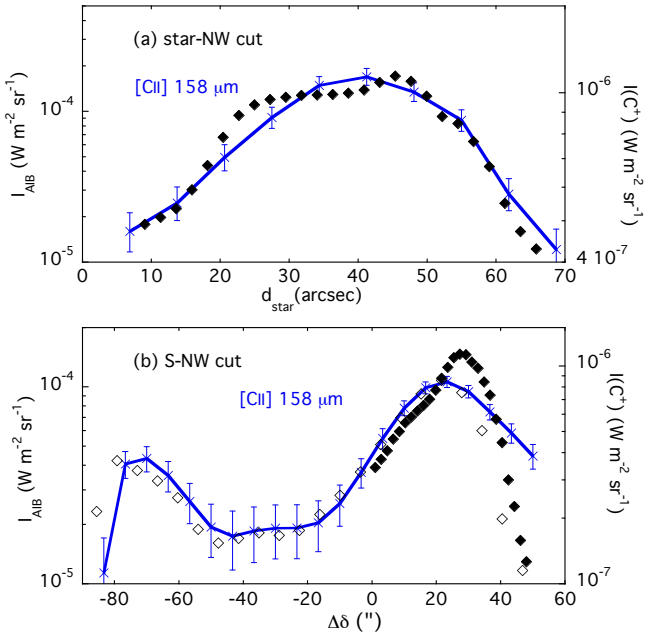

Figure 9.4: Comparison between the [C II] 158 μm line flux (solid line) measured with HIFI at a beam size of 11″ and the aromatic IR band (AIB) flux (5.5-14 μm) along the star-NW (a) and S-NW (b) cuts. The error bars for [C II] are computed at one-sigma level. The AIB flux is determined with a fit of the mid-IR spectra using the three PAH-related populations shown in Fig.10.1; filled diamonds are *Spitzer* data (1.8″ pix^{-1}), and open diamonds are ISOCAM data (6″ pix^{-1}).

Comparison with the AIB emission

Figure 9.4 displays the AIB flux, I_{AIB}, obtained by summing the fluxes of the PAH^0, PAH$^+$, and eVSG components that were derived from the fitting procedure presented in Chap. 5. It shows that the AIB intensity correlates well with the [C II] line intensity, strongly supporting that both emissions arise from the same regions. The fit of the mid-IR emission provides two independent tracers of the total gas column density N(H) along the line of sight as explained below.

1. Owing to the excitation mechanism, the AIB intensity can be considered to be proportional to the exciting UV flux, G_0, and the column density of the emitting material. Assuming that $N^C_{AIB}/N(H)$ stays constant at the PDR surface, I_{AIB} can therefore be used as a tracer of $N(H)$ if G_0 is known.

2. If the column density $N(H)$ is high enough, the effect of extinction by silicates can be seen on the AIB spectrum. We derived the column density of gas associated with the PDR by applying directly to the mid-IR spectral cubes the fitting procedure explained in Chap. 5 that includes the extinction.

Method 2 is precise for column densities higher than $N(H) \sim 10^{22}\,\mathrm{cm}^{-2}$. Method 1 can probe lower column densities but suffers from two limitations. The AIB emission needs to be corrected for the variation in the UV field G_0 to retrieve the value of N(H). This was done assuming that G_0 scales as the inverse squared distance to the illuminating star HD 200775 and a value of $G_0 = 2600$ at 42″ from this star, as derived in Chap. 6. We used the projected distance as an estimate of the true distance. This introduces an error that can be especially strong at positions close to the star in the plane of the sky. Figure 9.4 shows that the AIB emission stays almost constant at $d < 16''$ in the star-NW cut, therefore we used this value as the minimum effective distance of the NW PDR to the star. Method 1 also needs to be calibrated since the local emissivity of the AIB carriers is not known precisely. Our approach was therefore to derive a calibration factor using the values obtained by method 2 at a distance of $\sim 42''$ on the star-NW cut. The same calibration factor was used for all positions along the two cuts. A finer approach would consist in the description of these regions with a geometrical model, similarly to what has been done in Chap. 6 for the interior of the PDR.

Figure 9.5 shows that the column densities that were derived on the two cuts correlate quite well with the [C II] line intensity.

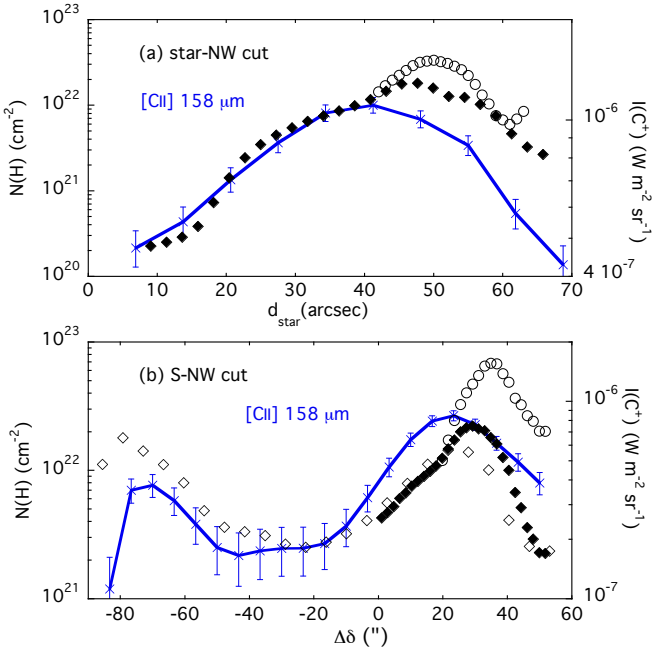

Figure 9.5: Comparison between the [C II] 158 μm line flux (solid line) measured with HIFI at a beam size of 11″ and the column density N(H) along the star-NW (a) and S-NW (b) cuts. N(H) was derived from both the AIB flux (diamonds) and the mid-IR dust extinction (open circles); filled diamonds and open circles are *Spitzer* data (1.8″ pix^{-1}), and open diamonds are ISOCAM data (6″ pix^{-1}).

A higher density filament is clearly observed around position 50″ on the star-NW cut. Attenuation of the mid-IR emission is observed here over a physical size of few

arcsecs, that is small compared to the full size of the filament (∼ 9.5″ at half maximum obtained in extinction with method 2, cf. Sec. 9.3).

Finally, it is interesting to note that the S-NW cut, that has been observed in [C II], is going through a denser or more extended structure. It corresponds indeed to a clump that is well observed in CS (see section 9.4).

9.3 HCO+ EMISSION AND THE HIGH-DENSITY FILAMENTS

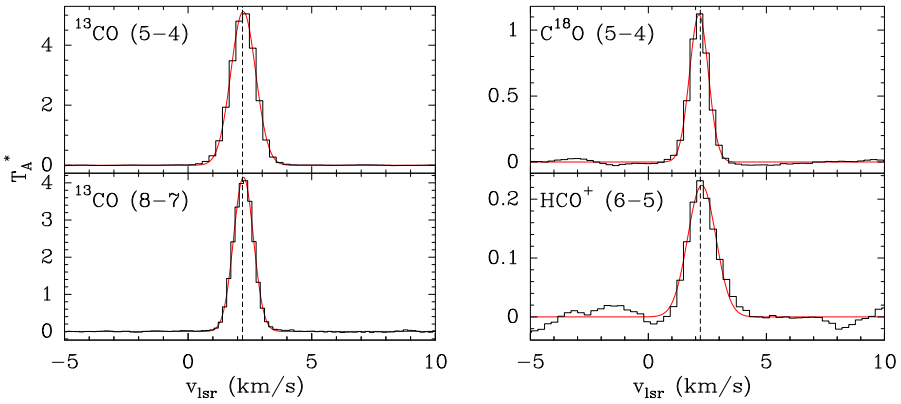

Figure 9.6: ^{13}CO, $C^{18}O$, and HCO^+ high-J transitions observed with HIFI toward the H_2 peak.The vertical dotted line indicates $v_{lsr} = 2.2$ km s^{-1}.

Interferometric observations obtained at the Plateau de Bure Interferometer (PdBI) in HCO^+ (Fuente *et al.*, 1996) and other tracers with high dipole moments such as CS, HCN, and CN show the presence of high-density filaments in NGC 7023 NW, with hydrogen densities of $n_H \sim 10^5 - 10^6$ cm^{-3}. However, the observations at mm wavelengths can probe only low-J transitions of these molecules. The high-J emission lines, that arise from gas at high temperature and density, are accessible with *Herschel* and can be used to further constrain the physical parameters towards these filaments. Here, we compare the HCO^+ (6→5) emission observed with HIFI and lower J transitions from previous ground-based observations.

HCO^+ was observed with HIFI at the H_2 peak position (see Fig. 9.2) towards the NW PDR in bands 1a and 3b. We used the frequency-switch observing mode, with a frequency throw of ∼ 0.9 MHz. In band 1a, the frequency ranges covered by the WBS were [535-539] GHz (LSB) and [547-551] GHz (USB). In band 3b, covered ranges were [879-883] GHz (LSB) and [891-895] GHz (USB). The observed position ($\Delta\alpha$ = −25″, $\Delta\delta$ = +38″, called H_2 peak) corresponds to the peak intensity of the H_2 rovibrational emission associated to the near-IR filaments (Lemaire *et al.*, 1996). The OFF positions was the same that has been used for [C II] observations. Manual steps in the

data reduction were performed in HIPE 3.0, and consisted in the stitching of sub-bands, baseline removal, and correction for main beam efficiency ($\eta_{mb} = 0.71$).

Fuente *et al.* (1996) have shown that the thickness of the high density filaments as traced by the HCO^+ 1→0 line observed at the PdBI is about 6″. Assuming that the (6→5) line arises from the same region, we estimate a dilution factor of 5.4 in the HIFI beam of 41″. Fuente *et al.* (1993) reported the observations of HCO^+ (3→2) with the IRAM 30m telescope towards a close-by position. The beam of the 30m telescope at this frequencies (8″) is comparable to the thickness of the filaments, so that dilution effects should be negligible.

Using RADEX (van der Tak *et al.*, 2007), we reproduced the brightness temperature of the interferometric HCO^+ (1→0), single dish (3→2) and *Herschel* (6→5) transitions. The observed brightness temperatures can be reproduced within 20% assuming a column density of $N(HCO^+) = 3.5 \times 10^{13}\,cm^{-2}$, a kinetic temperature of 95 K and a density of $n_H = 2 \times 10^5\,cm^{-3}$. Considering the uncertainty on dilution factors, calibration and pointing accuracy, this level of accuracy is very good.

Assuming that high-J lines of ^{13}CO and $C^{18}O$ arise from the same region, we can estimate a dilution factor in HIFI beam of 5.4 and 1.5 for the (5→4) and (8→7) lines, respectively. The observed brightness temperatures for these CO isotopes are also consistent with the estimates of density and temperature obtained from HCO^+ data at the same level of uncertainty as for the HCO^+ estimates.

9.4 The clump

One of the results of the fitting procedure described in Chap. 5 is the column density of the gas associated with the PDR. Figure 9.7 shows the effect of the extinction correction in the fit of the AIB spectrum extracted towards the clump position. Assuming a distance of 430 pc, the angular extend of the clump (FWHM ∼ 14″) translate into a physical length of 8×10^{16} cm (0.025 pc) for the width at half maximum. Using the column density of $N(H) = 7.2 \times 10^{22}\,cm^{-2}$ derived at the peak (see also fig. 9.5) we can estimate a density in the clump of $n(H_2) = 4.5 \times 10^5\,cm^{-3}$.

The NW PDR of NGC 7023 was observed in April-November 1997 with the IRAM 5-element array at Plateau de Bure (France) in its CD configuration (A. Fuente, private communication). The observations consist in a 5-field mosaic covering an almost circular region of ∼ 100″ in diameter. Receivers were tuned double side band to observe at the same time the CS(2→1) transition at 97.98 GHz (with a beam FWHM of ∼ 3″) and the CS(5→4) transition at 244.935 GHz (FWHM ∼ 1.5″). The CS lines peak at a $v_{lsr} \sim 2.4\,km\,s^{-1}$, with a second peak at $\sim 1.8\,km\,s^{-1}$.

Figure 9.8 shows the correlation of the column density derived with the mid-IR fit and the integrated intensity of CS emission in the $1.8 - 2.8\,km\,s^{-1}$ range. This spatial correlation is striking: CS (2 → 1) emission arises from the same region where the IR emission is absorbed, further supporting the evidence of a high density region (hereafter *the clump*) associated with the PDR.

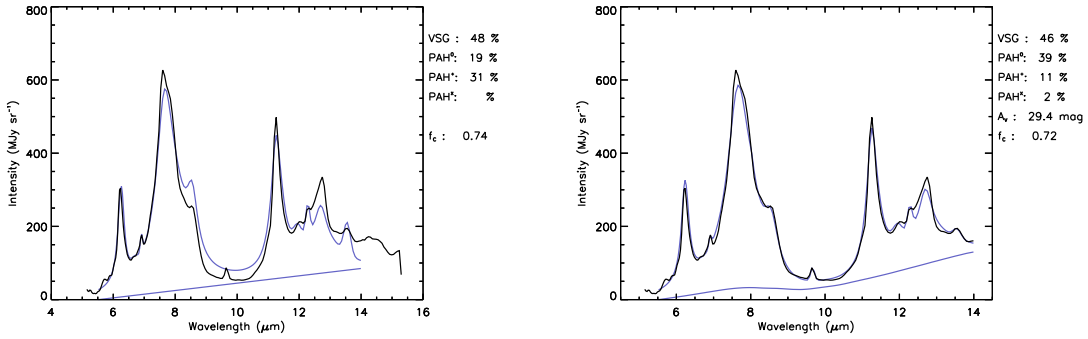

Figure 9.7: Fit of the mid-IR emission spectrum from the clump position without the extinction correction (left) and with the fully mixed correction (right).

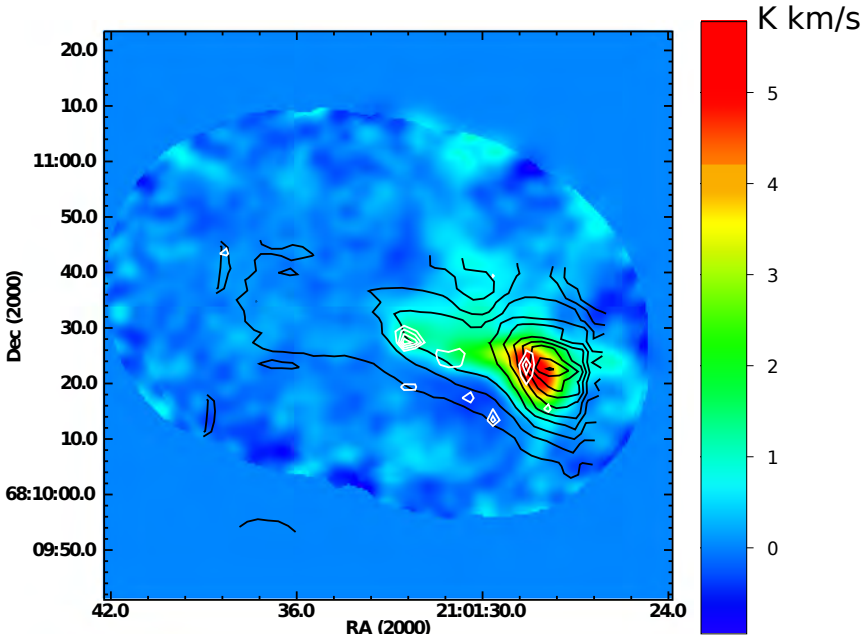

Figure 9.8: Comparison between the integrated CS (2 → 1) emission (colour scale) and the extinction A_V derived from the mid-IR fit (black contours, steps of 5 mag). White contours represent the tentative CS (5→4) detection (levels from 1 to 5 km s^{-1} in steps of 1 km s^{-1}.)

This result provides strong evidence that the clump is placed in front of the PDR, producing a shadow in the AIB emission. To illustrate this effect, we show in figure 9.9 three stripes along the star-PDR axis. For each of the stripes, we report a profile of the IRAC 8 μm and CS (2→1) emission and the hydrogen column density obtained with the mid-IR fit. In stripe (1), which is passing through the clump, the 8 μm emission profile decrease abruptly and present a hole in correspondence with the maximum of CS emission and A_V. In stripe (2) such decrease has a smoother profile. Stripe (3), which does not present CS emission or mid-IR absorption, shows a very smooth decrease in

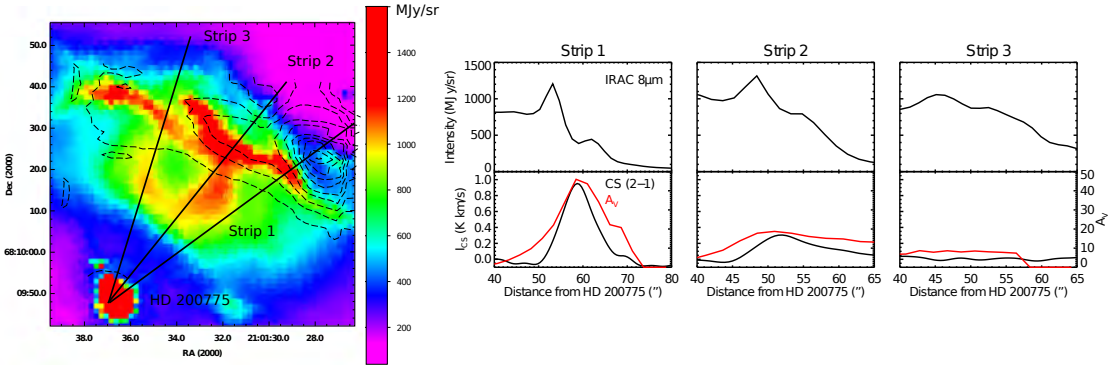

Figure 9.9: *Left:* IRAC 8 μm emission (colour scale) of the north-west PDR of NGC 7023. Contours represent the magnitudes of visual extinction derived from the analysis of the IRS spectral cubes, in steps of 5 A_V. *Right:* The stripes indicated in the left panel, reporting the IRAC 8 μm emission (up), the A_V and the CS (2→1) emission observed at the PDBI (down). Strip 1 pass through the clump, which is characterised by the high A_V and the intense CS emission. This correspond spatially to a abrupt decrease in the PAH emission traced by the IRAC 8 μm emission. Strip 3 passes in a region with no extinction, and the decrease in the PAH emission is quite smooth. Strip 2 is an intermediate case.

the IRAC 8 μm emission.

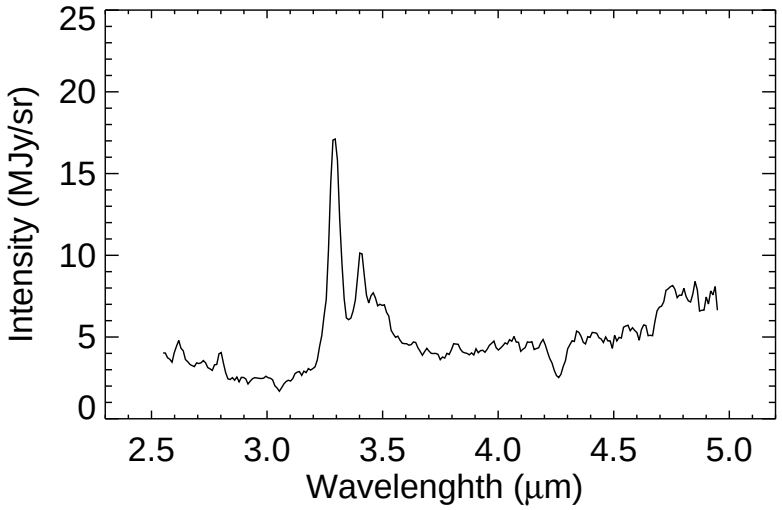

Figure 9.10: AKARI-IRC near-IR spectrum towards the clump position, showing the absorption of CO_2 ices.

Finally,Fig. 9.10 shows the AKARI-IRC spectrum between 2.5-5 μm extracted at the clump position. This spectrum presents several interesting features, apart from the 3.3 and 3.4 μm complex. In particular, broad absorption bands are present at 4.27 and 3.04 μm, which correspond respectively to the CO stretching mode in CO_2 ices and to the OH stretching mode in H_2O ices (Gerakines *et al.*, 1995). The CO_2 ice presents

another feature in the mid-IR, but it has a lower absorption strength and is blended with PAH features, which make it difficult to observe in PDR spectra. Using the laboratory absorption coefficients of Gerakines *et al.* (1995) and the column density derived from the mid-IR fit, we can estimate an abundance compared to H of $\sim 5 \times 10^{-6}$ for CO_2 and $\sim 4 \times 10^{-6}$ for H_2O. The abundance of CO_2 relative to H_2O is much lower ($\sim 10 - 20\%$) in star-forming regions and dark molecular clouds (Gerakines *et al.*, 1999; Nummelin *et al.*, 2001; Bergin *et al.*, 2005). However, this ratio is highly variable and the abundance of solid CO_2 has been measured to be ~ 45 compared to H_2O in the Large Magellanic Cloud (Shimonishi *et al.*, 2008). Interestingly, *Herschel* observations in the WADI key program have revealed that in PDRs the abundance of gas-phase H_2O is usually less than that predicted by models. These observations show that there is still more work to do to characterise the gas-grain interactions.

Chapter

10

The energetics and dynamics of NGC 7023

10.1 Very small dust particles, [C II] emission and the cooling of PDRs

The contribution of small dust particles to the photo-electric heating of PDRs depends on the size and charge state of the grain. Current models use empirical grain size distributions that enable to predict the contribution of PAHs and VSGs to the gas heating. These models need to be compared with observations. As mentioned in Chap. 3, one way to proceed is to measure the photo-electric efficiency, defined as the ratio between the energies emitted in the main PDR cooling lines and in the far-IR continuum. At the edges of PDRs, the main cooling lines are the [C II] and [O I] lines. The recent *Herschel* mission is now providing observations of these lines at high spatial and spectral resolution. The comparison of these lines with PAH observations allows a quantitative study on the role of PAHs in the thermal balance of PDRs. At this time, only [C II] observations has been performed towards NGC 7023, while PACS observations of the [O I] lines are still pending. Nevertheless, a preliminary comparison between [C II] emission and the different PAH populations can be performed.

[C II] modelling

The critical density for the [C II] 158 μm line is n_{crit}=2500 cm^{-3} for collisions with H and the line emissivity depends mainly on temperature for $n > n_{crit}$. We selected a few positions on the HIFI S-NW [C II] cut, three points on the NW PDR and two on the South PDR (cf. Table 10.1). The values of G_0 were determined as explained in Chap. 9, and we assumed a constant average density with two different values: $n_H = 2\times10^4$ cm^{-3} that is characteristic of the molecular cloud (Gerin *et al.*, 1998) and $n_H = 7\times10^3$ cm^{-3} that was derived by Rapacioli *et al.* (2006) in their study of PAH-related species.

We used the 1D Meudon PDR code (Le Petit *et al.*, 2006) to compute the gas temperature T at the cloud surface for all the selected positions (cf. Table 10.1). Assuming a two-level system, the values of T can be used to calculate the C^+ level populations n_1 and n_0:

$$\frac{n_1}{n_0} = \frac{g_1}{g_0} exp\left(-\frac{E_{01}}{kT}\right) \frac{1}{1+\frac{A_{10}}{\gamma_{10} n_H}} \tag{10.1}$$

where $g_1/g_0 = 2$ is the ratio of the statistical weights of the two levels involved, E_{01} is the energy separation between the two levels, k is the Boltzmann constant, $A_{10} = 2.29\times10^{-6}$ s^{-1} is the Einstein coefficient for spontaneous emission and $\gamma_{10} = 8.86\times10^{-10}$ cm^{-3} s^{-1} is the collisional coefficient for C^+ with H.

Line intensities are then derived by integrating along the line-of-sight (perpendicular to model results) and by assuming uniform excitation conditions. The thickness of the observed regions can lead to optical depths $\tau \sim 1$, which implies that radiative transfer effects must be taken into account. If we assume constant excitation conditions and gas properties along the line of sight, then τ can be computed analytically:

$$\tau = \left(\frac{g_1}{g_0} n_0 - n_1\right) \frac{c^2}{8\pi\Delta\nu_D \nu_0^2} A_{10} \frac{N_H}{n_H} \tag{10.2}$$

where $\Delta\nu_D$ is the Doppler width of the line and $\nu_0 = 1900.5369$ GHz is the central frequency of the line and we use the results of the previous chapter for the column density N_H. Once τ is known, we can compute also the intensity of the line using

$$I = \frac{2h\nu^3}{c^2} \frac{1-\exp(-\tau)}{\frac{g_1}{g_0}\frac{n_0}{n_1} - 1} \Delta\nu_D. \tag{10.3}$$

We calculated the expected line intensity for five positions along the S-NW cut for both $n_H = 7\times10^3$ cm^{-3} and $n_H = 2\times10^4$ cm^{-3}. The results are reported in Table 10.1.

The agreement between calculated and observed flux values is very good when using $n_H = 7\times10^3$cm^{-3}. In the NW PDR, the ratio is 1.0 for NW3 (16) and NW2 (12), and 1.4 for NW1 (-3). For the S PDR, a value of 2.3 is derived for the two positions, suggesting that systematic effects are causing the deviation between observed and calculated values of the [C II] flux. There are several parameters that are not precise in our model but looking at Table 10.1, it seems the local [C II] emissivity is mainly affected by the local

density and not by the value of G_0. For N(H), we assumed the same regions emit in PAHs and [C II], in agreement with the profiles shown in Fig. 9.4. Another source of error is the use of a temperature calculated at the surface rather than in the region emitting [C II] emission. There is also an error for N(H) due to our method (cf. Chap. 5), but this error is expected to be the same for both PDRs. Dividing N(H) by a factor of two leads to lower values of the ratio of the calculated over the observed [C II] flux: 0.7-0.8 for the NW PDR and 1.6-1.7 for the S PDR.

One step further in the model would consist in studying the effect of the grain charge on the photoelectric efficiency (Bakes and Tielens, 1994). The relative abundances of PAH^+, PAH^0, and evaporating VSGs vary significantly over the nebula (Fig. 10.1). Regions in the cavity appear mainly populated by PAH^+ (cf. NW1 (-3) in Table 10.1). Since the ionisation potential of PAH^+ is much higher than that of PAH^0 ($\sim$10 eV compared to $\sim$6 eV; Malloci *et al.* 2007), PAH^+ should contribute less to the photoelectric heating than PAH^0, leading to a decrease in the heating rate, hence in the gas cooling. In its current version, the PDR code uses classical grains with an MRN distribution (Mathis *et al.*, 1977) and absorption and scattering cross-sections from Laor and Draine (1993). We have used grains of sizes from 15 Å to 3000 Å with a dust-to-gas mass ratio of 1%. As a result, the ionisation parameter γ that quantifies the grain charge (cf. Table 10.1) does not reflect well the variations of the PAH charge observed in Fig. 10.1. An upgraded version, in which the PDR code is coupled to the code DUSTEM (Compiègne *et al.*, 2010), is under development (Gonzalez et al, in preparation) and will allow the inclusion of PAHs and a description of their charge variation. NGC 7023 is clearly a template region that could be used for these studies.

Table 10.1: Summary of the PDR modelling of the [C II] emission for 5 points along the HIFI S-NW cut ($\Delta\alpha = -47''$)

Pos. ($\Delta\delta$)	d_{proj}	UV field	T	PAH^+/PAH^0	Ionisation	$N(H)$	[C II] local	[C II] flux	
		(a)	***(b)***	***(c)***	parameter (γ) ***(b)***	***(d)***	emissivity ***(b)***	HIFI	Model ***(b)***
($''$)	($''$)	(G_0)	(K)		(10^3 G_0 $K^{1/2}$ cm^3)	(10^{21} cm^{-2})	(10^{-21}W m^{-3})	(10^{-7}W m^{-2} sr^{-1})	
NW3 (16)	50	1873	337 / 333	1.9	11.0 / 29.5	10.5	4.4 / 1.4	8.0	11.0 / 8.0
NW2 (12)	48	1975	342 / 333	2.7	11.7 / 31.1	8.1	4.4 / 1.4	6.9	9.5 / 7.1
NW1 (-3)	47	2100	348 / 333	9.6	12.6 / 33.0	3.9	4.4 / 1.4	3.3	5.6 / 4.6
S1 (-63)	79	747	248 / 320	1.7	3.8 / 11.8	8.7	4.2 / 1.4	3.1	8.3 / 7.2
S2 (-73)	87	607	230 / 312	0.96	3.0 / 9.5	14.0	4.1 / 1.4	3.7	9.6 / 8.4

(a) Calculated using a projected distance and G_0=2600 at 42 $''$ from the star.
(b) From the PDR model using $n_H = 2 \times 10^4 / 7 \times 10^3$ cm^{-3}, respectively.
(c) Given as the ratio of the mid-IR intensities shown in Fig. 10.1.
(d) Derived from the analysis of the mid-IR emission spectra.

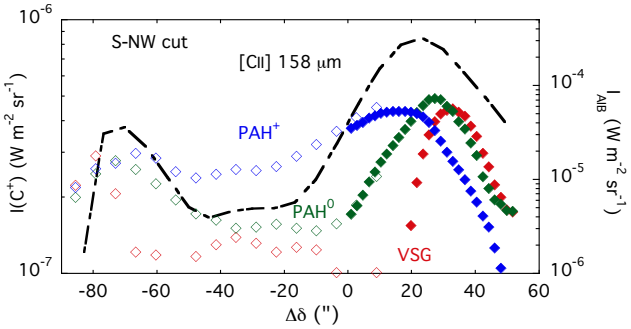

Figure 10.1: S-NW cut in [C II] emission measured with HIFI at a beam size of 11″ (dot-dashed line) and distribution of the emission from the different very small dust populations, PAH^+ (blue), PAH^0 (green) and evaporating VSGs (red); filled diamonds are *Spitzer* data (1.8 ″ pix^{-1}) and open diamonds are ISOCAM data (6″ pix^{-1}).

10.2 Perspective in the study of PDR dynamics

Figure 9.6 shows the ^{13}CO 5–4, ^{13}CO 8–7, $C^{18}O$ 5–4, and HCO^+ 6–5 lines observed by HIFI towards the H_2 peak. All the lines have a central velocity of about 2.2 km s^{-1}, comparable to previous ground-based observations in several molecular lines (Fuente *et al.*, 1993). Figure 9.3 shows the [C II] line profiles at the H_2 peak and at different positions along the S-NW cut. The line is much broader than molecular lines and its profile shows a complex multi-component structure. Its emission peaks at intermediate velocities (v_{lsr} ∼1.8-2.8 km s^{-1}) towards the PDRs, but there is also a contribution from higher velocity components (v_{lsr} ∼4 km s^{-1}), which dominate the emission in the cavity.

The position-velocity diagrams (Fig. 10.2) for the [C II] line at the very high spectral resolution of HIFI provides evidence for an evaporating flow of gas at $v_{lsr} = 4$ km s^{-1} (or ∼ 1.8 km s^{-1} relative to the quiescent gas velocity). This line appears then as a very good tracer of physical conditions in evaporating flows associated with dense molecular structures in PDRs. The interpretation of the gas kinematics in NGC 7023 is difficult. Even though the position velocity diagrams support the evaporating scenario, there can be other explanations. The gas at 4 km s^{-1} observed in the cavity could be also due to the expansion of the cavity, as hinted by the velocity structure detected in H I emission in the cavity (Fuente *et al.*, 1998), and/or a shock associated with the photodissociation front. The comparative study of the [C II] line profile in the different sources observed in the WADI consortium will provide further insights on this issue. The analysis of the CO band profiles can also constrain the physics of these processes.

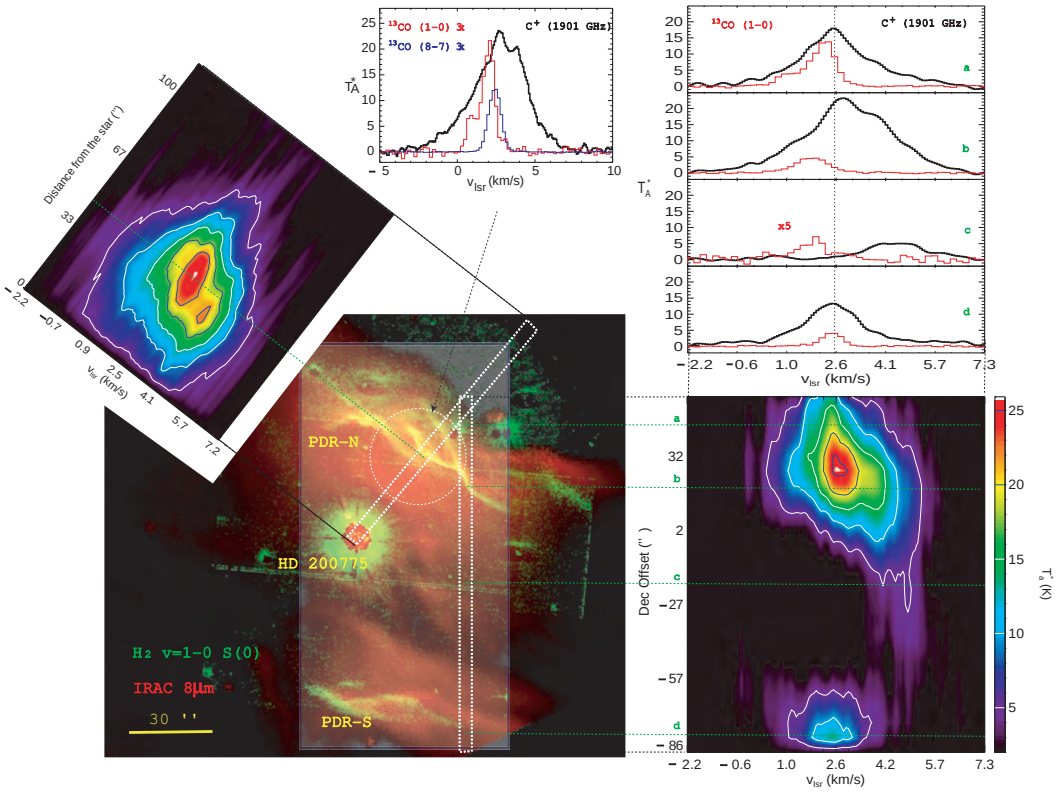

Figure 10.2: In the main image, the North and South PDRs of NGC 7023 and the illuminating star HD 200775: in red, the PAH emission observed with the Spitzer IRAC 8μm filter, and in green the vibrationally excited H_2 emission tracing the filaments (from Lemaire *et al.*, 1996). The white dotted lines represent the two C^+ stripes observed with HIFI, for which we report also the position-velocity maps. On the upper right, the C^+ and ^{13}CO (1→0) spectra at four positions on the vertical cut (green labels). Finally, the white circle represent the H_2 peak position, for which we show the C^+ and ^{13}CO (8→7) spectra observed with HIFI and ^{13}CO (1→0) observed with the IRAM 30m telescope.

A&A 521, L25 (2010)
DOI: 10.1051/0004-6361/201015129

Astronomy & Astrophysics
Special feature

Herschel/HIFI: first science highlights

LETTER TO THE EDITOR

Gas morphology and energetics at the surface of PDRs: New insights with *Herschel* observations of NGC 7023⋆

C. Joblin[1,2], P. Pilleri[1,2], J. Montillaud[1,2], A. Fuente[3], M. Gerin[4], O. Berné[5], V. Ossenkopf[6,7], J. Le Bourlot[8], D. Teyssier[9], J. R. Goicoechea[10], F. Le Petit[8], M. Röllig[6], M. Akyilmaz[6], A. O. Benz[11], F. Boulanger[12], S. Bruderer[11], C. Dedes[11], K. France[13], R. Güsten[14], A. Harris[15], T. Klein[14], C. Kramer[16], S. D. Lord[17], P. G. Martin[13], J. Martin-Pintado[10], B. Mookerjea[18], Y. Okada[6], T. G. Phillips[19], J.R. Rizzo[10], R. Simon[6], J. Stutzki[6], F. van der Tak[7,20], H. W. Yorke[21], E. Steinmetz[22], C. Jarchow[22], P. Hartogh[22], C. E. Honingh[6], O. Siebertz[6], E. Caux[1,2], and B. Colin[17]

(Affiliations are available on page 5 of the online edition)

Received 1 June 2010 / Accepted 19 July 2010

ABSTRACT

Context. We investigate the physics and chemistry of the gas and dust in dense photon-dominated regions (PDRs), along with their dependence on the illuminating UV field.
Aims. Using *Herschel*/HIFI observations, we study the gas energetics in NGC 7023 in relation to the morphology of this nebula. NGC 7023 is the prototype of a PDR illuminated by a B2V star and is one of the key targets of *Herschel*.
Methods. Our approach consists in determining the energetics of the region by combining the information carried by the mid-IR spectrum (extinction by classical grains, emission from very small dust particles) with that of the main gas coolant lines. In this letter, we discuss more specifically the intensity and line profile of the 158 μm (1901 GHz) [C II] line measured by HIFI and provide information on the emitting gas.
Results. We show that both the [C II] emission and the mid-IR emission from polycyclic aromatic hydrocarbons (PAHs) arise from the regions located in the transition zone between atomic and molecular gas. Using the Meudon PDR code and a simple transfer model, we find good agreement between the calculated and observed [C II] intensities.
Conclusions. HIFI observations of NGC 7023 provide the opportunity to constrain the energetics at the surface of PDRs. Future work will include analysis of the main coolant line [O I] and use of a new PDR model that includes PAH-related species.

Key words. ISM: structure – ISM: kinematics and dynamics – ISM: molecules – submillimeter: ISM

1. Introduction

One main goal of the guarantee time key programme "Warm and dense interstellar medium" (WADI) of the HIFI heterodyne spectrometer (de Graauw et al. 2010) onboard *Herschel* (Pilbratt et al. 2010) is to investigate the physics and chemistry of the gas and dust in dense photon-dominated regions (PDRs), as well as their dependence on the illuminating UV field. As part of this programme, we observed a prototype PDR, NGC 7023. The region is illuminated by the B2Ve HD 200775 [RA(2000) = 21h01m36.9s ; Dec(2000) = +68°09′47.8″], and has been shaped by the star formation process leading to the formation of a cavity. NGC 7023 has been widely studied at many wavelengths. It has been shown that this region hosts structures at different gas densities: $n_{\rm H} \sim 100\,{\rm cm}^{-3}$ in the cavity, $\sim 10^4\,{\rm cm}^{-3}$ in the PDRs that are located north-west (NW), south (S) and east, and 10^5–$10^6\,{\rm cm}^{-3}$ in dense filaments and clumps that are observed in the mm (Fuente et al. 1996; Gerin et al. 1998 and references therein) and near-IR (Lemaire et al. 1996; Martini et al. 1997).

NGC 7023 has been mapped by the instruments PACS and SPIRE of *Herschel* to study the emission of large cold grains (Abergel et al. 2010). We present here some observations of the gas at the surface of this nebula, taking advantage of the very high spectral resolution of HIFI. By combining these observations with previous mid-IR observations, we study the geometry and energetics of the NW and S PDRs.

2. Observations and results

2.1. HIFI observations

The HIFI observations presented here consist in (offset positions are relative to the star; see Fig. 1):

- single pointing using frequency switch mode towards the NW PDR in bands 1a and 3b. In band 1a, the frequency ranges covered by the wide band spectrometer (WBS) were [535–539] GHz (LSB) and [547–551] GHz (USB). In band 3b, covered ranges were [879–883] GHz (LSB) and [891–895] GHz (USB). The observed position ($\Delta\alpha$ = −25″, $\Delta\delta$ = +38″, called H_2 peak) corresponds to the peak intensity of the H_2 ro-vibrational emission associated to the near-IR filaments (Lemaire et al. 1996);
- on-the-fly (OTF) mapping of the [C II] 1901 GHz emission line in band 7b. The line was covered by both the WBS and the high-resolution spectrometer (HRS) in USB. Two cuts

⋆ *Herschel* is an ESA space observatory with science instruments provided by European-led Principal Investigator consortia and with important participation from NASA.

A&A 521, L25 (2010)

Table 1. Summary of the HIFI data.

Transition	$\nu_{\rm line}$ [GHz]	Position	Beam size [″]	$v_{\rm lsr}$ [km s^{-1}]	*FWHM*† [km s^{-1}]	$T_{\rm A}^{*}$ [K]	Area [K km s^{-1}]
HCO^+ (6–5)	535.062	H_2 peak	41	2.3 ± 0.3	1.4 ± 0.3	0.22	0.33 ± 0.07
^{13}CO (5–4)	550.926	H_2 peak	41	2.2 ± 0.3	1.2 ± 0.3	5.12	6.5 ± 1.5
^{13}CO (8–7)	881.272	H_2 peak	24	2.2 ± 0.2	0.9 ± 0.2	4.15	4.0 ± 0.8
$C^{18}O$ (5–4)	548.831	H_2 peak	41	2.1 ± 0.3	0.9 ± 0.3	1.12	1.1 ± 0.4
[C II]	1900.537	H_2 peak	11	2.7 ± 0.1	3.4 ± 0.2	23.6	85.6 ± 5.0
[C II]	1900.537	S-NW cut / North	11	2.5 ± 0.1	2.4 ± 0.2	17.9	45.8 ± 3.8
[C II]	1900.537	S-NW cut / Cavity	11	4.0 ± 0.1	2.2 ± 0.2	6.89	16.2 ± 1.4
[C II]	1900.537	S-NW cut / South	11	2.5 ± 0.1	2.4 ± 0.2	13.3	34.0 ± 2.8

Notes. $^{(\dagger)}$ For [C II] , we report the *FWHM* of the Gaussian profile of equivalent area and peak intensity.

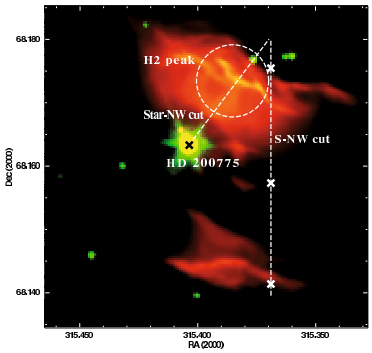

Fig. 1. The NW and S PDRs of NGC 7023 observed by *Spitzer*-IRAC at 8 μm (red) and 3.6 μm (green). The white circle represents the HIFI beam at 535 GHz (41″) towards the H_2 peak. The dotted lines show the cuts that are studied in the [C II] emission line at 158 μm with a beam of 11″, whereas white crosses indicate the specific positions reported in Fig. 2 and Table 1. The star position is shown with a black cross.

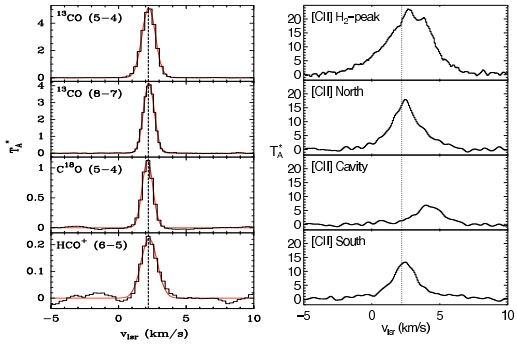

Fig. 2. *Left*: ^{13}CO, $C^{18}O$, and HCO^+ high-*J* transitions observed with HIFI toward the H_2 peak. *Right*: examples of [C II] emission profiles at the H_2 peak and at the three positions shown by crosses on Fig. 1: north ($\Delta\alpha = -47''$, $\Delta\delta = +45''$), cavity ($\Delta\alpha = -47''$, $\Delta\delta = -20''$), and south ($\Delta\alpha = -47''$, $\Delta\delta = -80''$), with offsets relative to the star position. In both figures, the vertical dotted line indicates $v_{\rm lsr} = 2.2$ km s^{-1}.

were performed: a cut from the star to the NW PDR (star-NW cut) and a south-north cut (hereafter S-NW cut) covering the NW PDR, the cavity and the S PDR ($\Delta\alpha = -47''$, $-85 < \Delta\delta < +60''$, see Fig. 1). The pixel size after regriding is 6.5″.

All these observations include an OFF reference position in the western lobe of the cavity ($\Delta\alpha = -144''$, $\Delta\delta = -47''$). Data was reduced with HIPE 3.0 (Ott 2010) on level-2 data produced with the standard pipeline. For the pointed observations in bands 1a and 3b, manual steps consisted in stitching sub-bands, baseline removal, and correction for main beam efficiency ($\eta_{\rm mb} = 0.71$). The [C II] WBS spectra required defringing, which was performed with standard HIPE tasks, and the best data quality was produced with the subtraction of two sinusoidal fringes. To verify the biases introduced by the fringe removal, we compared the WBS and HRS profiles, which showed good agreement both in profile and absolute intensity except for the weakest lines ($T_{\rm a}^{*} \lesssim 4$ K).

2.2. Gas kinematics

Figure 2 (left panel) shows the ^{13}CO 5–4, ^{13}CO 8–7, $C^{18}O$ 5–4, and HCO^+ 6–5 lines observed by HIFI towards the H_2 peak. All the lines have a central velocity of about 2.2 km s^{-1}, comparable to previous ground-based observations in several molecular lines (Fuente et al. 1993). Figure 2 (right panel) shows the [C II] line profiles at the H_2 peak and at different positions along the S-NW cut. The line is much broader than molecular lines and its profile shows a complex multi-component structure. The observations towards the PDRs show that the emission peaks at intermediate velocities ($v_{\rm lsr} \sim 1.8$–2.8 km s^{-1}), which have already been observed towards the NW PDR in several molecular tracers (see, for example, Fuente et al. 1996). There is also a contribution from higher velocity components ($v_{\rm lsr} \sim 4$ km s^{-1}), which dominate the emission in the cavity.

2.3. Emission from very small dust particles and C^+

The 158 μm (1901 GHz) [C II] and 63 μm [O I] lines are the major coolants of the gas at the surface of PDRs (Hollenbach & Tielens 1999). In these regions, photoelectric effect dominates the heating, while H_2 formation provides a minor contribution. Since the smallest dust particles, polycyclic aromatic hydrocarbons (PAHs) and very small grains (VSGs) contribute to a large fraction to this process (Bakes & Tielens 1994; Habart et al. 2001), and these particles emit in the mid-IR most of the energy they absorb in the UV, we expect that the mid-IR and [C II] emissions arise in the same regions.

We used mid-IR spectro-imagery data of the NW PDR of NGC 7023 that were obtained in the 5.5–14.5 μm range with the Infrared Spectrograph onboard *Spitzer* (Werner et al. 2004). For the S PDR, we used ISOCAM highly-processed data products (Boulanger et al. 1996) from the ISO data archive. To analyse the mid-IR spectra, we followed the method explained in Rapacioli et al. (2005) and Berné et al. (2007), in which the mid-IR emission is decomposed into three aromatic IR band

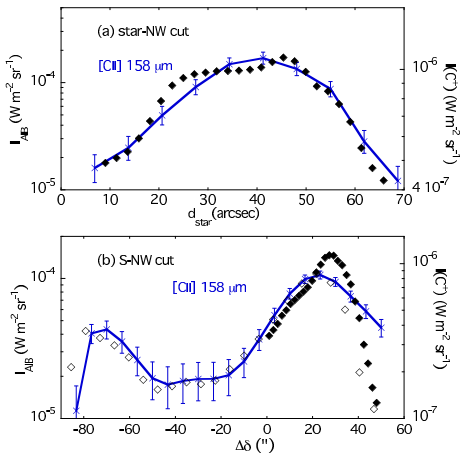

Fig. 3. Comparison between the [C II] 158 μm line flux (solid line) measured with HIFI at a beam size of 11″ and the aromatic IR band (AIB) flux (5.5-14 μm) along the star-NW **a)** and S-NW **b)** cuts. The error bars for [C II] are computed at one-sigma level. The AIB flux is determined with a fit of the mid-IR spectra using the three PAH-related populations shown in Fig. 5; filled diamonds are *Spitzer* data (1.8″ pix^{-1}), and open diamonds are ISOCAM data (6″ pix^{-1}).

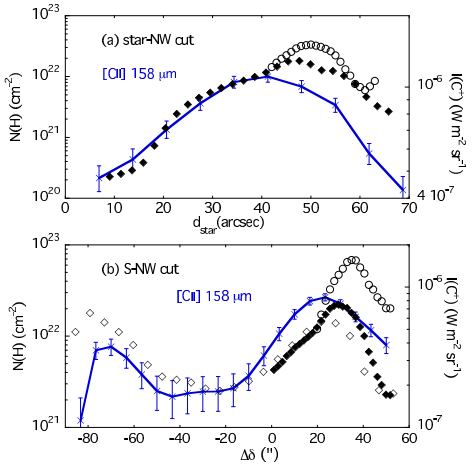

Fig. 4. Comparison between the [C II] 158 μm line flux (solid line) measured with HIFI at a beam size of 11″ and the column density N(H) along the star-NW **a)** and S-NW **b)** cuts. N(H) was derived from both the AIB flux (diamonds) and the mid-IR dust extinction (open circles); filled diamonds and open circles are *Spitzer* data (1.8″ pix^{-1}), and open diamonds are ISOCAM data (6″ pix^{-1}).

(AIB) spectra whose carriers are neutral PAHs (PAH^0), cationic PAHs (PAH$^+$), and evaporating VSGs. The fitting procedure was recently improved by including the convolution of the composite spectrum by extinction (Pilleri et al. 2010). Figure 3 displays the AIB flux, $I_{\rm AIB}$, obtained by summing the fluxes of the PAH^0, PAH$^+$, and VSG components that were derived from the fit. It shows that the AIB intensity correlates well with the [C II] line intensity, strongly suggesting that both emissions arise from the same regions. The fit of the mid-IR emission provides two independent tracers of the total gas column density N(H) along the line of sight as explained below.

(i) Owing to the excitation mechanism, the AIB intensity can be written as $I_{\rm AIB} \propto G_0 \times N^{\rm C}_{\rm AIB}$ where $N^{\rm C}_{AIB}$ is the column density of carbon in the AIB carriers and G_0 the UV flux in Habing units (Habing 1968). Assuming that $N^{\rm C}_{\rm AIB}/N$(H) stays constant at the PDR surface, $I_{\rm AIB}$ can therefore be used as a tracer of N(H) if G_0 is known (Pilleri et al. 2010).

(ii) If the column density N(H) is high enough, the effect of extinction by silicates can be seen on the AIB spectrum. In the mid-IR fit, the extinction is derived from a simple correction term, assuming that the emitting and absorbing materials are fully mixed: $\frac{1-e^{-\tau_\lambda}}{\tau_\lambda}$ where $\tau_\lambda = N({\rm H})\, C_{\rm ext}(\lambda)$ is the optical depth in the line of sight. The extinction cross-section per nucleon $C_{\rm ext}(\lambda)$ is taken from Weingartner & Draine (2001) for $R_V = 5.5$ and N(H) is a free parameter of the fit.

Method (ii) is precise for column densities higher than $N({\rm H}) \sim 10^{22}$ cm^{-2}. Method (i) can probe lower column densities but has two limitations. The AIB emission needs to be corrected for the variation in the UV field G_0 to retrieve the value of N(H). This was done assuming that G_0 scales as the inverse squared distance to the illuminating star HD200775 and a value of $G_0 = 2600$ at 42″ from this star (Pilleri et al. 2010). We used the projected distance as an estimate of the true distance. This introduces an error that can be especially strong at positions close to the star in the plane of the sky. Figure 3 shows that the AIB emission stays almost constant at $d < 16''$, therefore we used this value as the minimum effective distance of the NW PDR to the star. Method (i) also needs to be calibrated since the local emissivity of the AIB carriers is not known precisely. Our approach was therefore to derive a calibration factor using the values obtained by method (ii) around position 42″ on the star-NW cut. The same calibration factor was used for all positions along the two cuts. Figure 4 shows that the column densities that were derived on the two cuts correlate quite well with the [C II] line intensity.

3. Modelling C$^+$ emission

The critical density for the [C II] 158 μm line is $n_{\rm crit} = 2500\,{\rm cm}^{-3}$ for collisions with H and therefore the line emissivity depends mainly on temperature for n>n_{crit}. We selected a few positions on the HIFI S-NW [C II] cut, three points on the NW PDR and two on the South PDR (cf. Table 2). The values of G_0 were determined as explained in Sect. 2.3, and we assumed a constant average density with two different values: $n_{\rm H} = 2 \times 10^4$ cm^{-3} that is characteristic of the molecular cloud (Gerin et al. 1998) and $n_{\rm H} = 7 \times 10^3$ cm^{-3} that was derived by Rapacioli et al. (2006) in their study of PAH-related species.

We used the 1D Meudon PDR code (Le Petit et al. 2006) to compute the gas temperature T at the cloud surface for all the selected positions (cf. Table 2). The values of T are used to calculate the C$^+$ level populations. Line intensities are then derived by integrating along the line-of-sight (perpendicular to model results) and by assuming uniform excitation conditions. The thickness of the observed regions leads to an optical depth $\tau \sim 1$, which implies that transfer effects must be taken into account. If we assume constant excitation conditions and gas properties along the line of sight, then τ and the line intensity can be computed.

The agreement between calculated and observed flux values is very good when using $n_{\rm H} = 7 \times 10^3$ cm^{-3}. In the NW PDR, the ratio is 1.0 for NW3 (16) and NW2 (12), and 1.4 for NW1 (−3). For the S PDR, a value of 2.3 is derived for the two positions,

A&A 521, L25 (2010)

Table 2. Summary of the PDR modelling of the [C II] emission for 5 points along the HIFI S-NW cut ($\Delta\alpha = -47''$).

Pos. ($\Delta\delta$)	d_{proj}	UV field [a]	T [b]	PAH^+/PAH^0 [c]	Ionization parameter (γ) [b]	N(H) [d]	[C II] local emissivity [b]	[C II] flux	
								HIFI	Model [b]
($''$)	($''$)	(G_0)	(K)		(10^3 G_0 $K^{1/2}$ cm^3)	(10^{21} cm^{-2})	(10^{-21} W m^{-3})	(10^{-7} W m^{-2} sr^{-1})	
NW3 (16)	50	1873	337 / 333	1.9	11.0 / 29.5	10.5	4.4 / 1.4	8.0	11.0 / 8.0
NW2 (12)	48	1975	342 / 333	2.7	11.7 / 31.1	8.1	4.4 / 1.4	6.9	9.5 / 7.1
NW1 (–3)	47	2100	348 / 333	9.6	12.6 / 33.0	3.9	4.4 / 1.4	3.3	5.6 / 4.6
S1 (–63)	79	747	248 / 320	1.7	3.8 / 11.8	8.7	4.2 / 1.4	3.1	8.3 / 7.2
S2 (–73)	87	607	230 / 312	0.96	3.0 / 9.5	14.0	4.1 / 1.4	3.7	9.6 / 8.4

Notes. [a] Calculated using a projected distance and $G_0 = 2600$ at $42''$ from the star; [b] From the PDR model using $n_H = 2\times10^4/7\times10^3$ cm^{-3}, respectively; [c] Given as the ratio of the mid-IR intensities shown in Fig. 5; [d] Derived from the analysis of the mid-IR emission spectra.

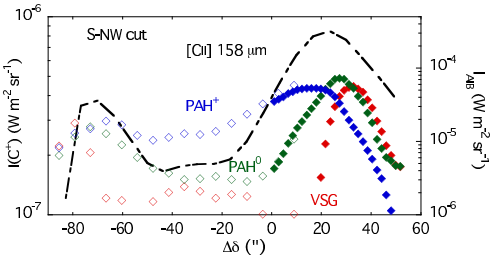

Fig. 5. S-NW cut in [C II] emission measured with HIFI at a beam size of $11''$(dot-dashed line) and distribution of the emission from the different very small dust populations, PAH^+ (blue), PAH^0 (green) and evaporating VSGs (red); filled diamonds are *Spitzer* data ($1.8''$ pix^{-1}) and open diamonds are ISOCAM data ($6''$ pix^{-1}).

suggesting that systematic effects are causing the deviation between observed and calculated values of the [C II] flux. There are several parameters that are not precise in our model but looking at Table 2, it seems the local [C II] emissivity is mainly affected by the local density and not by the value of G_0. For N(H), we assumed the same regions emit in PAHs and [C II] , in agreement with the profiles shown in Fig. 3. There is also an error for N(H) due to our method (cf. Sect. 2.3), but this error is expected to be the same for both PDRs. Dividing N(H) by a factor of two leads to lower values of the ratio of the calculated over the observed [CII] flux: 0.7–0.8 for the NW PDR and 1.6–1.7 for the S PDR.

One step further in the model would consist in studying the effect of the grain charge on the photoelectric efficiency (Bakes & Tielens 1994). The relative abundances of PAH^+, PAH^0, and evaporating VSGs vary significantly over the nebula (Fig. 5). Regions in the cavity appear mainly populated by PAH^+ (cf. NW1 (−3) in Table 2). Since the ionization potential of PAH^+ is much higher than that of PAH^0 (~10 eV compared to ~6 eV; Malloci et al. 2007), PAH^+ should contribute less to the photoelectric heating than PAH^0, leading to a decrease in the heating rate, hence in the gas cooling. In its current version, the PDR code uses classical grains with an MRN distribution (Mathis et al. 1977) and absorption and scattering cross-sections from Laor & Draine (1993). We have used grains of sizes from 15 Å to 3000 Å with a dust-to-gas mass ratio of 1%. As a result, the ionization parameter γ that quantifies the grain charge (cf. Table 2) does not reflect well the variations of the PAH charge observed in Fig. 5. An upgraded version, in which the PDR code is coupled to the code DUSTEM (Compiègne et al. 2010), is under development (Gonzalez et al., in prep.) and will allow for including PAHs. NGC 7023 is clearly a template region that could be used for these studies.

4. Conclusion

By using HIFI and complementary mid-IR data, we have shown that the [C II] cooling line and the AIB emission arise from the same regions, in the transition zone between atomic and molecular gas. The prototype PDR NGC 7023 was found to be a good object for comparison with PDR models. Further progress on the energetics of this region awaits for the coming [O I] data from the PACS instrument and a PDR model that treats the photophysics of PAHs consistently.

Acknowledgements. HIFI has been designed and built by a consortium of institutes and university departments from across Europe, Canada and the United States under the leadership of SRON Netherlands Institute for Space Research, Groningen, The Netherlands, and with major contributions from Germany, France, and the US. Consortium members are: Canada: CSA, U.Waterloo; France: CESR, LAB, LERMA, IRAM; Germany: KOSMA, MPIfR, MPS; Ireland, NUI Maynooth; Italy: ASI, IFSI-INAF, Osservatorio Astrofisico di Arcetri- INAF; Netherlands: SRON, TUD; Poland: CAMK, CBK; Spain: Observatorio Astronímico Nacional (IGN), Centro de Astrobiología (CSIC-INTA). Sweden: Chalmers University of Technology - MC2, RSS & GARD; Onsala Space Observatory; Swedish National Space Board, Stockholm University - Stockholm Observatory; Switzerland: ETH Zurich, FHNW; USA: Caltech, JPL, NHSC. This work was supported by the German *Deutsche Forschungsgemeinschaft, DFG* project number Os 177/1–1. A portion of this research was performed at the Jet Propulsion Laboratory, California Institute of Technology, under contract with the National Aeronautics and Space administration.

References

Abergel, A., Arab, H., Compiègne, M., et al. 2010, A&A, 518, L96
Bakes, E. L. O., & Tielens, A. G. G. M. 1994, ApJ, 427, 822
Berné, O., Joblin, C., Deville, Y., et al. 2007, A&A, 469, 575
Boulanger, F., Reach, W. T., Abergel, A., et al. 1996, A&A, 315, L325
Compiègne, M., Verstraete, L., Jones, A., et al. 2010, ApJ, submitted
de Graauw, Th., Helmich, F. P., Phillips, T. G., et al. 2010, A&A, 518, L6
Fuente, A., Martin-Pintado, J., Cernicharo, J., & Bachiller, R. 1993, A&A, 276, 473
Fuente, A., Martin-Pintado, J., Neri, R., Rogers, C., & Moriarty-Schieven, G. 1996, A&A, 310, 286
Gerin, M., Phillips, T. G., Keene, J., Betz, A. L., & Boreiko, R. T. 1998, ApJ, 500, 329
Habart, E., Verstraete, L., Boulanger, F., et al. 2001, A&A, 373, 702
Habing, H. J. 1968, Bull. Astron. Inst. Netherlands, 19, 421
Hollenbach, D. J., & Tielens, A. G. G. M. 1999, Rev. Mod. Phys., 71, 173
Laor, A., & Draine, B. T. 1993, ApJ, 402, 441
Le Petit, F., Nehmé, C., Le Bourlot, J., & Roueff, E. 2006, ApJS, 164, 506
Lemaire, J. L., Field, D., Gerin, M., et al. 1996, A&A, 308, 895
Malloci, G., Joblin, C., & Mulas, G. 2007, A&A, 462, 627
Martini, P., Sellgren, K., & Hora, J. L. 1997, ApJ, 484, 296
Mathis, J. S., Rumpl, W., & Nordsieck, K. H. 1977, ApJ, 217, 425
Ott, S. 2010, in Astronomical Data Analysis Software and Systems XIX, ed. Y Mizumoto, K. I. Morita, & M. Ohishi, ASP Conf. Ser., in press
Pilbratt, G. L., Riedinger, J. R., Passvogel, T., et al. 2010, A&A, 518, L1
Pilleri, P., Montillaud, J., Berné, O., & Joblin, C. 2010, A&A, submitted
Rapacioli, M., Joblin, C., & Boissel, P. 2005, A&A, 429, 193
Rapacioli, M., Calvo, F., Joblin, C., et al. 2006, A&A, 460, 519
Weingartner, J. C., & Draine, B. T. 2001, ApJ, 548, 296
Werner, M. W., Uchida, K. I., Sellgren, K., et al. 2004, ApJS, 154, 309

[1] Université de Toulouse, UPS, CESR, 9 avenue du colonel Roche, 31028 Toulouse Cedex 4, France
e-mail: christine.joblin@cesr.fr
[2] CNRS, UMR 5187, 31028 Toulouse, France
[3] Observatorio Astronómico Nacional (OAN), Apdo. 112, 28803 Alcalá de Henares (Madrid), Spain
[4] LERMA, Observatoire de Paris, 61 Av. de l'Observatoire, 75014 Paris, France
[5] Leiden Observatory, Universiteit Leiden, PO Box 9513, 2300 RA Leiden, The Netherlands
[6] I. Physikalisches Institut der Universität zu Köln, Zülpicher Straße 77, 50937 Köln, Germany
[7] SRON Netherlands Institute for Space Research, PO Box 800, 9700 AV Groningen, The Netherlands
[8] Observatoire de Paris, LUTH and Université Denis Diderot, Place J. Janssen, 92190 Meudon, France
[9] European Space Astronomy Centre, Urb. Villafranca del Castillo, PO Box 50727, 28080 Madrid, Spain
[10] Centro de Astrobiología, CSIC-INTA, 28850 Madrid, Spain
[11] Institute for Astronomy, ETH Zürich, 8093 Zürich, Switzerland
[12] Institut d'Astrophysique Spatiale, Université Paris-Sud, Bât. 121, 91405 Orsay Cedex, France
[13] Department of Astronomy and Astrophysics, University of Toronto, 60 St. George Street, Toronto, ON M5S 3H8, Canada
[14] Max-Planck-Institut für Radioastronomie, Auf dem Hügel 69, 53121, Bonn, Germany
[15] Astronomy Department, University of Maryland, College Park, MD 20742, USA
[16] Instituto de Radio Astronomía Milimétrica (IRAM), Avenida Divina Pastora 7, Local 20, 18012 Granada, Spain
[17] IPAC/Caltech, MS 100-22, Pasadena, CA 91125, USA
[18] Tata Institute of Fundamental Research (TIFR), Homi Bhabha Road, Mumbai 400005, India
[19] California Institute of Technology, 320-47, Pasadena, CA 91125-4700, USA
[20] Kapteyn Astronomical Institute, University of Groningen, PO box 800, 9700 AV Groningen, The Netherlands
[21] Jet Propulsion Laboratory, Caltech, Pasadena, CA 91109, USA
[22] MPI für Sonnensystemforschung, 37191 Katlenburg-Lindau, Germany

Conclusions [*en*]

In this thesis, I presented a multi-wavelength observational study of the evolution of PAH molecules and its impact in the chemical and physical processes in PDRs. The originality of the approach consists in combining studies on PAHs and smaller gas-phase species gathered from observations in the IR obtained with the ISO, *Spitzer* and AKARI satellites, and in the (sub-)mm domain obtained with the IRAM ground-based telescopes and the *Herschel* space observatory.

Main results

To study the evolution of PAH-related species in PDRs, we have developed a procedure that analyses the mid-IR emission in the Aromatic Infrared Bands (AIBs). This tool has been applied to a set of PDRs to trace the evolution from evaporating Very Small Grains (eVSGs) to free PAHs. We determined that the abundance of carbon locked in eVSGs compared to all carbon in the AIB carriers is related to the intensity of the local radiation field. This reflects an evolutionary scenario in which eVSGs are destroyed by the UV field giving birth to free PAHs. New millimeter observations on gas-phase species obtained at the IRAM 30 m telescope and the Plateau de Bure Interferometer have been compared with the IR observations to test a scenario in which small gas-phase hydrocarbons are produced by the photo-destruction of eVSGs.

We performed for the first time a search of a specific PAH, corannulene, in the millimeter wavelength domain. This search was not successful in identifying this specific PAH, but the derived upper limit has allowed to constrain the abundance of small PAHs in the Red Rectangle. The analysis of this result has shown that the formation process of PAHs in the envelopes of carbon rich-stars does not lead to large amount of small species, calling for an efficient growth mechanism.

Finally, we presented a comparative study of IR, sub-mm and millimeter observations to examine two PDRs in the reflection nebula NGC 7023. In particular, we show how the combination of [C II] line observations with the mid-IR PAH observations and millimeter data is a promising approach to study the geometry, energetics and dynamics of PDRs.

Perspectives

The work presented in this thesis has provided new insights into the role of PAHs in the chemical and physical processes of PDRs. Still, there are a number of open questions to be addressed. The evaporation of eVSGs into free PAHs and small hydrocar-

bons needs to be modelled in details to complete the photo-chemical scenario that has been proposed. A complete modelling of the geometry and chemistry of the studied regions is needed to understand to which extent the photo-processing of PAHs or eVSGs can contribute to the energetics and to the chemistry of PDRs. This faces the difficulties that neither PAHs nor eVSGs are associated yet with precise entities and this complicates the confrontation of astronomical data with laboratory measurements and quantum-mechanical calculations that are needed to address this problem. We can surely expect that the interpretation of the forthcoming *Herschel* observations will bring further constraints on the contribution of PAHs in the physics, chemistry and dynamics of gas-phase species in PDRs.

The identification of a specific PAH molecule is still an open issue of the PAH hypothesis. The instruments onboard *Herschel* provide now a great opportunity to search for the ro-vibrational transitions of specific PAHs in the sub-mm domain. As in the case of the search for corannulene in the Red Rectangle, the analysis of the Herschel observations with PAH emission models (Mulas *et al.*, 2006) will enable to place upper limits on the overall abundance of individual PAHs. We might also be able to identify some of them giving rise to detectable bands.

Finally, there are a number of observing facilities that will open new perspectives in these domains. In particular, the JCMT space observatory will be launched in 2014, and will provide spectro-imagery observations in the IR at sub-arcsecond scales. At about the same time, the ALMA interferometer will be fully operational, providing observations at comparable spatial resolution in the sub-mm and millimeter domains. The SPICA space mission, with in particular the European SAFARI instrument, will open the far-IR range again in 2020. The combination of multi-wavelength observations with an unprecedented sensitivity and spatial resolution will be the leading approach to study the role of PAHs and their related species in the chemistry and physics of PDRs in sources that are currently unresolved, such as proto-planetary disks and redshifted galaxies.

Conclusions [*fr*]

Dans cette thèse, j'ai présenté une étude observationnelle multi-longueur d'onde de l'évolution des PAH et de leur impact sur les processus physiques et chimiques dans les PDR. L'originalité de mon approche réside en la combinaison de l'étude des PAH et de petites espèces atomiques et moléculaires en phase gazeuse. Elle repose sur les observations dans le domaine infrarouge des satellites ISO, *Spitzer* et AKARI, et dans le domaine (sub-)millimétrique des radiotélescopes de l'IRAM et de l'observatoire spatial *Herschel*.

Principaux résultats

Afin d'étudier l'évolution des PAH et espèces dérivées dans les PDR, nous avons développé une procédure permettant d'analyser les bandes infrarouges aromatiques (AIB), dans le domaine infrarouge moyen. Cet outil a été appliqué à un ensemble de PDR pour sonder les liens d'évolution entre les très petits grains en cours d'évaporation (eVSG) et les PAH libres. Nous avons déterminé que l'abondance du carbone dans les eVSG rapportée à l'abondance du carbone dans l'ensemble des espèces responsables des AIB est liée à l'intensité du champ de rayonnement. Ce résultat conforte un scénario d'évolution selon lequel la destruction des eVSG par le champ de rayonnement UV génère des PAH libres. De nouvelles observations millimétriques de petites espèces moléculaires réalisées au télescope de 30 m de l'IRAM et à l'interféromètre du Plateau de Bure ont été comparées aux observations IR afin de tester un scénario dans lequel de petits hydrocarbures sont produits par la photodissociation des eVSG.

Nous avons réalisé la première recherche d'un PAH spécifique, le corannulène, dans le domaine millimétrique. Ce PAH n'ayant pas été identifié, nous en avons néanmoins déduit une limite supérieure à son abondance ce qui a permis de mettre en évidence que les processus de formation des PAH dans les enveloppes des étoiles carbonées conduisent à de faibles quantités de petits PAH, ce qui implique un mécanisme de croissance efficace.

Pour finir, nous présentons une étude comparative des observations IR, sub-millimétriques et millimétriques pour étudier deux PDR associées à la nébuleuse par réflexion NGC 7023. En particulier, nous montrons comment la combinaison des observations de la raie [C II] avec celle de l'émission des PAHs dans l'infrarouge moyen et du domaine millimétrique est une approche prometteuse pour l'étude de la géométrie, du bilan énergétique et de la dynamique des PDR.

Perspectives

Le travail présenté dans cette thèse fournit un nouvel éclairage sur le rôle des PAH dans les processus physiques et chimiques au sein des PDR. Il reste néanmoins un certain nombre de questions ouvertes. L'évaporation des eVSG en PAH libres et en petits hydrocarbures doit être modélisée en détails pour compléter le scenario photo-chimique proposé. Une modélisation complète de la géométrie et de la chimie des régions étudiées est nécessaire pour comprendre comment l'évolution photo-chimique des PAH et des eVSG influe sur le bilan énergétique et la chimie des PDR. Une difficulté majeure provient de ce que ni les PAH ni les eVSG ne sont pour le moment associés à des entités chimiques précises, ce qui complique la comparaison des données astronomiques aux mesures en laboratoire. Des expériences de laboratoire et des calculs de mécanique quantique sont nécessaires pour traiter ce problème. On doit s'attendre à ce que l'interprétation des observations *Herschel* à venir apporte de nouvelles contraintes sur la contribution des PAH à la physique, la chimie et la dynamique des espèces en phase gazeuse dans les PDR.

L'identification d'un PAH spécifique reste un enjeu majeur pour l'hypothèse PAH. Les instruments à bord du satellite *Herschel* fournissent une belle opportunité de chercher les transitions ro-vibrationnelles de PAH spécifiques dans le domaine submillimétrique. Comme dans le cas de la recherche du corannulène dans le Rectangle Rouge, l'analyse des observations d'*Herschel* à l'aide d'un modèle d'émission (Mulas *et al.*, 2006) permettra de donner des limites supérieures aux abondances de PAH individuels. Nous pourrions également être à même d'identifier certaines espèces émettant des bandes détectables.

Finalement, les futurs instruments d'observation vont ouvrir des nouvelles perspectives dans ces domaines. En particulier, le télescope spatial JWST devrait être lancé en 2014, et fournir des observations de spectro-imagerie dans le domaine infrarouge à des résolutions meilleures que la seconde d'arc. A peu près au même moment, l'interféromètre ALMA sera pleinement opérationnel et fournira des données aux mêmes résolutions spatiales dans les domaines millimétriques et sub-millimétriques. La mission spatiale SPICA, et en particulier son instrument européen SAFARI, observera de nouveau le domaine de l'infrarouge lointain à partir de 2020. La combinaison d'observations multi-longueur d'onde avec une sensibilité et une résolution spatiale sans précédent constituera la principale méthode d'étude du rôle des PAH et des espèces associées dans la chimie et la physique des PDR pour des sources actuellement non résolues, comme les disques protoplanétaires et les galaxies à grand redshift.

Appendices

Appendix

A

Study of the parameter space

The results of the fitting procedure presented in Chap. 5 are consistent with an evolutionary scenario in which the AIB carriers are processed by the UV radiation field. The relative weights of the band templates have been related to the physical conditions and evolutionary stage of different environments, such as PNe (Joblin *et al.*, 2008), protoplanetary disks (Berné *et al.*, 2009a), compact H II regions (Berné *et al.*, 2009b) and spatially resolved PDRs (Rapacioli *et al.*, 2005; Berné *et al.*, 2007, and Chap. 6). The consistency of the results with this scenario strongly suggests that, within its uncertainties, the methodology is reliable.

It is interesting to study the reliability of the fit results from a mathematical point of view to understand if the fit results are unique or if there is a degeneracy in the parameter space. Our fitting procedure is based on a maximum of 20 free parameters:

- 4 for the weights of the band template spectra: eVSG, PAH^0, PAH^+ and PAH^x
- 5 for the intensities of the H_2 rotational lines
- 2 (3) to define the (two-slope) continuum
- 1 for the column density
- 4 for the intensities of the ionised gas lines
- 3 for the intensities of the Lorentzian features at 6.9, 11.9 and 12.5 μm

In many cases, only a set of these parameters are used. In particular, in mild UV-excited PDRs that do not have an associated H II region the ionised gas lines are not observed and the continuum can be well represented with a single slope, reducing to 15 the number of free parameters.

The minimisation algorithm *mpfit* used by the procedure is very efficient to find the absolute minimum in the parameter space if the local minima are not very deep. Our tests show that the choice of the initial values for the 4 template weights does not influence the relative weights of the band templates of the fits, nor does the inclusion of the gas and

Lorentzian features in the fit. The estimate of the column density is subject, however, to larger uncertainties as discussed below.

The effect of the gas lines and Lorentzian features

We studied the effect of the gas and Lorentzian features on the results of the global fit. We performed the fit of several SL spectra, and compared the results obtained masking the Lorentzian features and the gas lines. Figure A.1 shows an example of the effect of masking the wavelengths corresponding to the gas lines and Lorentzian features. The relative intensities of each of the 4 band templates do not vary significantly, nor do the continuum shape and the value of the column density. In all the considered spectra, we found that masking the gas lines introduces a dispersion of less than 3% in the weights of the template spectra. The continuum and the estimate of the column density can however present larger variations, up to ~ 30%, in the tests we have performed.

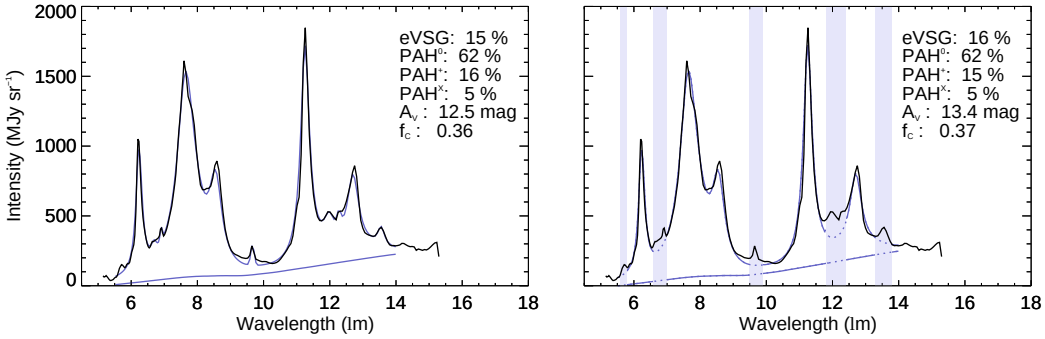

Figure A.1: The effect of masking the gas and Lorentzian features in the fit of region (2) of NGC 7023 NW (see Fig. 5.2). The results of the fits are almost unchanged.

The effect of column density

To study the quality of the fit and the dispersion of the results as a function of the value of the column density, we applied the fitting procedure to several PDR spectra by fixing the A_V parameter to given values. We then compared the results to that obtained with a free A_V parameter. Figure A.2 shows some examples of the results obtained for very different values of A_V, as well as the variation of the χ^2 as a function of A_V.

This analysis shows that good quality fits can be obtained for several values of A_V, and that *mpfit* overcome the local minima in this parameter space. The relative weights of the AIB populations are slightly influenced by these variations, as long as the quality of the fit is acceptable. In the majority of cases, values of A_V that differ by less than a factor 2 yield variations in the weights of the band templates by less than 10%.

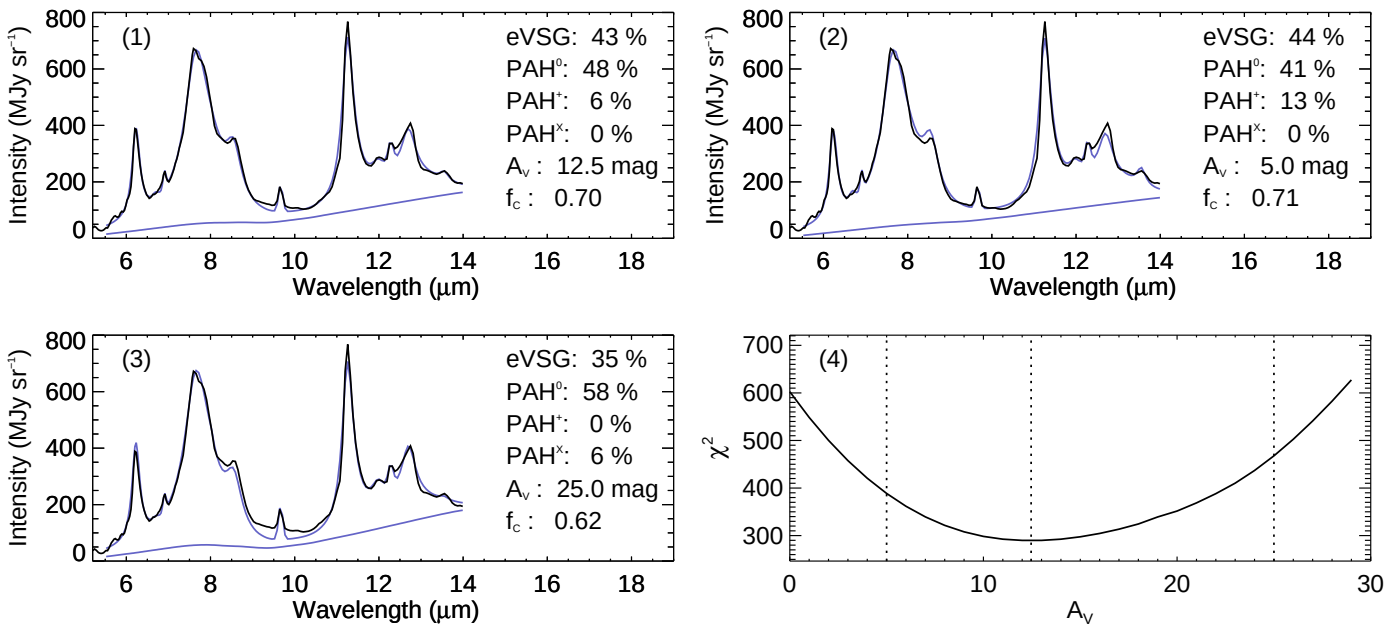

Figure A.2: Examples of the fit results towards position 2 of Fig. 5.2. The first panel shows the results of the fit with the A_V parameter free. The fit obtained with different values of A_V are displayed in the second and third panel. They show variations of the relative weights of the band templates up to 10% for differences in A_V by a factor of 2. The variation of the χ^2 with A_V is shown in panel 4.

Molecules detected in space

Species	Mass	Species	Mass	Species	Mass	Species	Mass
H_2	2	CF^+	31	SiO	44	NaCl	58
H_3^+	3	CH_3NH_2	31	HCS^+	45	CH_3CONH_2	59
CH^+	13	H_3CO^+	31	$HOCO^+$	45	HNCS	59
CH	13	HNO	31	NH_2CHO	45	C_5	60
CH_2	14	CH_3OH	32	PN	45	CH_2OHCHO	60
CH_3	15	SiH_4	32	AlF	46	CH_3COOH	60
NH	15	HS	33	C_2H_5OH	46	$HCOOCH_3$	60
CH_4	16	HS^+	33	CH_3OCH_3	46	OCS	60
NH_2	16	H_2S	34	H_2CS	46	SiS	60
NH_3	17	H_2S^+	34	HCOOH	46	C_5H	61
OH	17	C_3	36	NS	46	AlCl	62
OH^+	17	HCl	36	CH_3SH	48	$HOCH_2CH_2OH$	62
H_2O	18	c-C_3H	37	SO	48	HC_4N	63
H_2O^+	18	l-C_3H	37	SO^+	48	CH_3C_4H	64
NH_4^+	18	c-C_3H_2	38	C_4H	49	S_2	64
H_3O^+	19	H_2CCC	38	C_4H^-	49	SiC_3	64
HF	20	HCCN	39	NaCN	49	SO_2	64
C_2	24	C_2O	40	C_3N	50	CH_2CCHCN	65
C_2H	25	CH_2CN	40	H_2CCCC	50	CH_3C_3N	65
C_2H_2	26	CH_3CCH	40	HCCCCH	50	C_3S	68
CN	26	SiC	40	MgCN	50	FeO	72
CN^+	26	CH_3CN	41	MgNC	50	C_6H	73
HCN	27	CH_3NC	41	HC_3N	51	C_6H^-	73
HNC	27	H_2CCO	42	HCCNC	51	C_5N	74
C_2H_4	28	NH_2CN	42	HNCCC	51	C_6H_2	74
CO	28	SiN	42	c-SiC_2	52	HCCCCCCH	74
CO^+	28	OCN^-	42	C_3O	52	HC_5N	75
H_2CN	28	CH_3CHCH_2	42	$H_2C_3N^+$	52	KCl	75
$HCNH^+$	28	CP	43	AlNC	53	SiC_4	76
N_2^+	28	HNCO	43	CH_2CHCN	53	C_6H_6	78
CH_2NH	29	HOCN	43	c-H_2C_3O	54	C_7H	85
HCO	29	HCNO	43	HC_2CHO	54	CH_3C_6H	88
HCO^+	29	$HNCO^-$	43	SiCN	54	C_8H	97
HN_2^+	29	c-C_2H_4O	44	SiNC	54	C_8H^-	97
HOC^+	29	CH_3CHO	44	CH_3CH_2CN	55	HC_7N	99
SiH	29	CO_2	44	C_2S	56	HC_9N	123
CH_3CH_3	30	CO_2^+	44	C_3H_4O	56	$HC_{11}N$	147
H_2CO	30	CS	44	CH_3CH_2CHO	58	-	-
NO	30	N_2O	44	CH_3COCH_3	58	-	-

Adapted from http://www.astrochemistry.net

The list comprehends molecules that have been detected in the ISM, considering different environments.

List of acronyms

AGB	Asymptotic Giant Branch
AIB	Aromatic Infrared Bands
ALMA	Atacama Large Millimeter/sub-millimeter Array
BG	Big Grains
CFHT	Canada France Hawai Telescope
CMM	Cold Molecular Medium
CNM	Cold Neutral Medium
CVF	Circular Variable Filter
DIB	Diffuse Interstellar Bands
DSB	Double Side Band
ERE	Extended Red Emission
eVSG	Evaporating Very Small Grains
FIS	Far-Infrared Surveyor
FTS	Fourier Transform Spectrometer
FWHM	Full Width at Half Maximum
HAe	Herbig Ae
HBe	Herbig Be
HERA	HEterodyne Receiver Array
HIFI	Heterodyne Instrument for the Far Infrared
HIM	Hot Ionized Medium
HRS	High Resolution Spectrometer
HST	Hubble Space Telescope
IC	Internal Conversion
IR	InfraRed
IRAC	InfraRed Array Camera
IRAM	Istituto de Radio Astronomia Millimetrica
IRAS	InfraRed Astronomical Satellite
IRC	InfraRed Camera
IRS	InfraRed Spectrograph
ISM	Interstellar Medium
ISO	Infrared Space Observatory
ISRF	Interstellar Radiation Field
JWST	James Webb Space Telescope
IVR	Internal Vibrational Redistribution
KAO	Kuiper Airborne Observatory

LH	Long High (order of IRS)
LL	Long Low (order of IRS)
LO	Local Oscillator
LSB	Lower Side Band
LWS	Long Wavelength Spectrometer
MIPS	Multiband Imaging Photometer and Spectrometer
MW	Milky Way
PACS	Photodetector Array Camera and Spectrometer
PAH	Polycyclic Aromatic Hydrocarbons
PDBI	Plateau de Bure Interferometer
PDR	Photo-Dissociation Region
PN	Planetary Nebula
SED	Spectral Energy Distribution
SH	Short High (order of IRS)
SL	Short Low (oreder of IRS)
SOFIA	Stratospheric Observatory for Infrared Astronomy
SPICA	Space Infra-Red Telescope for Cosmology and Astrophysics
SPIRE	Spectral and Photometric Imaging Receiver
SSB	Single Side Band
SWS	Short Wavelength Spectrometer
UV	UltraViolet
UCH II	Ultra Compact H II
USB	Upper Side Band
VSG	Very Small Grains
WADI	Warm and Dense Interstellar Medium
WBS	Wide Band Spectrometer
WIM	Warm Ionized Medium
WNM	Warm Neutral Medium

Publications

Refereed publications

1. **P. Pilleri**, D. Herberth, T. Giesen, M. Gerin, *et al.*
Search for Corannulene ($C_{20}H_{10}$) in the Red Rectangle , MNRAS 397 1053-1060 (2009)

2. O. Berné, A. Fuente, J.R. Goicoechea, **P. Pilleri** *et al.*
Mid-Infrared Polycyclic Aromatic Hydrocarbon and H2 Emission as a Probe of Physical Conditions in Extreme Photodissociation Regions, ApJ 706 L160-L163 (2009)

3. C. Joblin, **P. Pilleri**, J. Montillaud, A. Fuente *et al.*
Gas morphology and energetics at the surface of PDRs: new insights with Herschel observations of NGC 7023, A&A 521:L25+ (2010)

4. A. Fuente, O. Berné, J. Cernicharo, ... , **P. Pilleri** *et al.*
Herschel observations in the ultracompact HII region Mon R2: Water in dense Photon-dominated regions (PDRs), A&A 521:L23+ (2010)

5. C. Dedes, Y. Okada, B. Mookerjea, ... , **P. Pilleri** *et al.*
The origin of the C^+ emission in the S140 PDRs - new insights from HIFI, A&A letters - HIFI special issue, A&A 521:L24+ (2010)

6. **P. Pilleri**, J. Montillaud, O. Berné, C. Joblin *et al.*
Evaporating Very Small Grains as a tracer of the UV radiation field in Photo Dissociation Regions, to be submitted to A&A

Proceedings

1. O. Berné, **P. Pilleri**, C. Joblin *et al.*
The shape of mid-IR PAH bands in the universe. To appear in the proceedings of the PAHs and the Universe Symposium; Toulouse (France), May 31 - June 4, 2010.

2. F. Boulanger, T. Onaka, **P. Pilleri**, C. Joblin *et al.*
Spectroscopic view at the near-IR emission from interstellar dust and its relation to PAHs. To appear in the proceedings of the PAHs and the Universe Symposium; Toulouse (France), May 31-June 4, 2010.

CONTRIBUTION TO CONFERENCES

Talks

- **P. Pilleri**, D. Herberth, M. Gerin *et al.*;
  Search for Corannulene in the Red Rectangle; Toulouse Nanograin Workshop, Toulouse (France), November 13-14, 2008
- **P. Pilleri**, D. Herberth, M. Gerin *et al.*;
  Search for Corannulene in the Red Rectangle; Molecular Universe final meeting, Boppard (Germany), September 1-5, 2008

Posters

- **P. Pilleri**, O. Berné, M. Gerin, *et al.*;
  The geometry of the NGC 7023 NW PDR revealed by mid- IR and (sub-)mm observations; Cosmic dust near and Far; Heidelberg, Germany, September 8-12, 2008
- **P. Pilleri**, O Berné, M. Gerin, *et al.*
  Combining molecular, PAH and dust observations to constrain the geometry of the NGC 7023 NW PDR; The Molecular Universe: an International Meeting on Physics and Chemistry of the Interstellar Medium. Arcachon (France), May 5-8, 2008
- **P. Pilleri**, C. Joblin, O. Berné, *et al.*
  Destruction of very small carbon particles and hydrocarbon production in PDRs: 1 - observation Journées ASA/ALMA 2009; Grenoble (France), April 6-7, 2009.
- C. Joblin, O. Berné, **P. Pilleri**, *et al.*
  The Search for PAH Bands with Herschel: Preliminary Results. Herschel First Results Symposium ; ESLAB ; Noorwijk (The netherlands); May 4-7, 2010.
- **P. Pilleri** A. Fuente, C. Joblin, *et al.*
  Photo-Induced Chemistry at the Surface of PDRs: new Insights with Herschel Observations of NGC 7023 Herschel First Results Symposium; ESLAB ; Noorwijk (The netherlands); May 4-7, 2010.
- Y. Okada, ... , **P. Pilleri**, *et al.*
  Spatial distributions of PAH and molecular hydrogen emissions in star-forming regions. PAHs and the Universe; Toulouse (France), May 31-June 4, 2010.
- Y. Okada, O.Berné, **P. Pilleri**, *et al.*
  PDR properties and spatial structures probed by Herschel and Spitzer spectroscopy. 5^{th} Zermatt ISM symposium: conditions and impact of star formation. New results with Herschel and beyond ; Zermatt (Switzerland), September 19 -24, 2010.

List of Figures

List of Tables

Bibliography

Abergel, A., **Arab, H.**, **Compiègne, M.**, *et al. Evolution of interstellar dust with Herschel. First results in the photodissociation regions of NGC 7023*. A&A, 518:L96+ (2010)

Abergel, A., **Teyssier, D.**, **Bernard, J. P.**, *et al. ISOCAM and molecular observations of the edge of the Horsehead nebula*. A&A, 410:577–585 (2003)

Acke, B., **Bouwman, J.**, **Juhász, A.**, *et al. Spitzer's View on Aromatic and Aliphatic Hydrocarbon Emission in Herbig Ae Stars*. ApJ, 718:558–574 (2010)

Alecian, E., **Catala, C.**, **Wade, G. A.**, *et al. Characterization of the magnetic field of the Herbig Be star HD200775*. MNRAS, 385:391–403 (2008)

Allamandola, L. J., **Tielens, A. G. G. M.**, and **Barker, J. R.** *Polycyclic aromatic hydrocarbons and the unidentified infrared emission bands - Auto exhaust along the Milky Way*. ApJ, 290:L25–L28 (1985)

Bakes, E. L. O. and **Tielens, A. G. G. M.** *The photoelectric heating mechanism for very small graphitic grains and polycyclic aromatic hydrocarbons*. ApJ, 427:822–838 (1994)

Beirão, P., **Brandl, B. R.**, **Appleton, P. N.**, *et al. Spatially Resolved Spitzer IRS Spectroscopy of the Central Region of M82*. ApJ, 676:304–316 (2008)

Bergin, E. A., **Melnick, G. J.**, **Gerakines, P. A.**, *et al. Spitzer Observations of CO_2 Ice toward Field Stars in the Taurus Molecular Cloud*. ApJ, 627:L33–L36 (2005)

Berné, O., **Fuente, A.**, **Goicoechea, J. R.**, *et al. Mid-Infrared Polycyclic Aromatic Hydrocarbon and H_2 Emission as a Probe of Physical Conditions in Extreme Photodissociation Regions*. ApJ, 706:L160–L163 (2009a)

Berné, O., **Joblin, C.**, **Deville, Y.**, *et al. Analysis of the emission of very small dust particles from Spitzer spectro-imagery data using blind signal separation methods*. A&A, 469:575–586 (2007)

Berné, O., **Joblin, C.**, **Fuente, A.**, *et al. What can we learn about protoplanetary disks from analysis of mid-infrared carbonaceous dust emission?* A&A, 495:827–835 (2009b)

Berné, O., **Joblin, C.**, **Rapacioli, M.**, *et al. Extended Red Emission and the evolution of carbonaceous nanograins in NGC 7023*. A&A, 479:L41–L44 (2008)

Bernstein, M. P., **Sandford, S. A.**, and **Allamandola, L. J.** *Hydrogenated Polycyclic Aromatic Hydrocarbons and the 2940 and 2850 Wavenumber (3.40 and 3.51 micron) Infrared Emission Features*. ApJ, 472:L127+ (1996)

Bless, R. C. and **Savage, B. D.** *Ultraviolet Photometry from the Orbiting Astronomical Observatory. II. Interstellar Extinction*. ApJ, 171:293–+ (1972)

Boersma, C., **Hony, S.**, and **Tielens, A. G. G. M.** *UIR bands in the ISO SWS spectrum of the carbon star TU Tauri*. A&A, 447:213–220 (2006)

Bot, C., **Boulanger, F.**, **Lagache, G.**, *et al. Multi-wavelength analysis of the dust emission in the Small Magellanic Cloud*. A&A, 423:567–577 (2004)

Boulanger, F., **Abergel, A.**, **Bernard, J. P.**, *et al. The Nature of Small Interstellar Dust Particles*. In **J. Yun & L. Liseau**, editor, *Star Formation with the Infrared Space Observatory*, volume 132 of *Astronomical Society of the Pacific Conference Series*, pages 15–+ (1998)

Boulanger, F., **Falgarone, E.**, **Puget, J. L.**, *et al. Variations in the abundance of transiently heated particles within nearby molecular clouds*. ApJ, 364:136–145 (1990)

Boulanger, F., **Lorente, R.**, **Miville Deschênes, M. A.**, *et al. Mid-IR spectro-imaging observations with the ISOCAM CVF: Final reduction and archive*. A&A, 436:1151–1158 (2005)

Bujarrabal, V., **Castro-Carrizo, A.**, **Alcolea, J.**, *et al. The orbiting gas disk in the Red Rectangle*. A&A, 441:1031–1038 (2005)

Burton, M. G., **Howe, J. E.**, **Geballe, T. R.**, *et al. Near-IR fluorescent molecular hydrogen emission from NGC 2023*. Publications of the Astronomical Society of Australia, 15:194–201 (1998)

Cami, J., **Bernard-Salas, J.**, **Peeters, E.**, *et al. Detection of C_{60} and C_{70} in a Young Planetary Nebula*. Science, 329:1180– (2010)

Cardelli, J. A., **Clayton, G. C.**, and **Mathis, J. S.** *The relationship between infrared, optical, and ultraviolet extinction*. ApJ, 345:245–256 (1989)

Cernicharo, J., **Heras, A. M.**, **Tielens, A. G. G. M.**, *et al. Infrared Space Observatory's Discovery of C_4H_2, C_6H_2, and Benzene in CRL 618*. ApJ, 546:L123–L126 (2001)

Cesarsky, C. J., **Abergel, A.**, **Agnese, P.**, *et al. ISOCAM in flight.* A&A, 315:L32–L37 (1996)

Cesarsky, D., **Lequeux, J.**, **Ryter, C.**, *et al. ISO observations of the reflection nebula Ced 201: evolution of carbonaceous dust*. A&A, 354:L87–L91 (2000)

Cherchneff, I. *A chemical study of the inner winds of asymptotic giant branch stars*. A&A, 456:1001–1012 (2006)

Cherchneff, I., **Barker, J. R.**, and **Tielens, A. G. G. M.** *Polycyclic aromatic hydrocarbon formation in carbon-rich stellar envelopes*. ApJ, 401:269–287 (1992)

Chokshi, A., **Tielens, A. G. G. M.**, **Werner, M. W.**, *et al. C II 158 micron and O I 63 micron observations of NGC 7023 - A model for its photodissociation region*. ApJ, 334:803–814 (1988)

Clegg, P. E., **Ade, P. A. R.**, **Armand, C.**, *et al. The ISO Long-Wavelength Spectrometer.* A&A, 315:L38–L42 (1996)

Cohen, M., **Anderson, C. M.**, **Cowley, A.**, *et al. The peculiar object HD 44179 /'The red rectangle'/.* ApJ, 196:179–189 (1975)

Colbert, J. W., **Malkan, M. A.**, **Clegg, P. E.**, *et al. ISO LWS Spectroscopy of M82: A Unified Evolutionary Model*. ApJ, 511:721–729 (1999)

Compiègne, M., **Abergel, A.**, **Verstraete, L.**, *et al. Dust processing in photodissociation regions. Mid-IR emission modelling*. A&A, 491:797–807 (2008)

Compiègne, M., **Verstraete, L.**, **Jones, A.**, *et al.* . ApJ, page submitted (2010)

Dartois, E., **Muñoz Caro, G. M.**, **Deboffle, D.**, *et al. Diffuse interstellar medium organic polymers. Photoproduction of the 3.4, 6.85 and 7.25 μm features*. A&A, 423:L33–L36 (2004)

de Graauw, T., **Haser, L. N.**, **Beintema, D. A.**, *et al. Observing with the ISO Short-Wavelength Spectrometer.* A&A, 315:L49–L54 (1996)

de Graauw, T., **Helmich, F. P.**, **Phillips, T. G.**, *et al. The Herschel-Heterodyne Instrument for the Far-Infrared (HIFI)*. A&A, 518:L6+ (2010)

DeFrees, D. J., **Miller, M. D.**, **Talbi, D.**, *et al. Theoretical infrared spectra of some model polycyclic aromatic hydrocarbons - Effect of ionization*. ApJ, 408:530–538 (1993)

Désert, F. X., **Boulanger, F.**, **Léger, A.**, *et al. Nature of very small grains - PAH molecules or silicates?* A&A, 159:328–330 (1986)

Désert, F.-X., **Boulanger, F.**, and **Puget, J. L.** *Interstellar dust models for extinction and emission*. A&A, 237:215–236 (1990)

D'Hendecourt, L. B., **Léger, A.**, **Olofsson, G.**, *et al. The Red Rectangle - A possible case of visible luminescence from polycyclic aromatic hydrocarbons*. A&A, 170:91–96 (1986)

Dieter, N. H. *Radio Observations of the Interstellar OH Line at 1,667 Mc/s*. Nature, 201:279–281 (1964)

Diplas, A. and **Savage, B. D.** *An IUE survey of interstellar H I LY alpha absorption. 1: Column densities*. ApJS, 93:211–228 (1994)

Disney, M., **Davies, J.**, and **Phillipps, S.** *Are galaxy discs optically thick?* MNRAS, 239:939–976 (1989)

Draine, B. and **Bertoldi, F.** *Theoretical Models of Photodissociation Fronts*. In **F. Combes & G. Pineau Des Forets**, editor, *Molecular Hydrogen in Space*, pages 131–+ (2000)

Draine, B. T. *Interstellar Dust Grains*. ARA&A, 41:241–289 (2003)

Draine, B. T. *Interstellar Dust Models and Evolutionary Implications*. In **T. Henning, E. Grün, & J. Steinacker**, editor, *Astronomical Society of the Pacific Conference Series*, volume 414 of *Astronomical Society of the Pacific Conference Series*, pages 453–+ (2009)

Draine, B. T. and **Lazarian, A.** *Electric Dipole Radiation from Spinning Dust Grains*. ApJ, 508:157–179 (1998)

Draine, B. T. and **Lee, H. M.** *Optical properties of interstellar graphite and silicate grains*. ApJ, 285:89–108 (1984)

Draine, B. T. and **Li, A.** *Infrared Emission from Interstellar Dust. IV. The Silicate-Graphite-PAH Model in the Post-Spitzer Era*. ApJ, 657:810–837 (2007)

Engelbracht, C. W., **Kundurthy, P.**, **Gordon, K. D.**, *et al. Extended Mid-Infrared Aromatic Feature Emission in M82*. ApJ, 642:L127–L132 (2006)

Fazio, G. G., **Hora, J. L.**, **Allen, L. E.**, *et al. The Infrared Array Camera (IRAC) for the Spitzer Space Telescope*. ApJS, 154:10–17 (2004)

Field, D., **Gerin, M.**, **Leach, S.**, *et al. High spatial resolution observations of H_2_ vibrational fluorescence in NGC 2023*. A&A, 286:909–914 (1994)

Field, G. B. *Interstellar abundances: gas and dust.* ApJ, 187:453–459 (1974)

Finkenzeller, U. *Rotational velocities, spectral types, and forbidden lines of Herbig Ae/Be stars*. A&A, 151:340–348 (1985)

Fitzpatrick, E. L. and **Massa, D.** *An analysis on the shapes of ultraviolet extinction curves. I - The 2175 A bump.* ApJ, 307:286–294 (1986)

Fitzpatrick, E. L. and **Massa, D.** *An analysis of the shapes of ultraviolet extinction curves. II - The far-UV extinction.* ApJ, 328:734–746 (1988)

Foing, B. H. and **Ehrenfreund, P.** *Detection of Two Interstellar Absorption Bands Coincident with Spectral Features of* C_{60}^{+} . Nature, 369:296–+ (1994)

Fossé, D., **Cesarsky, D.**, **Gerin, M.**, *et al. AIBs and carbon chains in PDRs*. In **A. Salama, M. F. Kessler, K. Leech, & B. Schulz**, editor, *ISO Beyond the Peaks: The 2nd ISO Workshop on Analytical Spectroscopy*, volume 456 of *ESA Special Publication*, pages 91–+ (2000)

Frenklach, M. and **Feigelson, E. D.** *Formation of polycyclic aromatic hydrocarbons in circumstellar envelopes.* ApJ, 341:372–384 (1989)

Fuente, A., **García-Burillo, S.**, **Usero, A.**, *et al. On the chemistry and distribution of* HOC^{+} *in M 82. More evidence for extensive PDRs.* A&A, 492:675–684 (2008)

Fuente, A., **Martin-Pintado, J.**, **Cernicharo, J.**, *et al. A chemical study of the photodissociation region NGC 7023.* A&A, 276:473–+ (1993)

Fuente, A., **Martin-Pintado, J.**, and **Gaume, R.** *High-density CN filaments in NGC 2023.* ApJ, 442:L33–L36 (1995)

Fuente, A., **Martin-Pintado, J.**, **Neri, R.**, *et al. The filamentary structure of the interface between the atomic and the molecular phases in NGC 7023.* A&A, 310:286–296 (1996)

Fuente, A., **Martín-Pintado, J.**, **Rodríguez-Fernández, N. J.**, *et al. Infrared Space Observatory Observations toward the Reflection Nebula NGC 7023: A Nonequilibrium Ortho-to-Para-H_2 Ratio.* ApJ, 518:L45–L48 (1999)

Fuente, A., **Martin-Pintado, J.**, **Rodriguez-Franco, A.**, *et al. The biconical cavity associated with HD 200775: the formation of a cometary nebula.* A&A, 339:575–586 (1998)

Fuente, A., **Rodrıguez-Franco, A.**, **Garcıa-Burillo, S.**, *et al. Observational study of reactive ions and radicals in PDRs.* A&A, 406:899–913 (2003)

Galazutdinov, G. A., **Krełowski, J.**, **Musaev, F. A.**, *et al. On the identification of the* C_{60}^{+} *interstellar features.* MNRAS, 317:750–758 (2000)

Galliano, F., **Madden, S. C.**, **Tielens, A. G. G. M.**, *et al. Variations of the Mid-IR Aromatic Features inside and among Galaxies.* ApJ, 679:310–345 (2008)

Geballe, T. R., **Tielens, A. G. G. M.**, **Allamandola, L. J.**, *et al. Spatial variations of the 3 micron emission features within UV-excited nebulae - Photochemical evolution of interstellar polycyclic aromatic hydrocarbons*. ApJ, 341:278–287 (1989)

Gerakines, P. A., **Schutte, W. A.**, **Greenberg, J. M.**, *et al. The infrared band strengths of H_2_O, CO and CO_2_ in laboratory simulations of astrophysical ice mixtures*. A&A, 296:810–+ (1995)

Gerakines, P. A., **Whittet, D. C. B.**, **Ehrenfreund, P.**, *et al. Observations of Solid Carbon Dioxide in Molecular Clouds with the Infrared Space Observatory*. ApJ, 522:357–377 (1999)

Gerin, M., **Fossé, D.**, and **Roueff, E.** *Carbon Chemistry in Interstellar Clouds*. In **C. L. Curry & M. Fich**, editor, *SFChem 2002: Chemistry as a Diagnostic of Star Formation*, pages 81–+ (2003)

Gerin, M., **Pety, J.**, and **Goicoechea, J. R.** *The Horsehead Nebula, a Template Source for Interstellar Physics and Chemistry*. In **D. C. Lis, J. E. Vaillancourt, P. F. Goldsmith, T. A. Bell, N. Z. Scoville, & J. Zmuidzinas**, editor, *Astronomical Society of the Pacific Conference Series*, volume 417 of *Astronomical Society of the Pacific Conference Series*, pages 165–+ (2009)

Gerin, M., **Phillips, T. G.**, **Keene, J.**, *et al. CO, C i, and C II Observations of NGC 7023*. ApJ, 500:329–+ (1998)

Griffin, M. J., **Abergel, A.**, **Abreu, A.**, *et al. The Herschel-SPIRE instrument and its in-flight performance*. A&A, 518:L3+ (2010)

Habart, E., **Abergel, A.**, **Walmsley, C. M.**, *et al. Density structure of the Horsehead nebula photo-dissociation region*. A&A, 437:177–188 (2005)

Habart, E., **Boulanger, F.**, **Verstraete, L.**, *et al.* H_2 *infrared line emission across the bright side of the rho Ophiuchi main cloud*. A&A, 397:623–634 (2003)

Habart, E., **Verstraete, L.**, **Boulanger, F.**, *et al. Photoelectric effect on dust grains across the L1721 cloud in the rho Ophiuchi molecular complex*. A&A, 373:702–713 (2001)

Habing, H. J. *The interstellar radiation density between 912 A and 2400 A*. Bull. Astron. Inst. Netherlands, 19:421–+ (1968)

Herbig, G. H. *The Diffuse Interstellar Bands*. ARA&A, 33:19–74 (1995)

Hollenbach, D. J. and **Tielens, A. G. G. M.** *Photodissociation regions in the interstellar medium of galaxies*. Reviews of Modern Physics, 71:173–230 (1999)

Hony, S., **Van Kerckhoven, C.**, **Peeters, E.**, *et al. The CH out-of-plane bending modes of PAH molecules in astrophysical environments*. A&A, 370:1030–1043 (2001)

Houck, J. R., **Roellig, T. L.**, **van Cleve, J.**, *et al. The Infrared Spectrograph (IRS) on the Spitzer Space Telescope*. ApJS, 154:18–24 (2004)

Iglesias-Groth, S., **Manchado, A.**, **García-Hernández, D. A.**, *et al. Evidence for the Naphthalene Cation in a Region of the Interstellar Medium with Anomalous Microwave Emission*. ApJ, 685:L55–L58 (2008)

Iglesias-Groth, S., **Manchado, A.**, **Rebolo, R.**, *et al. A search for interstellar anthracene towards the Perseus anomalous microwave emission region*. MNRAS, pages 1136–+ (2010)

Joblin, C., **Léger, A.**, and **Martin, P.** *Contribution of polycyclic aromatic hydrocarbon molecules to the interstellar extinction curve*. ApJ, 393:L79–L82 (1992)

Joblin, C., **Pilleri, P.**, **Montillaud, J.**, *et al. Gas morphology and energetics at the surface of PDRs: New insights with Herschel observations of NGC 7023*. A&A, 521:L25+ (2010)

Joblin, C., **Szczerba, R.**, **Berné, O.**, *et al. Carriers of the mid-IR emission bands in PNe reanalysed. Evidence of a link between circumstellar and interstellar aromatic dust*. A&A, 490:189–196 (2008)

Joblin, C., **Tielens, A. G. G. M.**, **Allamandola, L. J.**, *et al. Spatial Variation of the 3.29 and 3.40 Micron Emission Bands within Reflection Nebulae and the Photochemical Evolution of Methylated Polycyclic Aromatic Hydrocarbons*. ApJ, 458:610–+ (1996a)

Joblin, C., **Tielens, A. G. G. M.**, **Geballe, T. R.**, *et al. Variations of the 8.6 and 11.3 MU M Emission Bands within NGC 1333: Evidence for PAH Cations*. ApJ, 460:L119+ (1996b)

Joblin, C., **Toublanc, D.**, **Boissel, P.**, *et al. Calculations of the far-infrared emission of $C_{24}H_{12}$ under interstellar conditions*. Molecular Physics, 100:3595–3600 (2002)

Jura, M., **Balm, S. P.**, and **Kahane, C.** *A Long-lived Disk around the Red Rectangle?* ApJ, 453:721–+ (1995)

Kaufman, M. J., **Wolfire, M. G.**, **Hollenbach, D. J.**, *et al. Far-Infrared and Submillimeter Emission from Galactic and Extragalactic Photodissociation Regions*. ApJ, 527:795–813 (1999)

Kawada, M., **Baba, H.**, **Barthel, P. D.**, *et al. The Far-Infrared Surveyor (FIS) for AKARI*. PASJ, 59:389–+ (2007)

Kemper, F., **Vriend, W. J.**, and **Tielens, A. G. G. M.** *Erratum: The Absence of Crystalline Silicates in the Diffuse Interstellar Medium*. ApJ, 633:534–534 (2005)

Kessler, M. F. *The ISO mission: past and future*. In **P. Cox & M. Kessler**, editor, *The Universe as Seen by ISO*, volume 427 of *ESA Special Publication*, pages 23–+ (1999)

Kokkin, D. L., **Troy, T. P.**, **Nakajima, M.**, *et al. The Optical Spectrum of a Large Isolated Polycyclic Aromatic Hydrocarbon: Hexa-peri-hexabenzocoronene, $C_{42}H_{18}$.* ApJ, 681:L49–L51 (2008)

Kurucz, R. L. *Model Atmospheres (Kurucz, 1979).* VizieR Online Data Catalog, 6039:0–+ (1993)

Kwok, S. *The synthesis of organic and inorganic compounds in evolved stars.* Nature, 430:985–991 (2004)

Lafleur, A. L., **Howard, J. B.**, **Marr, J. A.**, *et al. Proposed fullerene precursor corannulene identified in flames both in the presence and absence of fullerene production.* J. Phys. Chem., 97:13539–13543 (1993)

Laor, A. and **Draine, B. T.** *Spectroscopic constraints on the properties of dust in active galactic nuclei.* ApJ, 402:441–468 (1993)

Le Page, V., **Snow, T. P.**, and **Bierbaum, V. M.** *Hydrogenation and Charge States of Polycyclic Aromatic Hydrocarbons in Diffuse Clouds. II. Results.* ApJ, 584:316–330 (2003)

Le Petit, F., **Nehmé, C.**, **Le Bourlot, J.**, *et al. A Model for Atomic and Molecular Interstellar Gas: The Meudon PDR Code.* ApJS, 164:506–529 (2006)

Léger, A. and **Puget, J. L.** *Identification of the 'unidentified' IR emission features of interstellar dust?* A&A, 137:L5–L8 (1984)

Lemaire, J. L., **Field, D.**, **Gerin, M.**, *et al. High spatial resolution observations of H_2_ vibrational emission in NGC 7023.* A&A, 308:895–907 (1996)

Lemke, D., **Klaas, U.**, **Abolins, J.**, *et al. ISOPHOT - capabilities and performance.* A&A, 315:L64–L70 (1996)

Li, A. *Interaction of Nanoparticles with Radiation.* In **A. N. Witt, G. C. Clayton, & B. T. Draine**, editor, *Astrophysics of Dust*, volume 309 of *Astronomical Society of the Pacific Conference Series*, pages 417–+ (2004)

Li, A. and **Draine, B. T.** *Infrared Emission from Interstellar Dust. II. The Diffuse Interstellar Medium.* ApJ, 554:778–802 (2001a)

Li, A. and **Draine, B. T.** *On Ultrasmall Silicate Grains in the Diffuse Interstellar Medium.* ApJ, 550:L213–L217 (2001b)

Li, A. and **Draine, B. T.** *Do the Infrared Emission Features Need Ultraviolet Excitation? The Polycyclic Aromatic Hydrocarbon Model in UV-poor Reflection Nebulae.* ApJ, 572:232–237 (2002)

Lovas, F. J., **McMahon, J.**, **Grabow, J. U.**, *et al. Insterstellar chemistry: a strategy for detecting polycyclic aromatic hydrocarbons in space*. J. Am. Chem. Soc., 127:4345–4349 (2005)

Malloci, G., **Joblin, C.**, and **Mulas, G.** *On-line database of the spectral properties of polycyclic aromatic hydrocarbons*. Chemical Physics, 332:353–359 (2007)

Malloci, G., **Mulas, G.**, and **Joblin, C.** *Electronic absorption spectra of PAHs up to vacuum UV. Towards a detailed model of interstellar PAH photophysics*. A&A, 426:105–117 (2004)

Markwardt, C. B. *Non-linear Least-squares Fitting in IDL with MPFIT*. In **D. A. Bohlender, D. Durand, & P. Dowler**, editor, *Astronomical Society of the Pacific Conference Series*, volume 411 of *Astronomical Society of the Pacific Conference Series*, pages 251–+ (2009)

Martini, P., **Sellgren, K.**, and **Hora, J. L.** *Near-Infrared Spectroscopy of Molecular Filaments in the Reflection Nebula NGC 7023*. ApJ, 484:296–+ (1997)

Mathis, J. S., **Rumpl, W.**, and **Nordsieck, K. H.** *The size distribution of interstellar grains*. ApJ, 217:425–433 (1977)

McKee, C. F. and **Ostriker, J. P.** *A theory of the interstellar medium - Three components regulated by supernova explosions in an inhomogeneous substrate*. ApJ, 218:148–169 (1977)

Mennella, V., **Colangeli, L.**, and **Bussoletti, E.** *The absorption coefficient of cosmic carbon analogue grains in the wavelength range 20 - 2000 microns*. A&A, 295:165–170 (1995)

Merrill, P. W. *Unidentified Interstellar Lines*. PASP, 46:206–207 (1934)

Montillaud, J., **Joblin, C.**, and **Toublanc, D.** *Modelling the physical and chemical evolution of PAHs and PAH-related species in astrophysical environments*. in PAHs and the Universe, C. Joblin and A.G.G.M Tielens Eds (2011)

Mulas, G. *A MonteCarlo model of the rotation of a big, isolated molecule in the ISM*. A&A, 338:243–261 (1998)

Mulas, G., **Malloci, G.**, **Joblin, C.**, *et al. Estimated IR and phosphorescence emission fluxes for specific polycyclic aromatic hydrocarbons in the Red Rectangle*. A&A, 446:537–549 (2006)

Murakami, H., **Baba, H.**, **Barthel, P.**, *et al. The Infrared Astronomical Mission AKARI*. PASJ, 59:369–+ (2007)

Neugebauer, G., **Habing, H. J.**, **van Duinen, R.**, *et al. The Infrared Astronomical Satellite (IRAS) mission*. ApJ, 278:L1–L6 (1984)

Nummelin, A., **Whittet, D. C. B.**, **Gibb, E. L.**, *et al. Solid Carbon Dioxide in Regions of Low-Mass Star Formation*. ApJ, 558:185–193 (2001)

Onaka, T., **Matsuhara, H.**, **Wada, T.**, *et al. The Infrared Camera (IRC) for AKARI – Design and Imaging Performance*. PASJ, 59:401–+ (2007)

Ott, S. . In **Y Mizumoto, K. I. Morita, M. Ohishi**, editor, *ASP Conference Series, Astronomical Data Analysis Software and Systems XIX*, page "in press" (2010)

Peeters, E., **Allamandola, L. J.**, **Hudgins, D. M.**, *et al. The Unidentified InfraRed Features after ISO*. In **A. N. Witt, G. C. Clayton, & B. T. Draine**, editor, *Astrophysics of Dust*, volume 309 of *Astronomical Society of the Pacific Conference Series*, pages 141–+ (2004)

Peeters, E., **Hony, S.**, **Van Kerckhoven, C.**, *et al. The rich 6 to 9 vec mu m spectrum of interstellar PAHs*. A&A, 390:1089–1113 (2002)

Pendleton, Y. J. and **Allamandola, L. J.** *The Organic Refractory Material in the Diffuse Interstellar Medium: Mid-Infrared Spectroscopic Constraints*. ApJS, 138:75–98 (2002)

Pety, J. *Successes of and Challenges to GILDAS, a State-of-the-Art Radioastronomy Toolkit*. In **F. Casoli, T. Contini, J. M. Hameury, & L. Pagani**, editor, *SF2A-2005: Semaine de l'Astrophysique Francaise*, pages 721–+ (2005)

Pety, J., **Teyssier, D.**, **Fossé, D.**, *et al. Are PAHs precursors of small hydrocarbons in photo-dissociation regions? The Horsehead case*. A&A, 435:885–899 (2005)

Pilbratt, G. L., **Riedinger, J. R.**, **Passvogel, T.**, *et al. Herschel Space Observatory. An ESA facility for far-infrared and submillimetre astronomy*. A&A, 518:L1+ (2010)

Pilleri, P., **Herberth, D.**, **Giesen, T. F.**, *et al. Search for corannulene ($C_{20}H_{10}$) in the Red Rectangle*. MNRAS, 397:1053–1060 (2009)

Poglitsch, A., **Waelkens, C.**, **Geis, N.**, *et al. The Photodetector Array Camera and Spectrometer (PACS) on the Herschel Space Observatory*. A&A, 518:L2+ (2010)

Racine, R. *Stars in reflection nebulae*. AJ, 73:233–+ (1968)

Rapacioli, M., **Calvo, F.**, **Joblin, C.**, *et al. Formation and destruction of polycyclic aromatic hydrocarbon clusters in the interstellar medium*. A&A, 460:519–531 (2006)

Rapacioli, M., **Joblin, C.**, and **Boissel, P.** *Spectroscopy of polycyclic aromatic hydrocarbons and very small grains in photodissociation regions*. A&A, 429:193–204 (2005)

Rieke, G. H., **Young, E. T.**, **Engelbracht, C. W.**, *et al. The Multiband Imaging Photometer for Spitzer (MIPS)*. ApJS, 154:25–29 (2004)

Rouan, D., **Léger, A.**, **Omont, A.**, *et al. Physics of the rotation of a PAH molecule in interstellar environments*. A&A, 253:498–514 (1992)

Ryder, S. D., **Allen, L. E.**, **Burton, M. G.**, *et al. Molecular hydrogen line emission from the reflection nebula Parsamyan 18*. MNRAS, 294:338–+ (1998)

Salama, A. *ISO: highlights of recent results*. Advances in Space Research, 34:528–534 (2004)

Salama, F., **Bakes, E. L. O.**, **Allamandola, L. J.**, *et al. Assessment of the polycyclic aromatic Hydrocarbon–Diffuse interstellar band proposal*. ApJ, 458:621–636 (1996)

Salama, F., **Galazutdinov, G. A.**, **Krełowski, J.**, *et al. Polycyclic Aromatic Hydrocarbons and the Diffuse Interstellar Bands: A Survey*. ApJ, 526:265–273 (1999)

Scott, A. and **Duley, W. W.** *The Decomposition of Hydrogenated Amorphous Carbon: A Connection with Polycyclic Aromatic Hydrocarbon Molecules*. ApJ, 472:L123+ (1996)

Sellgren, K., **Uchida, K. I.**, and **Werner, M. W.** *The 15-20 μm Spitzer Spectra of Interstellar Emission Features in NGC 7023*. ApJ, 659:1338–1351 (2007)

Sellgren, K., **Werner, M. W.**, **Ingalls, J. G.**, *et al. C$ _{60}$ in Reflection Nebulae*. ArXiv e-prints (2010)

Shimonishi, T., **Onaka, T.**, **Kato, D.**, *et al. AKARI Near-Infrared Spectroscopy: Detection of H_2O and CO_2 Ices toward Young Stellar Objects in the Large Magellanic Cloud*. ApJ, 686:L99–L102 (2008)

Simon, A. and **Joblin, C.** *Photodissociation of $[Fe_x(C_{24}H_{12})_y]^+$ complexes in the PIRENEA set-up : iron-PAH clusters as good candidates for interstellar very small grains*. J. Phys. Chem. A, 113:4878–4888 (2009)

Sloan, G. C., **Bregman, J. D.**, **Geballe, T. R.**, *et al. Variations in the 3 Micron Spectrum across the Orion Bar: Polycyclic Aromatic Hydrocarbons and Related Molecules*. ApJ, 474:735–+ (1997)

Sloan, G. C., **Hayward, T. L.**, **Allamandola, L. J.**, *et al. Direct Spectroscopic Evidence for Ionized Polycyclic Aromatic Hydrocarbons in the Interstellar Medium*. ApJ, 513:L65–L68 (1999)

Sloan, G. C., **Jura, M.**, **Duley, W. W.**, *et al. The Unusual Hydrocarbon Emission from the Early Carbon Star HD 100764: The Connection between Aromatics and Aliphatics*. ApJ, 664:1144–1153 (2007)

Smith, J. D. T., **Draine, B. T.**, **Dale, D. A.**, *et al. The Mid-Infrared Spectrum of Star-forming Galaxies: Global Properties of Polycyclic Aromatic Hydrocarbon Emission*. ApJ, 656:770–791 (2007)

Smolders, K., **Acke, B.**, **Verhoelst, T.**, *et al. When an old star smolders . On the detection of hydrocarbon emission from S-type AGB stars*. A&A, 514:L1+ (2010)

Stecher, T. P. *Interstellar Extinction in the Ultraviolet. II*. ApJ, 157:L125+ (1969)

Szczepanski, J. and **Vala, M.** *Infrared frequencies and intensities for astrophysically important polycyclic aromatic hydrocarbon cations*. ApJ, 414:646–655 (1993a)

Szczepanski, J. and **Vala, M.** *Laboratory evidence for ionized polycyclic aromatic hydrocarbons in the interstellar medium*. Nature, 363:699–701 (1993b)

Tauber, J. A., **Tielens, A. G. G. M.**, **Meixner, M.**, *et al. Anatomy of a Photodissociation Region: High angular resolution images of molecular emission in the Orion Bar*. ApJ, 422:136–152 (1994)

Teyssier, D., **Fossé, D.**, **Gerin, M.**, *et al. Carbon budget and carbon chemistry in Photon Dominated Regions*. A&A, 417:135–149 (2004)

Thaddeus, P. *The prebiotic molecules observed in the interstellar gas*. Phil. Trans. R. Soc., 361:1681–1687 (2006)

Thorwirth, S., **Theulé, P.**, **Gottlieb, C. A.**, *et al. Rotational Spectra of Small PAHs: Acenaphthene, Acenaphthylene, Azulene, and Fluorene*. ApJ, 662:1309–1314 (2007)

Tielens, A. G. G. M. *The Physics and Chemistry of the Interstellar Medium*. The Physics and Chemistry of the Interstellar Medium, by A. G. G. M. Tielens, pp. . ISBN 0521826349. Cambridge, UK: Cambridge University Press, 2005. (2005)

Useli Bacchitta, F. *Photophysique des molćules polycycliques aromatiques hydrogńés dÕintŕêt interstellaire avec lÕexpŕience PIRENEA*. Ph.D. thesis, Centre d'Etude Spatial des Rayonnement, Université Paul Sabatier, Toulouse, France (2009)

Useli-Bacchitta, F., **Bonnamy, A.**, **Mulas, G.**, *et al. Visible photodissociation spectroscopy of PAH cations and derivatives in the PIRENEA experiment*. Chemical Physics, 371:16–23 (2010)

Useli Bacchitta, F. and **Joblin, C.** *Photo-dissociation of large hydrocarbons with PIRENEA*. In *Molecules in Space and Laboratory* (2007)

van den Ancker, M. E., **The, P. S.**, **Tjin A Djie, H. R. E.**, *et al. HIPPARCOS data on Herbig Ae/Be stars: an evolutionary scenario.* A&A, 324:L33–L36 (1997)

van der Tak, F. F. S., **Black, J. H.**, **Schöier, F. L.**, *et al. A computer program for fast non-LTE analysis of interstellar line spectra. With diagnostic plots to interpret observed line intensity ratios*. A&A, 468:627–635 (2007)

Vastel, C., **Spaans, M.**, **Ceccarelli, C.**, *et al. The physical conditions in the PDR of W49N*. A&A, 376:1064–1072 (2001)

Waters, L. B. F. M., **Waelkens, C.**, **van Winckel, H.**, *et al. An oxygen-rich dust disk surrounding an evolved star in the Red Rectangle*. Nature, 391:868–871 (1998)

Weingartner, J. C. and **Draine, B. T.** *Dust Grain-Size Distributions and Extinction in the Milky Way, Large Magellanic Cloud, and Small Magellanic Cloud*. ApJ, 548:296–309 (2001)

Werner, M. W., **Roellig, T. L.**, **Low, F. J.**, *et al. The Spitzer Space Telescope Mission*. ApJS, 154:1–9 (2004a)

Werner, M. W., **Uchida, K. I.**, **Sellgren, K.**, *et al. New Infrared Emission Features and Spectral Variations in NGC 7023*. ApJS, 154:309–314 (2004b)

Witt, A. N., **Gordon, K. D.**, **Vijh, U. P.**, *et al. The Excitation of Extended Red Emission: New Constraints on Its Carrier from Hubble Space Telescope Observations of NGC 7023*. ApJ, 636:303–315 (2006)

Young Owl, R. C., **Meixner, M. M.**, **Fong, D.**, *et al. Testing Models of Low-Excitation Photodissociation Regions with Far-Infrared Observations of Reflection Nebulae*. ApJ, 578:885–896 (2002)

Abstract

Polycyclic Aromatic Hydrocarbons (PAHs) are a major constituent of interstellar matter, containing about 20% of the total carbon in our Galaxy. PAHs are known to play a major role in the chemistry and the physics of photo-dissociation regions (PDRs). In these environments, the evolution of PAHs is driven by the UV field and it has been proposed to be linked to that of very small dust particles and small molecular hydrocarbons. In this work, we provide further insights into these evolutionary scenarios by combining the analysis of infrared (IR) data from ISO, *Spitzer* and AKARI space telescopes with new observations in the far-IR and sub-mm domains obtained with *Herschel* as well as in the millimeter domain using the IRAM ground-based telescopes.

We have developed a new analysis method for the mid-IR spectro-imagery observations that allows to study the photo-processing of evaporating Very Small Grains (eVSGs) in PDRs. This procedure provides an estimate of the fraction of carbon locked in eVSGs compared to all atoms in the AIB carriers. This quantity is found to be related to the UV radiation field and can therefore be used as a tracer of its intensity in both resolved and unresolved sources. The obtained results are also consistent with a scenario in which eVSGs are destroyed by the UV field, giving birth to free PAHs. The results of the mid-IR analysis are compared with near-IR and millimeter observations, showing that the destruction process of eVSGs may be a source of production of small hydrocarbons. An accurate modelling of hydrocarbon chemistry in PDRs is needed to quantitatively test this scenario.

We used the IRAM 30 m telescope to search for the specific rotational signatures of an individual PAH, corannulene, in the millimeter spectrum of the Red Rectangle nebula. The comparison of the derived upper limit for detection with models allows to constrain the maximum abundance of small PAHs in this source. This provides evidence that these small species are under-abundant in the envelopes of evolved carbon stars and constrains the formation mechanisms of PAHs in these environments.

The results of the mid-IR analysis are combined with observations of several gas species in the far-IR and sub-millimeter with *Herschel* and in the millimeter with IRAM to study the geometry, energetics, and dynamics of the PDRs in the reflection nebula NGC 7023. Further progresses on this topics await for more *Herschel* data but also for the forthcoming JWST and SPICA space missions and the ALMA interferometer.

Resumé

Les molécules Polycycliques Aromatiques Hydrogénées (PAH) sont un constituant majeur de la matière interstellaire, contenant environ 20% de la totalité du carbone dans notre galaxie. Les PAH jouent un rôle majeur dans la physique et la chimie des régions de photo-dissociation (PDR). Dans ces environnements, l'évolution des PAH est pilotée par le champ de rayonnement ultraviolet (UV) et il a été proposé qu'elle soit liée à celle des très petites particules de poussière et aux petits hydrocarbures. Dans ce travail, nous proposons un nouvel éclairage sur ces scénarios d'évolution en combinant les analyses des données infrarouges (IR) des télescopes spatiaux ISO, *Spitzer* et AKARI, à de nouvelles observations dans les domaines de l'IR lointain et du sub-millimétrique obtenues par le satellite *Herschel* ainsi que dans le domaine millimétrique grâce aux télescopes au sol de l'IRAM.

Nous avons développé une nouvelle méthode d'analyse des observations de spectro-imagerie de l'IR moyen qui permet d'étudier l'évolution des très petits grains en cours d'évaporation (eVSG) dans les PDR. Cette procédure fournit une estimation de la fraction de carbone contenu dans les eVSG par rapport au total du carbone contenu dans les espèces responsables de l'émission des Bandes Infrarouges Aromatiques (AIB). Cette quantité s'avère être reliée au champ de rayonnement UV et peut ainsi être utilisée comme sonde de l'intensité de ce rayonnement dans des sources résolues ou non spatialement. Les résultats obtenus sont également cohérents avec un scénario dans lequel la destruction des eVSG par le champ UV donne naissance à des PAH libres. Les résultats de l'analyse dans l'IR moyen sont comparés aux observations des domaines du proche IR et du millimétrique, montrant que les processus de destruction des eVSG pourraient être une source de petits hydrocarbures. Une modélisation précise de la chimie des hydrocarbures dans les PDR s'avère nécessaire pour quantifier ce scénario.

Nous avons utilisé le télescope de 30 m de l'IRAM pour chercher la signature rotationnelle spécifique d'un PAH individuel, le corannulène, dans le spectre millimétrique de la nébuleuse du Rectangle Rouge. En comparant à des modèles la limite supérieure d'abondance déduite de la non détection de ce PAH, nous avons pu contraindre l'abondance maximale des PAH de petite taille dans cette source. Ceci indique que ces espèces sont sous-abondantes dans les enveloppes des étoiles carbonées évoluées, et contraint les mécanismes de formation des PAH dans ces environnements.

Les résultats de l'analyse dans l'infrarouge moyen sont combinés aux observations de plusieurs constituants du gaz dans l'IR lointain et le submillimétrique grâce au satellite *Herschel* et dans le millimétrique avec les instruments de l'IRAM afin d'étudier la géométrie, le bilan énergétique et la dynamique des PDR associées à la nébuleuse par réflexion NGC 7023. Ce sujet devrait continuer à progresser dans les années à venir

grâce à de nouvelles données *Herschel*, mais aussi l'arrivée de futures missions spatiales JWST et SPICA et de l'interféromètre ALMA.